

LIFE PASTORALP



LIFE16 CCA/IT/000060

Pastures vulnerability and adaptation strategies to climate change impacts in the Alps

Deliverable C.4

Models calibrated and validated

June, 2020

Updated May, 2021



Acknowledgements

This report was produced under co-finance of the EC LIFE programme for the Environment and Climate Action (2014-2020), in the framework of Action C.4 “Modelling framework” of the project LIFE PASTORALP (LIFE16 CCA/IT/000060) “Pastures vulnerability and adaptation strategies to climate change impacts in the Alps”.

The project is being implemented by the following beneficiaries:

	University of Florence - UNIFI
	Agenzia Regionale Protezione Ambiente - Valle d'Aosta - ARPA VDA
	Centre National de la Recherche Scientifique - CNRS
	Institut Agricole Régional – IAR
	Institut National de Recherche pour l'Agriculture l'alimentation et l'Environnement – INRAE
	Parc National des Ecrins – PNE
	Ente Parco Nazionale Gran Paradiso – PNGP

ACTION C.4: Modelling framework
Deliverable: Models calibrated and validated

Author(s)	Organisation(s)	E-mail(s)
Gianni Bellocchi Dehia Hadj Saadi Raphaël Martin	French National Research Institute for Agriculture, Food and Environment, Grassland Ecosystem Research Unit - INRAE-UREP (Clermont-Ferrand, France)	gianni.bellocchi@inrae.fr dehia.hadj-saadi@inrae.fr raphael.martin@inrae.fr
Giovanni Argenti Lorenzo Brilli Sergi Costafreda Aumedes Camilla Dibari	University of Florence - UNIFI (Italy)	giovanni.argenti@unifi.it lorenzo.brilli@unifi.it sergi.costafredaumedes@unifi.it camilla.dibari@unifi.it
Gianluca Filippa	Agenzia Regionale Protezione Ambiente - Valle d'Aosta - ARPA VDA (Italy)	gian.filippa@gmail.com

Contents

Executive Summary	10
1 How to read the document	10
2 List of acronyms.....	11
3 Introduction.....	12
4 Site-specific calibration of DayCent and PaSim.....	12
4.1 DayCent calibration results	14
4.2 PaSim calibration results	16
5 Sensitivity analysis of PaSim.....	18
5.1 Impact of snow cover on above ground biomass	18
5.1.1 Light-interception modification by snow cover	19
5.1.2 Water-supply modification by snow melt	19
5.2 Impact of soil texture variations on AGB and LAI.....	20
5.2.1 Growth start date	23
5.2.2 Growth end date	25
5.2.3 Date of maximum growth	27
5.2.4 Mean AGB.....	29
5.2.5 Maximum AGB.....	31
5.2.6 Mean LAI.....	33
5.2.7 Maximum LAI.....	35
5.3 Impact of pH variations on AGB and LAI	37
5.3.1 Growth start date	38
5.3.2 Growth end date	38
5.3.3 Date of maximum growth	39
5.3.4 Mean AGB.....	40
5.3.5 Maximum AGB.....	40
5.3.6 Mean LAI.....	41
5.3.7 Maximum LAI.....	42
5.4 Impact of SOC variations on AGB and LAI	42
5.4.1 Growth start date	42
5.4.2 Growth end date	43
5.4.3 Date of maximum growth	44
5.4.4 Mean AGB.....	44
5.4.5 Maximum AGB.....	45
5.4.6 Mean LAI.....	45
5.4.7 Maximum LAI.....	46
5.5 Climate analysis	47
6 Random Forest set up and assessment.....	51
6.1 Methodology	51

6.1.1	The Random Forest (RF) machine-learning statistical model	51
6.1.2	Ancillary data for RF training	51
6.1.3	RF calibration and validation	52
6.2	Results	52
6.2.1	RF calibration outputs and accuracy	52
6.2.2	Future pasture distribution	54
7	Simulations under future scenarios (DayCent, PNGP) – based on site-specific calibration.....	59
8	Extraction of satellite-derived vegetation spectral indices.....	62
9	Simulations under future scenarios – based on macro-type calibration	65
10	Concluding statements.....	70
11	References.....	70
	Appendix A - Sites description.....	73
1.	Torgnon	73
2.	Entrelor.....	74
3.	Oisans	75
	Appendix B - Site-specific parameterisation data (PaSim).....	78
1.	Torgnon	78
2.	Entrelor.....	78
3.	Oisans	79
	Appendix C - List of PaSim vegetation parameters	83
	Appendix D - NDVI data analysis	85
	Site description.....	85
	What is NDVI?.....	85
	NDVI data	85
	Calibration data	86
	NDVI data processing	88

List of figures

Fig. 4.1. Geographic location of the study areas and sites.

Fig. 4.2. Description of the study sites (appendix A provides detailed information for each site).

Fig. 4.3. Comparisons between DayCent simulations (red dotted line) and observations (black continuous line) of gross primary production (GPP, $g\ C\ m^{-2}\ month^{-1}$) at Torgnon.

Fig. 4.4. Comparisons between DayCent simulations (red dotted line) and observations (black continuous line) of soil water content (% , 0.3 m) at Torgnon.

Fig. 4.5. Comparison between DayCent simulations (red dotted line) and observations (black continuous line) of above ground biomass ($kg\ DM\ ha^{-1}$) at Entrelor (Alto).

Fig. 4.6. Comparison between DayCent simulations (coloured dotted line) and observations (coloured rectangles) of net primary production ($g\ C\ m^{-2}$) at Oisans (year 2007).

Fig. 4.7. Comparisons between PaSim simulations (blue dots) and observations (brown dots) of aboveground biomass at Torgnon.

Fig. 4.8. Comparisons between PaSim simulations (blue dots) and observations (brown dots) of aboveground biomass at Entrelor (two sites).

Fig. 4.9. Comparisons between PaSim simulations (blue dots) and observations (brown dots) of aboveground biomass at Oisans (five sites).

Fig. 5.1. Comparison of simulated aboveground biomass obtained considering or not the snow cover effect.

Fig. 5.2. Comparison of aboveground biomass simulated in the presence and absence of water accumulation, and with light-interception effects.

Fig. 5.3. First soil layer texture at Torgnon (a red dot for each of 10000 simulations).

Fig. 5.4. Texture distribution for layers 4, 5 and 6.

Fig. 5.5. Texture distribution for the 0-30 cm layer.

Fig. 5.6. Mean start date of growing season.

Fig. 5.7. Coefficient of variation of growth start date.

Fig. 5.8. Mean end date of growing season.

Fig. 5.9. Coefficient of variation of growth end date.

Fig. 5.10. Mean date of maximum growth.

Fig. 5.11. Coefficient of variation of the date of maximum growth.

Fig. 5.12. Mean AGB ($kg\ DM\ m^{-2}$).

Fig. 5.13. Coefficient of variation of mean AGB.

Fig. 5.14. Maximum AGB (kg DM m⁻²).

Fig. 5.15. Coefficient of variation of maximum AGB.

Fig. 5.16. Mean LAI (m² m⁻²).

Fig. 5.17. Coefficient of variation of mean LAI.

Fig. 5.18. Maximum LAI (m² m⁻²).

Fig. 5.19. Coefficient of variation of maximum LAI.

Fig. 5.20. Variation of growth start date with pH and by year.

Fig. 5.21. Variation of growth end date with pH and by year.

Fig. 5.22. Variation of the date of maximum growth with pH and by year.

Fig. 5.23. Variation of mean AGB (kg DM m⁻²) with pH and by year.

Fig. 5.24. Variation of maximum AGB (kg DM m⁻²) with pH and by year.

Fig. 5.25. Variation of mean LAI (m² m⁻²) with pH and by year.

Fig. 5.26. Variation of maximum LAI (m² m⁻²) with pH and by year.

Fig. 5.27. Variation of growth start date with SOC and by year.

Fig. 5.28. Variation of growth end date with SOC and by year.

Fig. 5.29. Variation of the date of maximum growth with SOC and by year.

Fig. 5.30. Variation of mean AGB (kg DM m⁻²) with SOC and by year.

Fig. 5.31. Variation of maximum AGB (kg DM m⁻²) with SOC and by year.

Fig. 5.32. Variation of mean LAI (m² m⁻²) with SOC and by year.

Fig. 5.33. Variation of maximum LAI (m² m⁻²) with SOC and by year.

Fig. 5.34. Time series of (A) air temperature (°C) and (B) rainfall (mm d⁻¹) at Torgnon.

Fig. 5.35. Soil water content (%) observed at Torgnon.

Fig. 5.36. De Martonne-Gottmann aridity index.

Fig. 5.37. UNEP aridity index.

Fig. 5.38. Simulated aboveground biomass (kg DM m⁻²).

Fig. 6.1 displays the partial plots of predictors, i.e. the graphical depiction of the marginal effect of predictors on the RF class classification for both PNGP and PNE areas.

Fig. 6.2. Relative importance of climatic variables, expressed as mean decrease accuracy, in the classification process as derived from random forest calibration. Variables are pH; slope; Tmax_jul: monthly average maximum temperature of July; Tmin_jan: monthly average minimum temperature of January; Prec_djf, Prec_mam, Prec_jja, and Prec_son cumulated precipitation of winter, spring, summer and autumn season, respectively.

Fig. 6.3. Partial Dependence Plot of the probability of presence of pastures across PNGP and PNE versus increasing values of Slope, pH, Tmin_Jan, Tmax_Jul, Prec_djf, Prec_mam, Prec_jja, Prec_son. The original data were interpolated using a polynomial function.

Fig. 6.4. Grid cell map representing the distribution of pastures across PNGP in the present (top of the figure) and variations (in red losses, in green gains and in grey no change) in the near (2011-2040) and far future (2041-2070) under RCP 4.5 and 8.5 RCP scenarios according to the three RCMs with respect to the present, as simulated by RF.

Fig. 6.5. Grid cell map representing the distribution of pastures across PNE study area in the present (top of the figure) and variations (in red losses, in green gains and in grey no change) in the near (2011-2040) and far future (2041-2070) under RCP 4.5 and 8.5 RCP scenarios according to the three RCMs with respect to the present, as simulated by RF.

Fig. 7.1. Projected snow-cover height trend under near (2011-2040) and far (2041-2070) future, as predicted by the ensemble of RCMs (CNRM-ALADIN, ICTP-RGCM4, and CMCC-CCLM4) for RCP 4.5 and 8.5 scenarios at (a) Torgnon, (b) Entrelor (Alto) and (c) Oisans (average of sites 2, 3, 4 and 5).

Fig. 7.2. Projected duration of vegetation period under near (2011-2040) and far (2041-2070) future, as predicted by the ensemble of RCMs (CNRM-ALADIN, ICTP-RGCM4, and CMCC-CCLM4) for RCP 4.5 and 8.5 scenarios at (a) Torgnon, (b) Entrelor (Alto) and (c) Oisans (average of sites 2, 3, 4 and 5).

Fig. 7.3. Projected net primary production pattern ($g C m^{-2} d^{-1}$) under near (2011-2040) and far (2041-2070) future, as predicted by the ensemble of RCMs (CNRM-ALADIN, ICTP-RGCM4, and CMCC-CCLM4) for RCP 4.5 and 8.5 scenarios at Torgnon (top graph) and Entrelor Alto (bottom graph).

Fig. 8.1. Three-year seasonal trajectories of S2-derived NDVI values in selected PNGP pastures.

Fig. 8.2. Three-year seasonal trajectories of S2-derived LAI values in selected PNGP pastures.

Fig. 8.2. Three-year seasonal trajectories of LAI, as calculated from Eq. (1).

Fig. 9.1. Comparisons of DayCent simulations of aboveground biomass (AGB, $g DM m^{-2}$, red line) and snow cover (cm, H_2O , blue lines) with observations (black lines and grey areas, respectively) at PNE and PNGP for three macro-types (HP, MP, LP).

Fig. 9.2. Projected mean duration of the vegetation period for the baseline, near (2011-2040) and far (2041-2070) future, as predicted by DayCent with the ensemble of RCMs (CNRM-ALADIN, ICTP-RGCM4, and CMCC-CCLM4) for RCP 4.5 and 8.5 scenarios for the three macro-types (HP, MP, LP) of PNE and PNGP.

Fig. 9.3. Projected aboveground biomass mean pattern ($g C m^{-2}$) for the baseline, near (2011-2040) and far (2041-2070) future, as predicted by DayCent with the ensemble of RCMs (CNRM-ALADIN, ICTP-RGCM4, and CMCC-CCLM4) for RCP 4.5 and 8.5 for the three macro-types (HP, MP, LP) of PNE and PNGP.

Fig. 9.4. Exceedance probability (%) distribution functions of PaSim-simulated annual values of present and future above ground biomass (kg DM m^{-2}) in the PNE, as predicted by the ensemble of RCMs (CNRM-ALADIN, ICTP-RGCM4, and CMCC-CCLM4) for RCP 4.5 and 8.5. The red arrows indicate the trend towards higher values with future scenarios.

Fig. 9.5. Exceedance probability (%) distribution functions of present and future annual dates (days of year) of PaSim-simulated aboveground biomass peak in the PNE, as predicted by the ensemble of RCMs (CNRM-ALADIN, ICTP-RGCM4, and CMCC-CCLM4) for RCP 4.5 and 8.5. The red arrows indicate the trend towards earlier biomass peaks with future scenarios. Dates exceeding 0.5 probability are reported.

Fig. 9.6. Projected soil water content mean pattern ($\text{m}^3 \text{m}^{-3}$) for the baseline, near (2011-2040) and far (2041-2070) future, as predicted by DayCent with the ensemble of RCMs (CNRM-ALADIN, ICTP-RGCM4, and CMCC-CCLM4) for RCP 4.5 and 8.5 for the three macro-types (HP, MP, LP) of PNE and PNGP.

Fig. 9.7. Projected net ecosystem exchange (NEE) mean pattern (g C m^{-2}) for the baseline, near (2011-2040) and far (2041-2070) future, as predicted by DayCent with the ensemble of RCMs (CNRM-ALADIN, ICTP-RGCM4, and CMCC-CCLM4) for RCP 4.5 and 8.5 for the three macro-types (HP, MP, LP) of PNE and PNGP.

Fig. D.1. NDVI sensor.

Fig. D.2. Interannual dynamics of NDVI (FLUXALP Lautaret-Charmase station, PNE, France).

Fig. D.3. Relation between leaf area index (LAI) and above ground biomass (AGB).

Fig. D.4. Relation between NDVI and leaf area index (LAI).

Fig. D.5. Relation between NDVI and AGB (g m^{-2}).

Fig. D.6. Interannual dynamics of AGB (g m^{-2}).

Executive Summary

This report has been elaborated in the framework of Action C.4 (*Modelling framework*), which focuses on the assessment of process-based (DayCent, PaSim) and statistical (Random Forest) modelling approaches as a preparatory work for an analysis of the vulnerability of pastures in the Western Alpine range. This deliverable integrates the methodologies and results deriving from data collation and harmonization (summarised in deliverable C.1 *Data collection and harmonization and downscaling of climate scenarios*) and describes the modelling actions performed with DayCent, PaSim and Random Forest. Specifically, meteorological observations and data on pasture management, production, growth and development, which were collected from stations located in the two study areas (Parc National des Ecrins and Parco Nazionale Gran Paradiso), have been the basis for the model calibration work. Complementary analyses have been performed (mostly with the grassland-specific model PaSim) to assess the sensitivity of grassland outputs to the variability of snowpack cover and soil factors (texture, pH and soil organic carbon content) and prepare the selection of pasture macro-type classes in both PNGP and PNE. It is at this level that satellite-derived leaf area index (LAI) and normalised difference vegetation index (NDVI) trajectories (deliverable C2 *Pastures typologies survey and mapping*) were extracted for the final calibration work. Machine learning (Random Forest) was employed to map the environmental suitability of representative pasture macro-type classes in French and Italian Alps, and simulate the impact of climate change on their dynamics. The modelling framework includes the economic model, which is not included in this deliverable. Since it requires a continuous review by stakeholders, additional consultations are needed. Hence, it will be documented in deliverable C.5, as a part of the vulnerability assessment.

1 How to read the document

The document consists of four main sections (plus introduction and references). Each section contains a complete description of a set of operations or processes or links to additional internal documents where the topic is developed in more detail.

The sections are organized as follows:

“Introduction” (Section 3), in which the topic is introduced with ground on the relevant body of literature

“Site-specific calibration of DayCent and PaSim” (Section 4), in which the results obtained with the two models at grassland sites in PNGP and PNE are presented

“Sensitivity analysis of PaSim” (Section 5), in which the methodology used and the results achieved with PaSim are described and displayed

“Random Forest set up and assessment” (Section 6), in which the machine learning approach used to map grassland macro-types and predict their evolution under future changes of the Alpine climate is presented

“Simulations under future scenarios (DayCent, PNGP) – based on site-specific calibration” (Section 7), in which some preliminary results are anticipated on the possible impacts of climate change in the PNGP

“Extraction of satellite-derived vegetation spectral indices” (Section 8), in which the methodology used to derive satellite data for model calibration is described

“Simulations under future scenarios – based on macro-type calibration” (Section 9) extends the achievements of Section 4 and Section 7 to pastoral macro-types based on the methodology of Section 8

“Concluding statements” (Section 10) summarises the conclusions and the implications of these findings

References (Section 11), in which the supporting literature is reported

2 List of acronyms

AGB	Aboveground biomass
CMCC-CCLM4	Euro-Mediterranean Center on Climate Change- Climate Limited-area Modelling Community (version 4)
CNRM-ALADIN	Centre National de Recherches Météorologiques- Aire Limitée Adaptation dynamique Développement InterNational)
DayCent	Daily CENTURY model
ICTP-RGCM4	International Center for Theoretical Physics- Regional and Global Climate Modeling Program (version 4)
LAI	Leaf area index
NDVI	Normalised difference vegetation index
PaSim	Pasture Simulation model
pH	Potential for hydrogen
PNE	Parc National des Ecrins
PNGP	Parco Nazionale Gran Paradiso
RCM	Regional circulation model
RCP	Representative concentration pathway
RF	Random Forest
SOC	Soil organic carbon

3 Introduction

The last decades have seen changes in land use/cover, with a reduction in the land allocated to grasslands, whether in Europe (Peyraud et al., 2012) or in different regions of the world (e.g. Fakarayi et al., 2015; Münch et al., 2017; Schirpke et al., 2017; Gibson et al., 2018). It is recognized that these changes are socio-economically important (Dunford et al., 2015) because the replacement of pastures and the erosion of biodiversity do not only modify the continuity of forage production, which supports animal production. Climate change is also expected to negatively affect natural resources such as pastures, which are recognized sensitive and vulnerable ecosystems, especially in Alpine regions.

Changes in plant diversity actually reflect the evolution of two main factors (e.g. Isselstein et al. 2005; Pontes et al., 2010, 2015): environmental conditions (soil and climate) and management practices (mowing, grazing, fertilization, etc.). In this perspective, the objective is the preservation of mountain pastures for their productivity and biodiversity, and for their capacity to protect the soil from erosion, and to maintain landscapes and open spaces useful for tourist activities. To better understand the evolution of these open spaces and their properties, it is essential to relate all the evolution of environmental and management factors. For that, ecosystem modelling is an ideal tool. In fact, models incorporating a mechanistic view of these processes that occur within a grassland system, and encompassing system interactions (e.g. van Oijen et al., 2018), provide a solid basis for studying these interactions, assessing their impact and testing the role of management (what the analysis of empirical data or a meta-analysis of the literature only partially does). Thanks to simulations carried out with models, it is possible to make long-term forecasts of the impact of environmental changes on the grassland ecosystem as well as on the contribution of these grasslands to carbon storage (e.g. Graux et al., 2012, 2013). Grassland modelling will be used here to support the analysis of what is expected to happen to pastoral resources under future climate scenarios in terms of production, biodiversity, quality of fodder, suitability of grassland areas, etc. To translate the impacts of future climate scenarios on pastoral resources in the study area, we used two simulation models (PaSim, DayCent), which were calibrated and validated for the alpine region. The aim is to apply these models to identify improved strategies for the adaptation of managed grasslands to ensure the continuity of fodder production while also supporting soil carbon storage, improving the spreading of manure, and favouring biodiversity (action C6). PaSim - a grassland-specific model - and DayCent - a generic crop model - are daily time-step biogeochemical models simulating carbon and nitrogen fluxes at the atmosphere-vegetation-soil interface. Thanks to their mechanistic vision of the grassland ecosystem, PaSim and DayCent are able to estimate plant and animal production, greenhouse gas (GHG) emissions and changes in carbon storage, and their evolution under projected future climate. The results obtained, whether or not using projected climate data, coupled with the datasets collected in action C1, are used to develop a statistical model (i.e. Random Forest) to describe the suitability of for pasturelands under future climatic conditions in two protected areas. To reduce uncertainties the uncertainties associated with observations and simulation, an in-depth analysis of the data was carried out to explore the sensitivity of grasslands to environmental factors as a preliminary step towards the identification of grassland macro-types, covering the different situations of the French-Italian alpine range and which can be characterised by satellite-derived vegetation indices. The modelling framework includes the economic model, whose assessment was not accommodated as part of this deliverable. Built on criteria requiring a continuous review by stakeholders, additional consultations are needed, which will be embedded in the vulnerability assessment and documented in deliverable C.5.

4 Site-specific calibration of DayCent and PaSim

Simulation models quantify the impacts on carbon (C) and nitrogen (N) cycling in agricultural systems (including grasslands) caused by changes in management practices. To support farm management adaptations and agricultural policies, it is however important to contrast the responses of alternative models, which can differ greatly in their treatment of key processes and

in their response to management. Here, we applied two biogeochemical models (DayCent and PaSim; Table 4.1) at three grassland sites/areas (Figs. 4.1 and 4.2) representative of grassland situations in the Park National des Écrins (Oisans) and Parco Nazionale Gran Paradiso (Entrelor, Torgnon).

Table 4.1. Description of the two biogeochemical models used.

DayCent	PaSim
It is the daily time-step adaptation of the biogeochemical model CENTURY (Parton et al., 1998). It simulates biomass growth, soil C dynamics, N leaching, gaseous emissions (e.g. N ₂ O, NO, N ₂ , NH ₃ , CH ₄ and CO ₂) and C fluxes (e.g. NPP, NEE) in croplands, grasslands, forests and savannahs, as affected by management practices (such as fertilization, tillage, pruning, cutting and grazing) and specific external disturbances (e.g. fires).	The Pasture Simulation model originally developed by Riedo et al. (1998) is a process-based, grassland-specific ecosystem model that simulates grassland productivity and GHG emissions to the atmosphere. The model consists of sub-models for vegetation, grazing animals, microclimate, soil biology, soil physics and management.

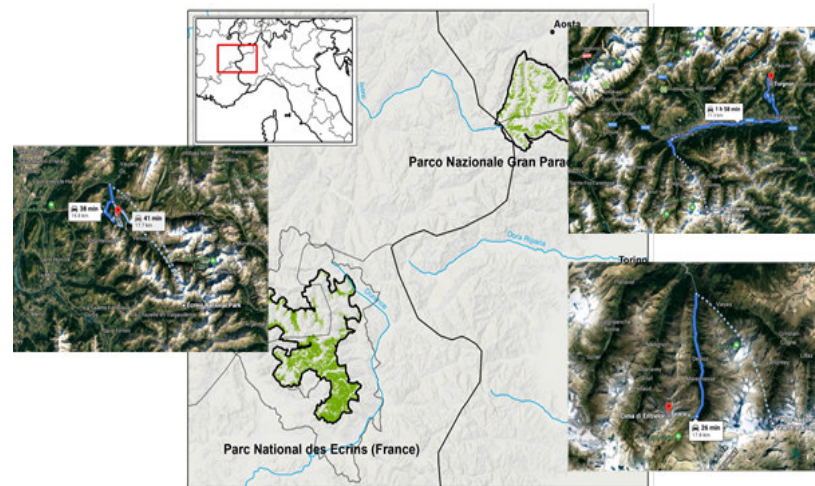


Fig. 4.1. Geographic location of the study areas and sites.

The two test sites of Torgnon and Entrelor (two sites) are located in the Italian western Alps. The former is an unmanaged grassland located at 2200 m a.s.l., the latter is a managed pasture located at 2100 m a.s.l. with different botanical and pedological conditions. On the French side, Oisans includes managed pastures at five sites located over an altitudinal gradient from about 1800 to 2400 m a.s.l.



Fig. 4.2. Geolocation of the study sites (appendix A provides detailed information for each site).

Simulations were set-up at each site with:

1. **Weather data** (max/min air temperatures, precipitation, solar radiation, relative air humidity, wind speed) - daily resolution. For Oisans, they were extracted from the SAFRAN-CROCUS-MEPRA meteorological model developed by Météo-France for the French Alps (Durand et al., 2009). For Torgnon, we referred to sub-hourly time-step weather data as recorded by the local automatic weather station (Galvagno et al., 2013). For Entrelor, a weather dataset was produced in the framework of the hydrological modelling activities operating at the regional level in Valle d'Aosta (Silvestro et al., 2015).
2. **Soil** (depth, texture, chemical properties)
3. **Vegetation** (water-biomass and radiation-biomass conversion coefficients, optimum/maximum temperatures for plant growth)
4. **Management** (grazing, cutting, nitrogen fertilisation)

The simulation design included:

- **Site-specific model calibration** (adaptation of model parameters and comparison of simulated and observed data over multiple years)
- **Impact projections (future climate scenarios)**
 - Time slices: 2011-2040 (near future), 2041-2070 (far future)
 - Emission scenarios (RCP: representative concentration pathways: RCP4.5 (medium radiative forcing) and RCP8.5 (high radiative forcing))

For DayCent calibration, the vegetation eco-physiological characteristics were initially set according to default values found for temperate pastures, as provided by DayCent handbook developed by Colorado State University. Management practices for spin-up and current period were set to reflect as closely as possible the historical and current land use, vegetation type and management. Spin-up runs were performed with DayCent for setting up initial conditions of the main state variables (e.g. carbon and nitrogen pool sizes) at each site (>2000 years of continuous unmanaged pasture).

PaSim was calibrated by minimizing the model-data error by varying 27 parameters. The Latin hypercube sampling method was used to explore the space of possible model solutions. It realizes a quasi-random sampling from a multivariate probability law (https://en.wikipedia.org/wiki/Latin_hypercube_sampling). A pool of 10000 alternative input files was generated in each site, and then PaSim was launched on each of these files and the results explored by searching the one minimizing the error. For instance, for a given variable k , there are $\{obs_{i,k}\}_{i \in \llbracket 1;n \rrbracket}$ n observations and $\{out_{i,j,k}\}_{i \in \llbracket 1;n \rrbracket}$ n outputs from the set of parameters j . We determined the model error by applying the following formula:

$$error_{j,k} = \frac{\sum_{i=1}^n |out_{i,j,k} - obs_{i,k}|}{\sum_{i=1}^n |obs_{i,k}|}$$

Then, in order to calculate the total error:

$$error_j = \sqrt{\sum_k error_{j,k}^2}$$

The best simulation is obtained with the j set of parameters minimizing $error_j$.

4.1 DayCent calibration results

Once implemented, DayCent was calibrated and validated following three steps:

(1) sensitivity analysis to detect the most relevant parameters controlling C and N fluxes and dynamics between soil vegetation and atmosphere. The most sensitive parameters for pastures were identified manually changing value at each run, thus determining the magnitude of changes in the outputs. For each of the main parameters modified, the values were changed in the plausible range as reported by literature.

(2) calibration was performed using the available observed data, specifically, biomass production and soil water content by minimizing the root mean square error (RMSE) between observed and simulated data;

(3) validation was performed using the same available observed data over multiple years. To refine the calibration-validation procedure on a higher number of observed data, further calibrations are undergoing, deriving data from NDVI trajectories extracted from Sentinel2 imageries (Section 8).

Exemplary results show that the model robustly reproduces both the pattern and magnitude of primary production and soil water content at Torgnon (Figs. 4.3 and 4.4) and aboveground biomass at Entrelor (Fig. 4.5).

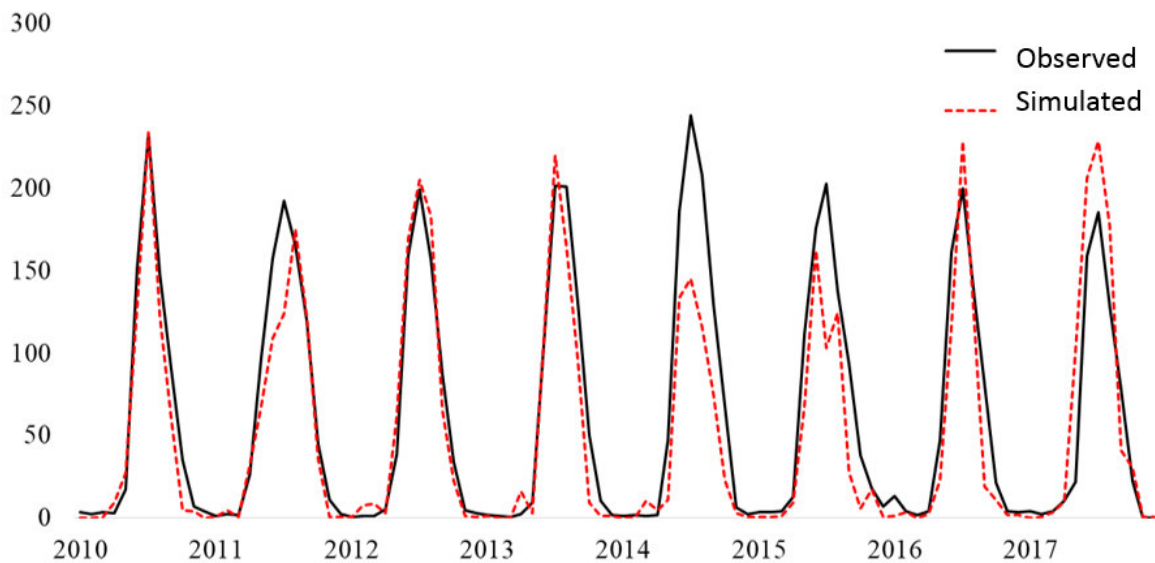


Fig. 4.3. Comparisons between DayCent simulations (red dotted line) and observations (black continuous line) of gross primary production (GPP, $g C m^{-2} month^{-1}$) at Torgnon.

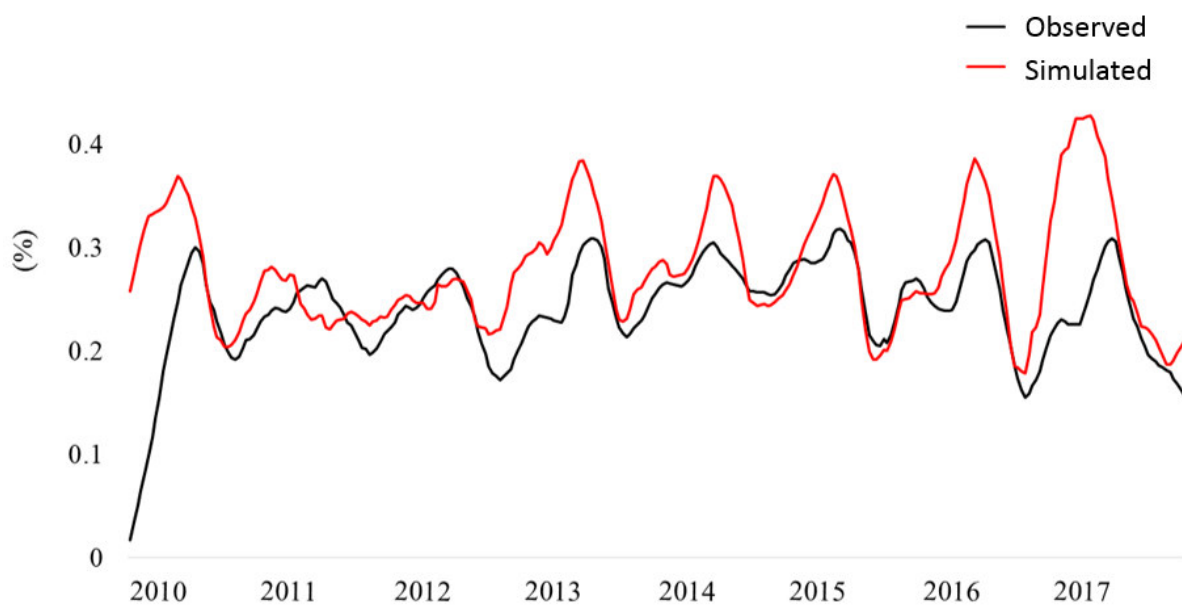


Fig. 4.4. Comparisons between DayCent simulations (red dotted line) and observations (black continuous line) of soil water content (% , 0.3 m) at Torgnon.

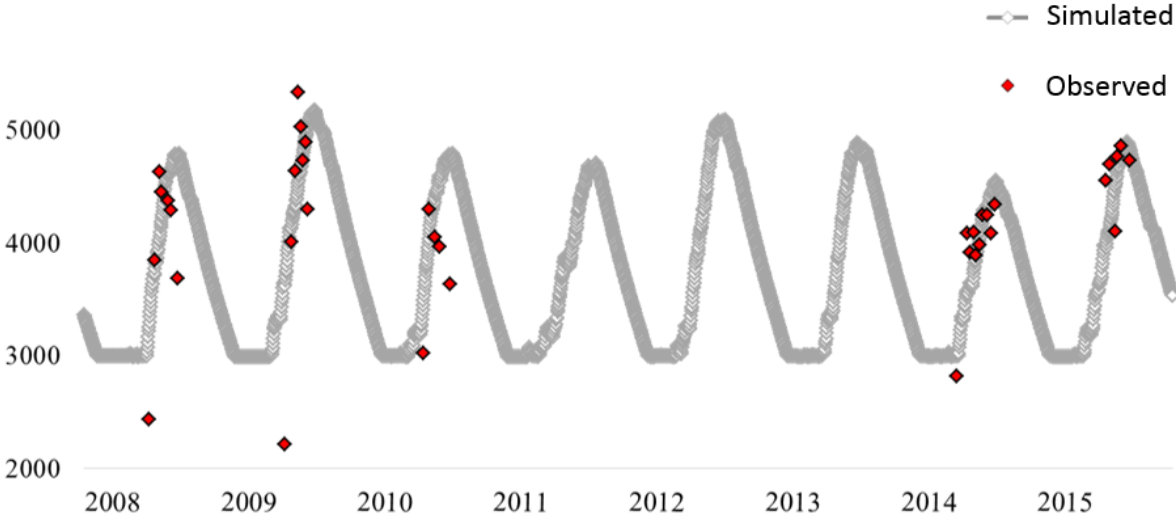


Fig. 4.5. Comparison between DayCent simulations (red dotted line) and observations (black continuous line) of above ground biomass (kg DM ha⁻¹) at Entrelor (Basso).

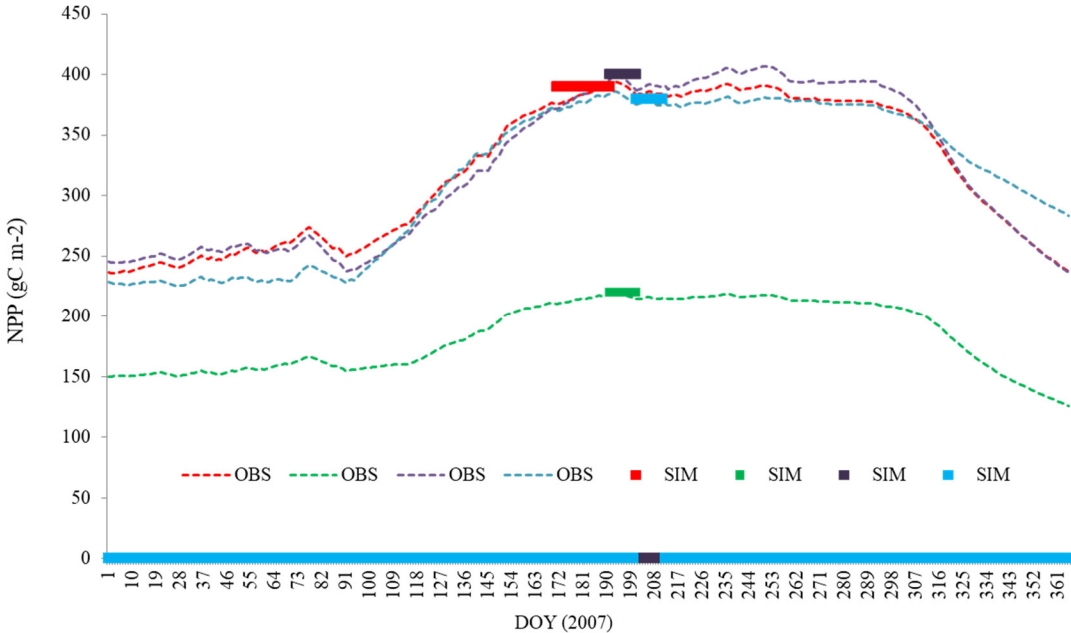


Fig. 4.6. Comparison between DayCent simulations (coloured dotted line) and observations (coloured rectangles) of net primary production (g C m⁻²) at Oisans (year 2007).

4.2 PaSim calibration results

Appendix B reports site-specific inputs, while the list of PaSim vegetation parameters used for calibration are detailed in Appendix C. Figs. 4.7, 4.8 and 4.9 illustrate the calibration results, which show the substantial ability of the model to capture the variability of aboveground biomass (kg DM m⁻²). Some high values cannot be caught by the model but the fluctuations are correctly simulated.

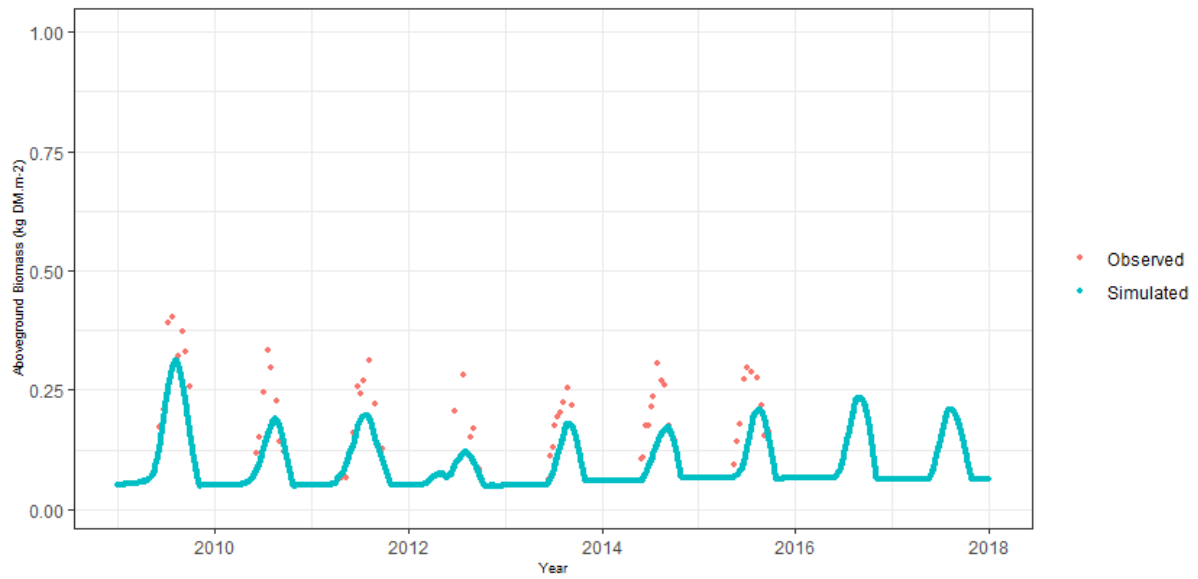


Fig. 4.7. Comparisons between PaSim simulations (blue dots) and observations (brown dots) of aboveground biomass at Torgnon.

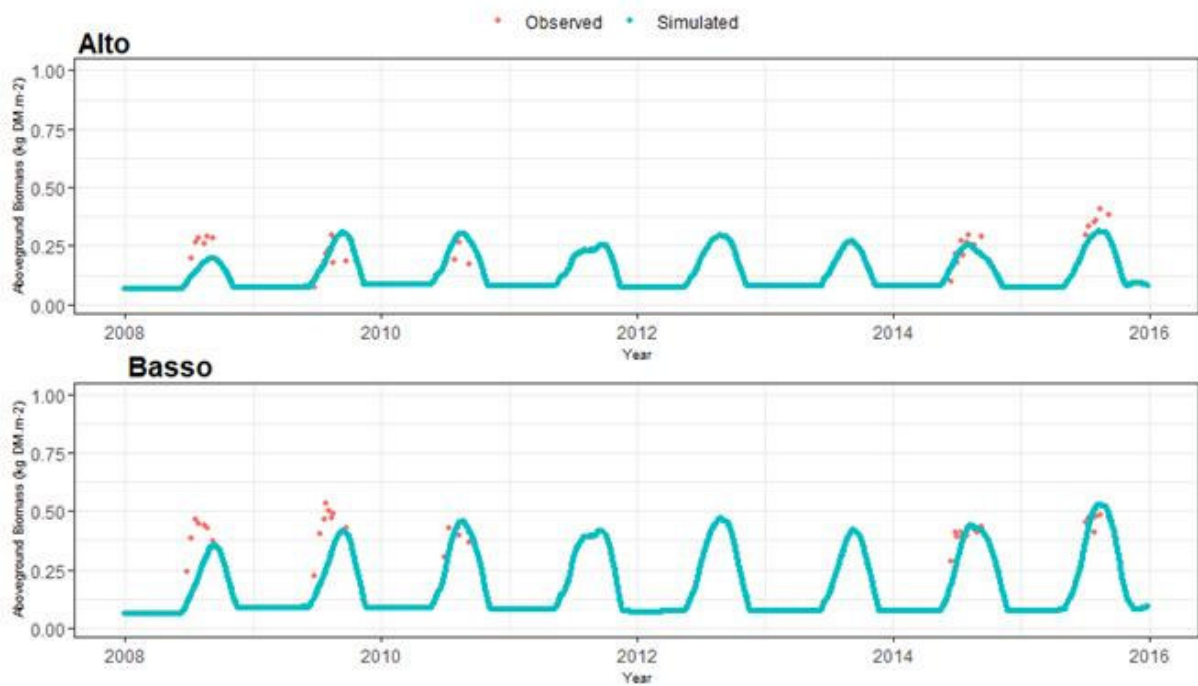


Fig. 4.8. Comparisons between PaSim simulations (blue dots) and observations (brown dots) of aboveground biomass at Entrelor (two sites).

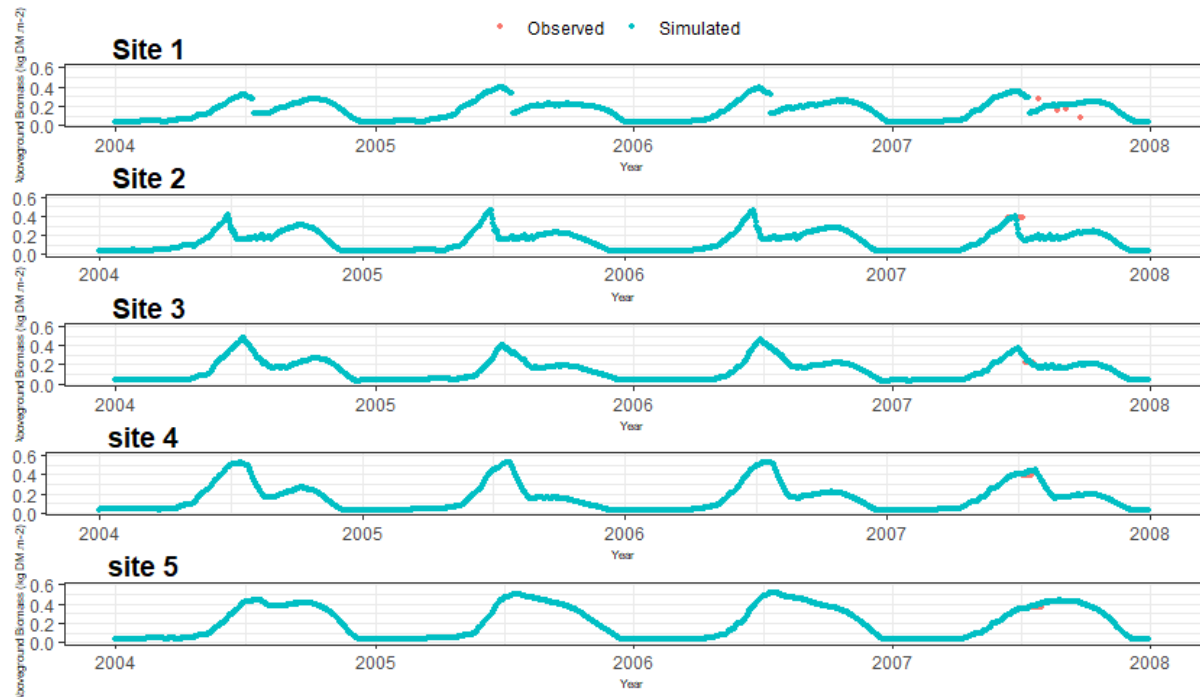


Fig. 4.9. Comparisons between PaSim simulations (blue dots) and observations (brown dots) of aboveground biomass at Oisans (five sites).

These findings must be regarded as preliminary and need to be corroborated by further analysis. In particular, they will be revised after the updated calibration of simulation models against satellite-derived data. Since these simulations were performed with partial datasets, which introduced large uncertainties in the results, to get insight into the sources of these uncertainties, and try to improve the quality of PaSim simulations by allocating model outputs variability to different sources of uncertainty, we carried out some exploratory data analyses. Climate data were first modified to assess the impact of snow cover on vegetation development. Then, we studied the impact of variations in soil texture, pH and soil organic carbon (SOC) content on both aboveground biomass (AGB) and leaf area index (LAI). To better represent the different situations characterising the Alpine pastures (which are not covered by site-specific calibrations), new simulations were performed on typical grassland areas for which valuable vegetation data can be derived from remote-sensing derived NDVI (normalised difference vegetation index) data. For that, we expanded the base of vegetation data for model calibration, by converting remote-sensing derived NDVI data into LAI and AGB in typical grassland areas of the Alps.

5 Sensitivity analysis of PaSim

This section is organised in three parts. Part A assesses the impact of snow cover on the simulated aboveground biomass. Parts B, C and D explore how variations in the soil texture, pH and soil organic carbon (SOC) content, respectively, affect the simulated values of aboveground biomass and leaf area index, as well growing-season dates.

5.1 Impact of snow cover on above ground biomass

In alpine environments, ice and snowpack cover the ground over several months from autumn to spring. On one side, snow cover prevents plants from growing because they are not intercepting the incoming radiation. On the other, water stored by the snowpack is not available for plant use while the melting of snowpack makes available big amounts of water to plants in spring. We assessed the impact on vegetation due to light interception by snow, either alone or along with spring water supply.

5.1.1 Light-interception modification by snow cover

The snow and ice cover prevent the interception of incoming solar radiation by the vegetation canopy. In order to emulate this behaviour, a snow data file was used to indicate the days with snow/ice cover on the ground. We coupled these data to the daily weather radiation file and set incoming solar radiation to zero in the days where snow was present.

As we do not have access to detailed snow datasets in the studied sites, we tested the effect of snow cover on the grassland site of Laqueuille in the Massif Central of France (whose characteristics are similar to the Alps), which is operated by INRAE UREP of Clermont-Ferrand. We refer to Laqueuille because PaSim was already extensively evaluated in previous investigations at this site. The test was designed to compare the simulated aboveground biomass obtained by running the grassland system over multiple years, left ungrazed and unmown, without and with incoming solar radiation (i.e. with or without snow-cover effect). The snow-cover effect was introduced by setting incoming solar radiation to 0 from December the 1st to April the 1st (which is the most probable period with snow on the ground). In Fig. 5.1, we observe a seasonal shift between the two situations along with a decrease of the aboveground biomass in the presence of snow.

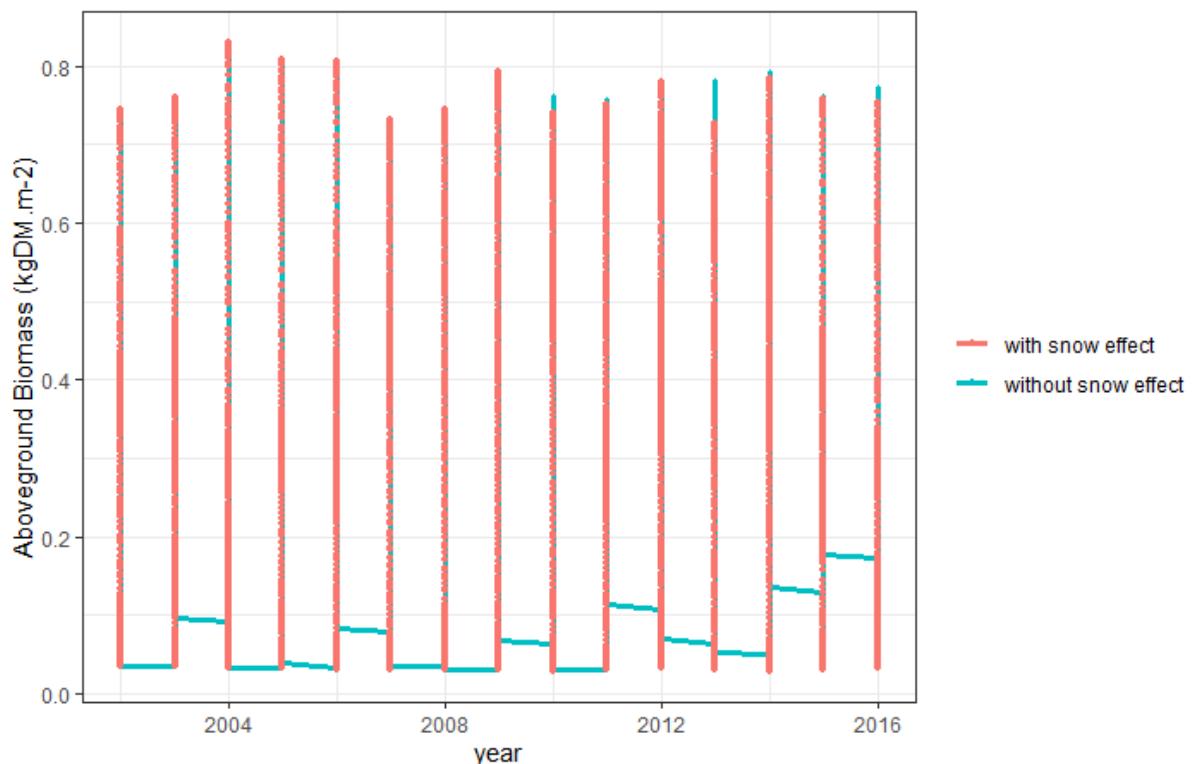


Fig. 5.1. Comparison of simulated aboveground biomass obtained considering or not the snow cover effect.

5.1.2 Water-supply modification by snow melt

The idea here is to emulate the accumulation of water in the form of snow, which is released as snow melts. Considering that water is accumulating from December the 1st to April the 1st, we assumed that the snowpack releases each day over one month (April) 1/30th of the water accumulated during the winter period. We combined the two modification effects (light interception and snow-released water) and then we compared the aboveground biomass simulated, with and without snow-water supply in spring. In Fig. 5.2, we observe a distinct seasonal shift as well as a decrease of biomass associated with winter water retention. From this simulation study, we thus conclude that the effect of snow cover on vegetation is present, which results in a seasonal shift and a slight decrease in biomass.

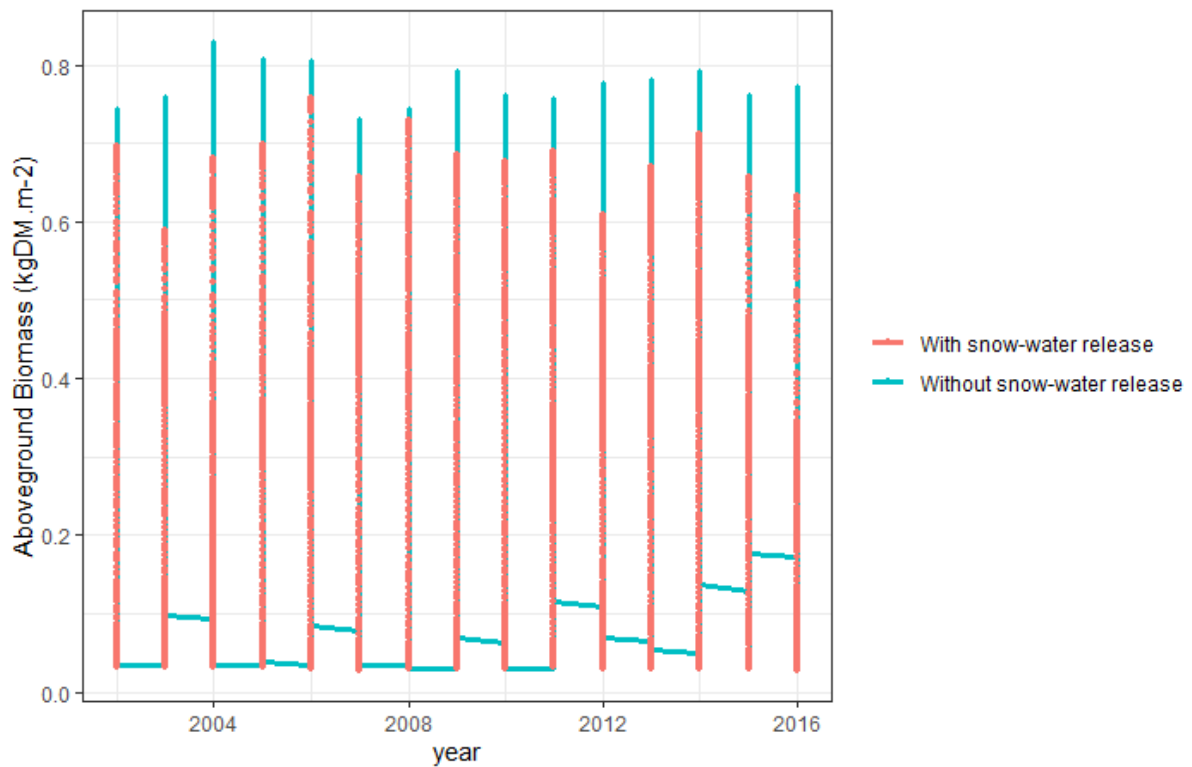


Fig. 5.2. Comparison of aboveground biomass simulated in the presence and absence of water accumulation, and with light-interception effects.

5.2 Impact of soil texture variations on AGB and LAI

The first step was to generate randomly 10000 virtual soils (Fig. 5.3) by using a Latin Hypercube Sampling (LHS).

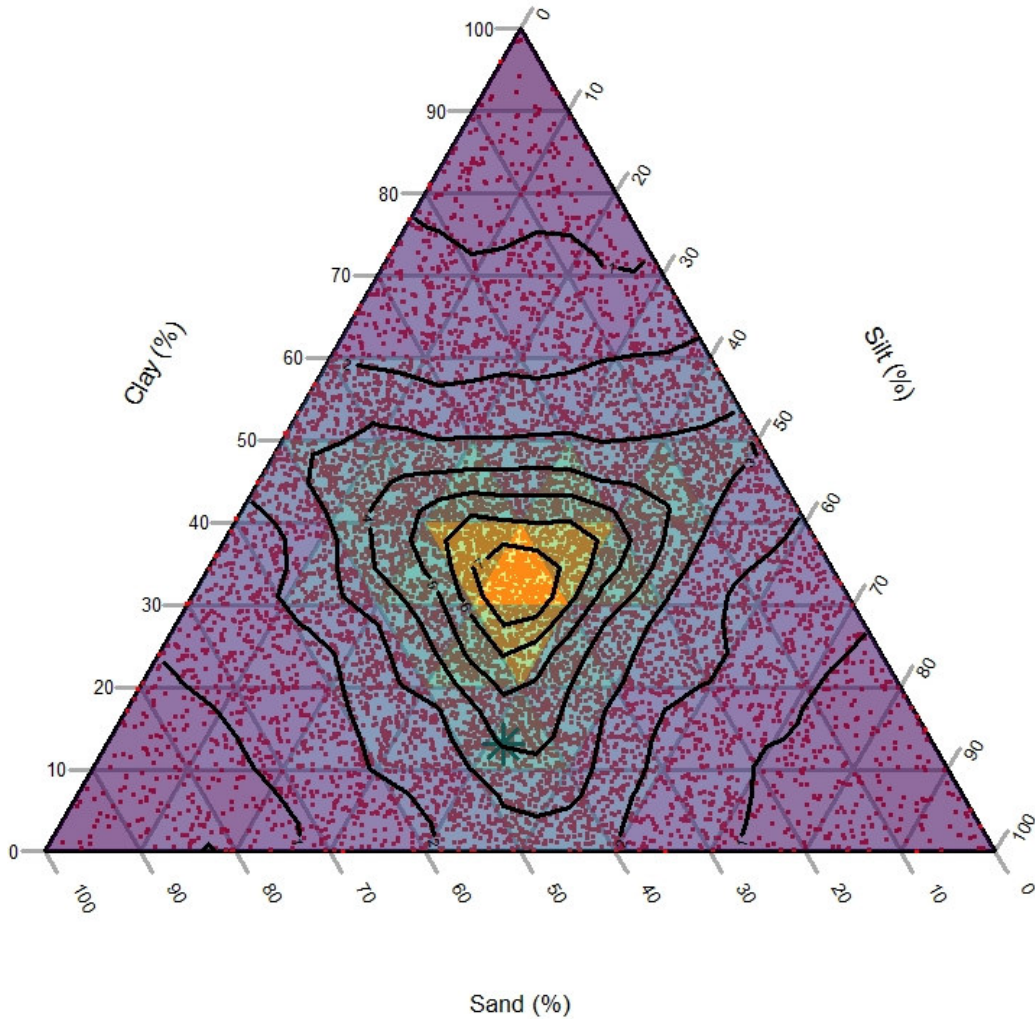


Fig. 5.3. First soil layer texture at Torgnon (a red dot for each of 10000 simulations).

Here is a detailed explanation of how soils were generated. Firstly, by using the LHS method, we have:

$$\{sand_i; silt_i; clay_i\}_{i \in [1; 10000]} \in [0; 1]^3$$

Sand, silt and clay ratios were derived from the available texture data of Torgnon to extrapolate them for the six soil layers of PaSim, i.e.:

$$\begin{aligned} ratio_{sand} &= \{1; 1; 1; 1.090708; 1.152655; 1.488938\} \\ ratio_{clay} &= \{1; 1; 1; 0.610687; 0.351145; 0.1679389\} \\ ratio_{silt} &= \{1; 1; 1; 1.023981; 1.038369; 0.7314149\} \end{aligned}$$

The following was applied to have this ratio for any given layer l :

$$\begin{aligned} sand_{i,l} &= ratio_{sand,l} * sand_i \\ clay_{i,l} &= ratio_{clay,l} * clay_i \\ silt_{i,l} &= ratio_{silt,l} * silt_i \end{aligned}$$

Then, to keep the sum of all the ratios at a given layer equal to 1, ratios were normalised as follows:

$$\text{normalizedSand}_{i,l} = \frac{\text{sand}_{i,l}}{\text{sand}_{i,l} + \text{clay}_{i,l} + \text{silt}_{i,l}}$$

$$\text{normalizedClay}_{i,l} = \frac{\text{clay}_{i,l}}{\text{sand}_{i,l} + \text{clay}_{i,l} + \text{silt}_{i,l}}$$

$$\text{normalizedSilt}_{i,l} = \frac{\text{silt}_{i,l}}{\text{sand}_{i,l} + \text{clay}_{i,l} + \text{silt}_{i,l}}$$

The following textures (Fig. 5.4) were obtained for layers 4, 5 and 6. Applying the ratios observed at Torgnon caused the distribution of sand, silt and clay to converge to the Torgnon values.

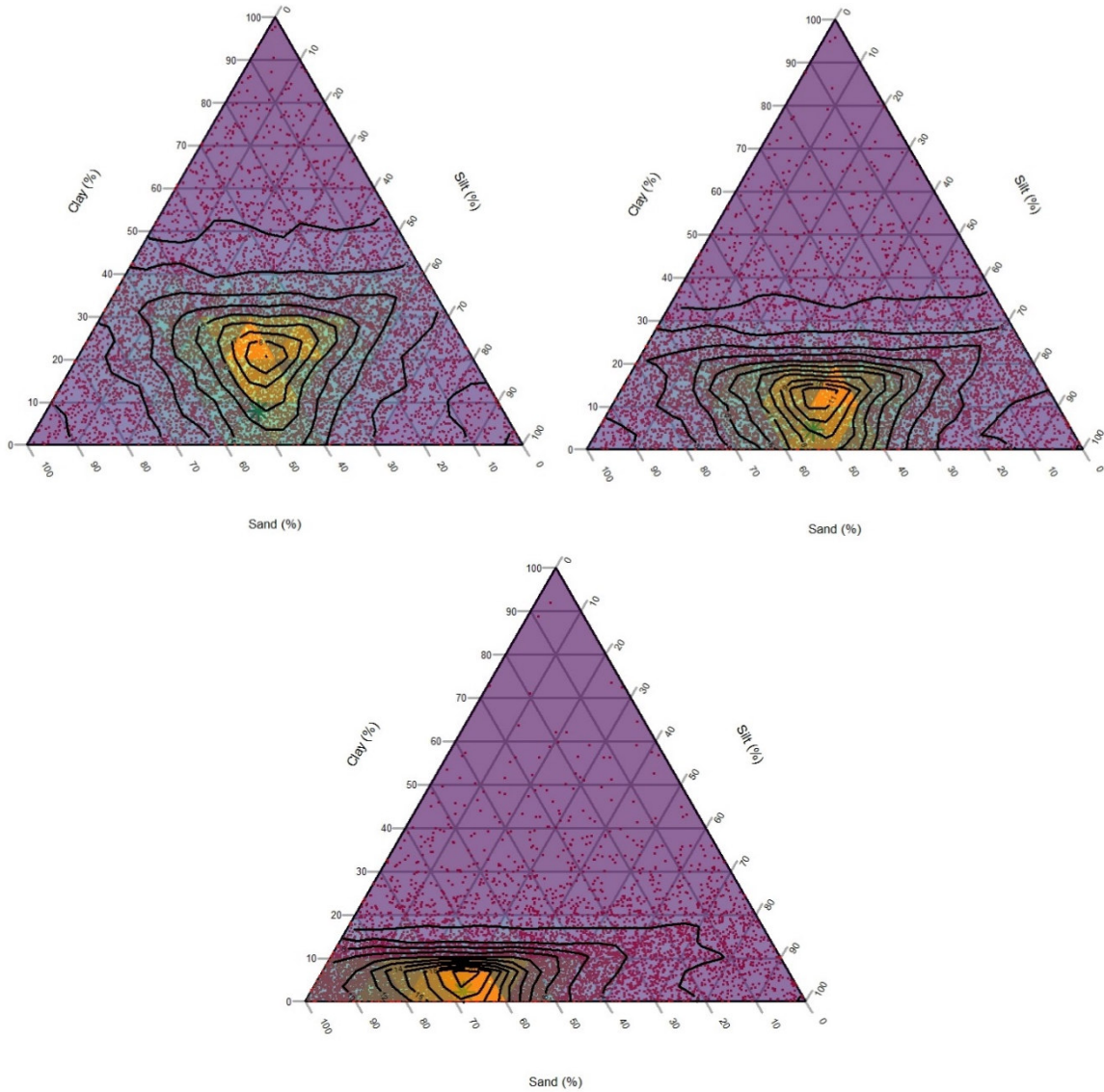


Fig. 5.4. Texture distribution for layers 4, 5 and 6.

However, the 0-30 cm layer remains well explored as shown in the Fig. 5.5.

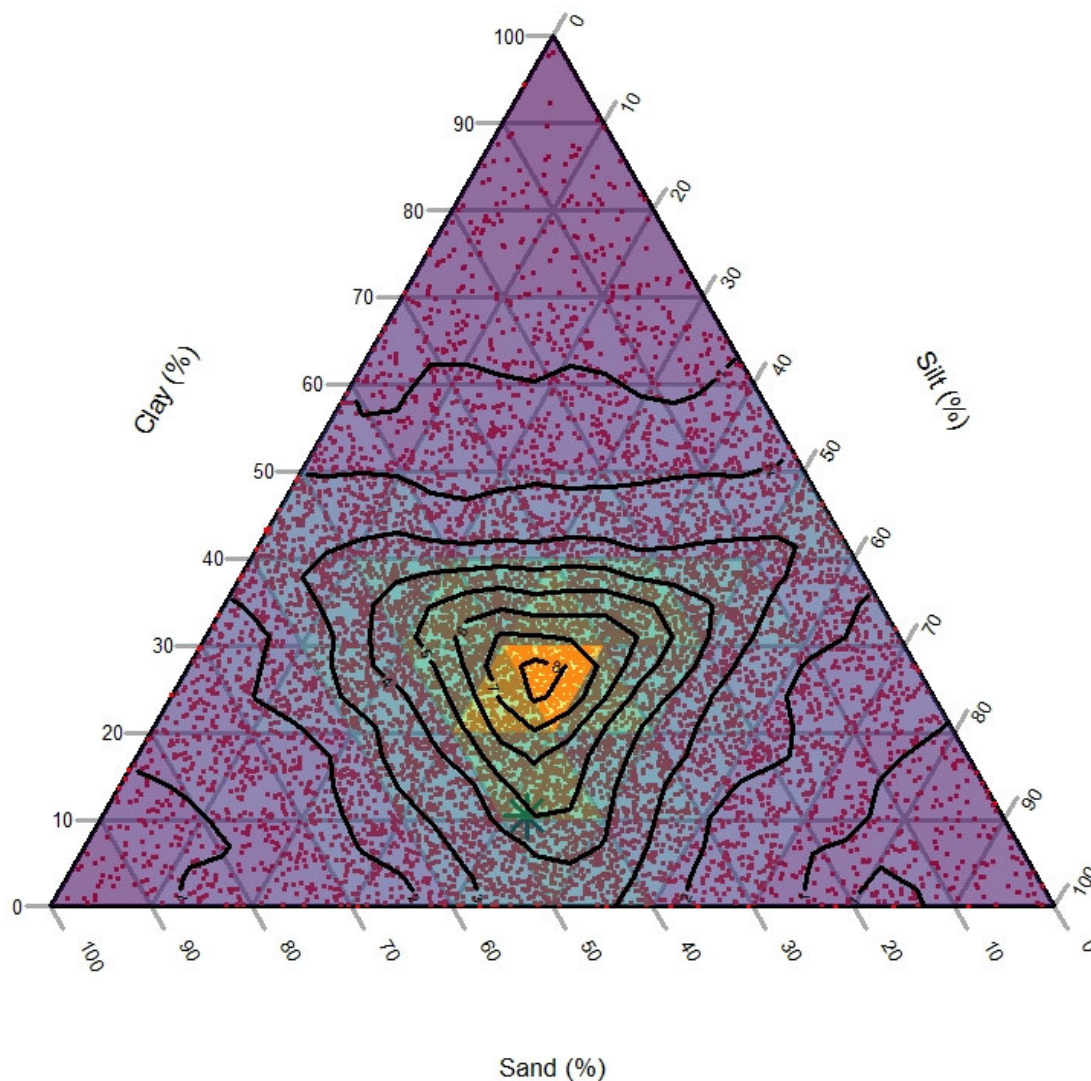


Fig. 5.5. Texture distribution for the 0-30 cm layer.

The pH value was kept to the constant value of 5.14. We estimated all other soil variables in each layer by using internal routines for:

- Bulk density
- Saturated soil water content
- Air entry potential
- Saturated hydraulic conductivity
- Field capacity
- Plant wilting point

The SOC value was re-initialised for each simulation.

Finally, the initial soil C and N stocks were recalculated based on the estimated bulk density (the organic carbon content was considered constant).

The outputs studied were growing-season dates (start of growth, max of growth, end of growth) AGB and LAI.

5.2.1 Growth start date

The growth start date is the first date when the aboveground biomass (AGB) is greater than 0.1 kg DM m⁻², i.e. 1 t DM ha⁻¹. In this way, we assessed if, under certain textures, grassland vegetation started to grow earlier or later.

Interannual mean of growth start date (AGB>0.1 kgDM/m²)

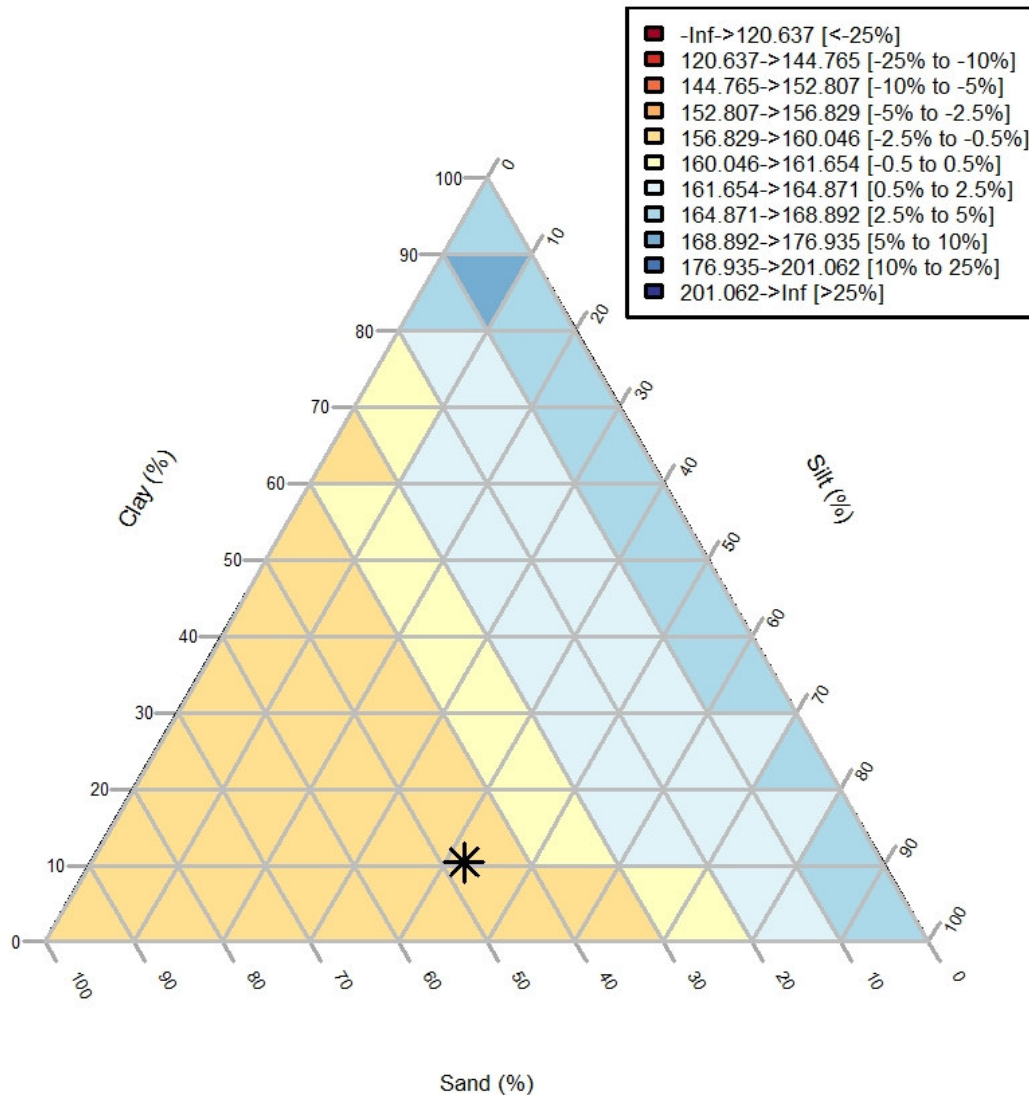


Fig. 5.6. Mean start date of growing season.

In Fig. 5.6, as for all the following figures, we used texture values in the 0-30 cm soil layer. Colours range from dark red for below average values ($\leq 75\%$ of the average) to dark blue for above average values ($\geq 125\%$ of the average) to yellow when they were equivalent to the average (between 99.5% and 100.5% of the average). We can see that a variation of $\pm 20\%$ of the three texture components around the Torgnon values is not leading to a significant shift in the growth start date. It is noteworthy that sand is the main driver to explain the growth start date and that an earlier start of vegetation growth tends to be induced by sandy soils.

We then looked at the variations around this inter-annual average by representing the coefficients of variation.

Interannual coefVariation of growth start date (AGB>0.1 kgDM/m²)

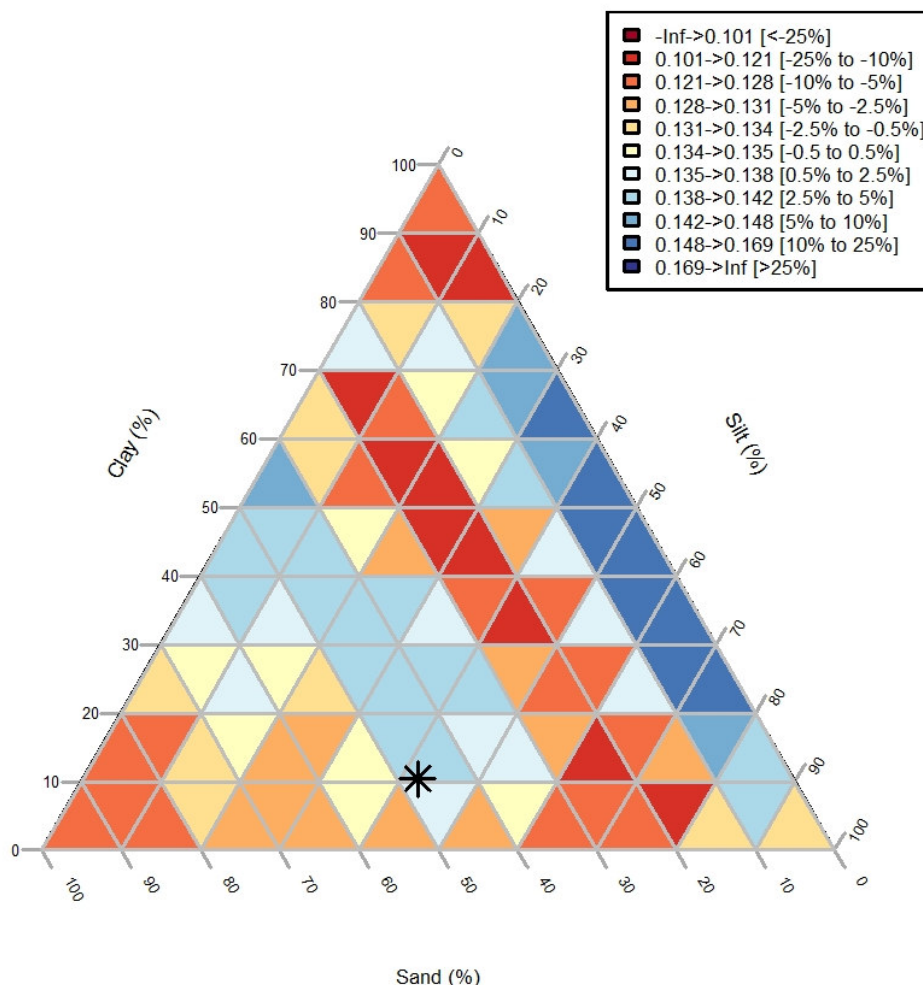


Fig. 5.7. Coefficient of variation of growth start date.

We can note (Fig. 5.7) that it is difficult to find an explanatory scheme, denoting the important intra-annual variability of the growth start date (mean CV ~0.135), likely explained by meteorological variability. However, it can be noted that a poorly sandy soil (>10% sand) seems to be more influential.

5.2.2 Growth end date

In order to get an idea of the length of the growing season, we looked at the last day of growth, i.e. with aboveground biomass greater than 0.1 kg DM m⁻².

Interannual mean of last growth date (AGB>0.1 kgDM/m²)

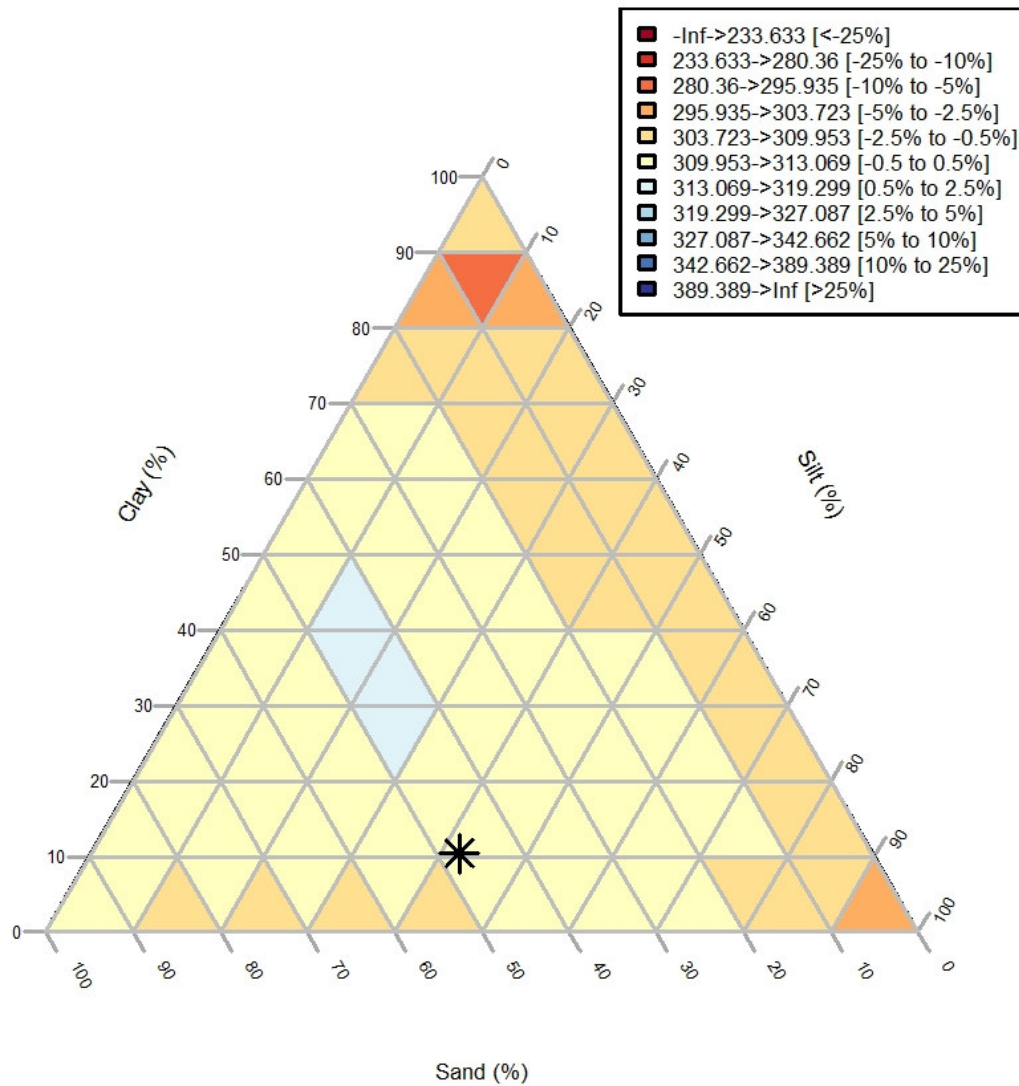


Fig. 5.8. Mean end date of growing season.

It can be seen here (Fig. 5.8) that the date when vegetation stops growing is relatively insensitive to changes in texture, except for very clayey and/or low sandy soils.

Interannual coefVariation of maximum growth date

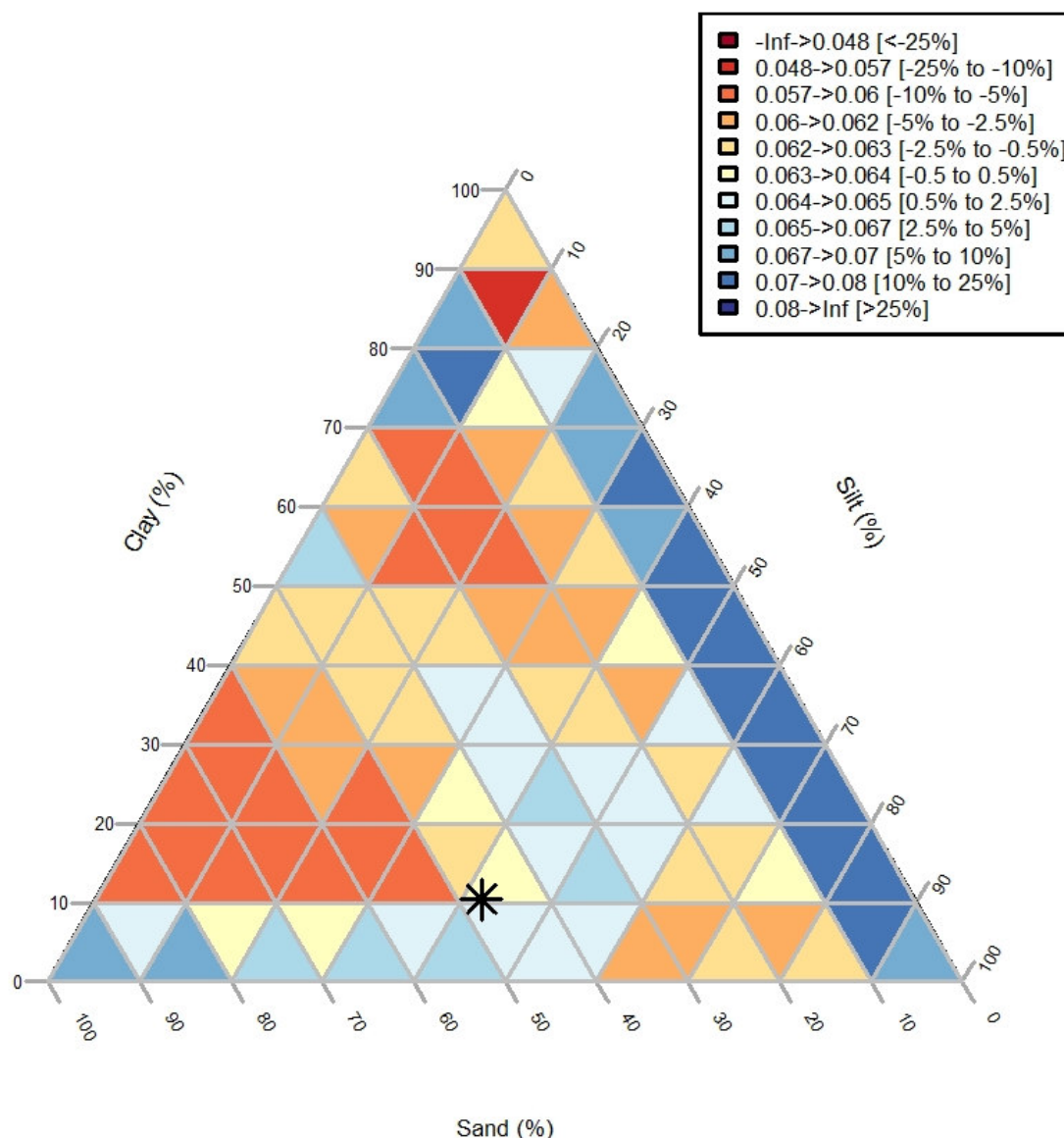


Fig. 5.9. Coefficient of variation of growth end date.

As with growth start dates, there is no explanatory pattern emerging except that low sandy soils appear to be more sensitive. The average CV (Fig. 5.9) is however twice as low as for the growth start date, which seems to indicate that whatever the growth start dates are, the end dates are more stable.

5.2.3 Date of maximum growth

In order to get an idea of the optimum of the growing season, we looked at the date when the AGB achieves its peak.

Interannual mean of maximum growth date

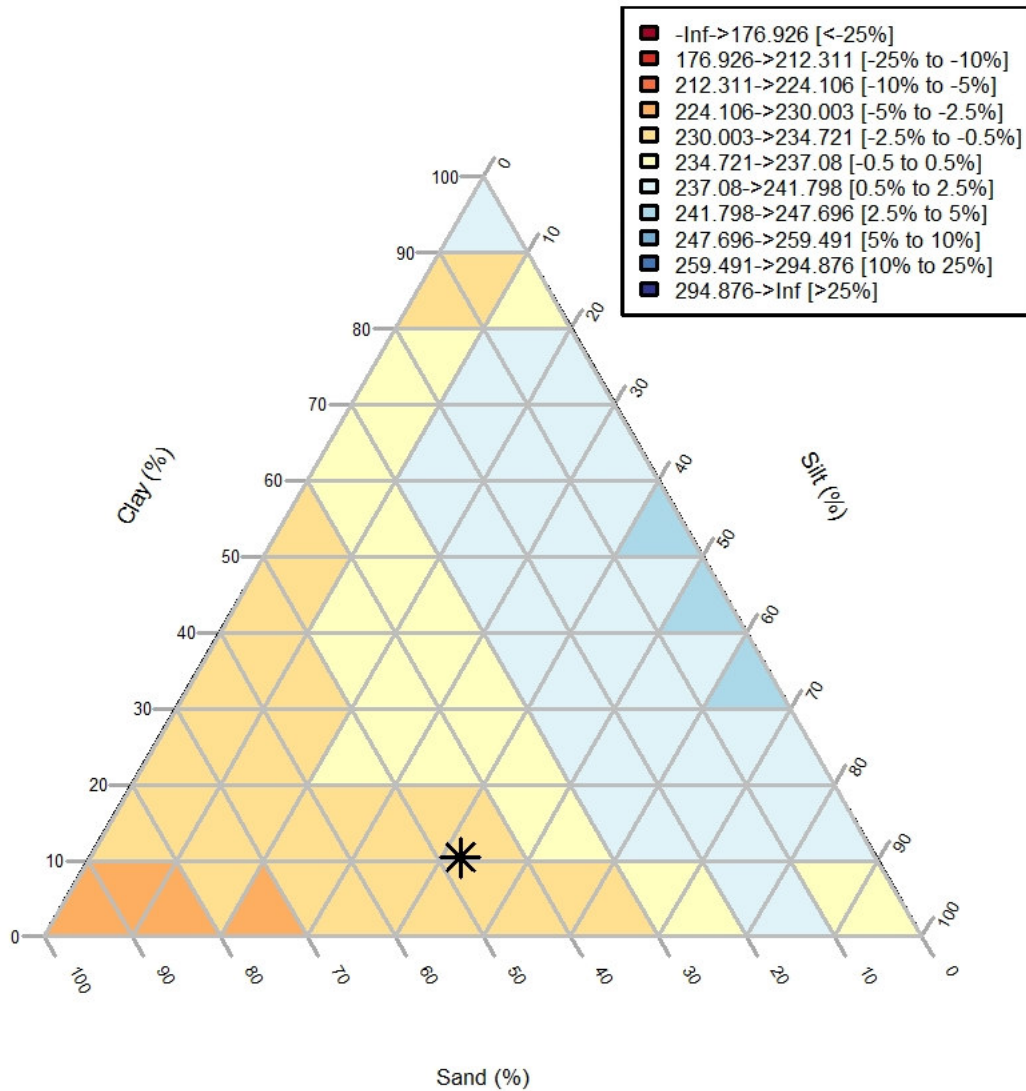


Fig. 5.10. Mean date of maximum growth.

The pattern distinctly shows that the more the soil is sandy, the sooner the vegetation is at its optimum (Fig. 5.10).

Interannual coefVariation of maximum growth date

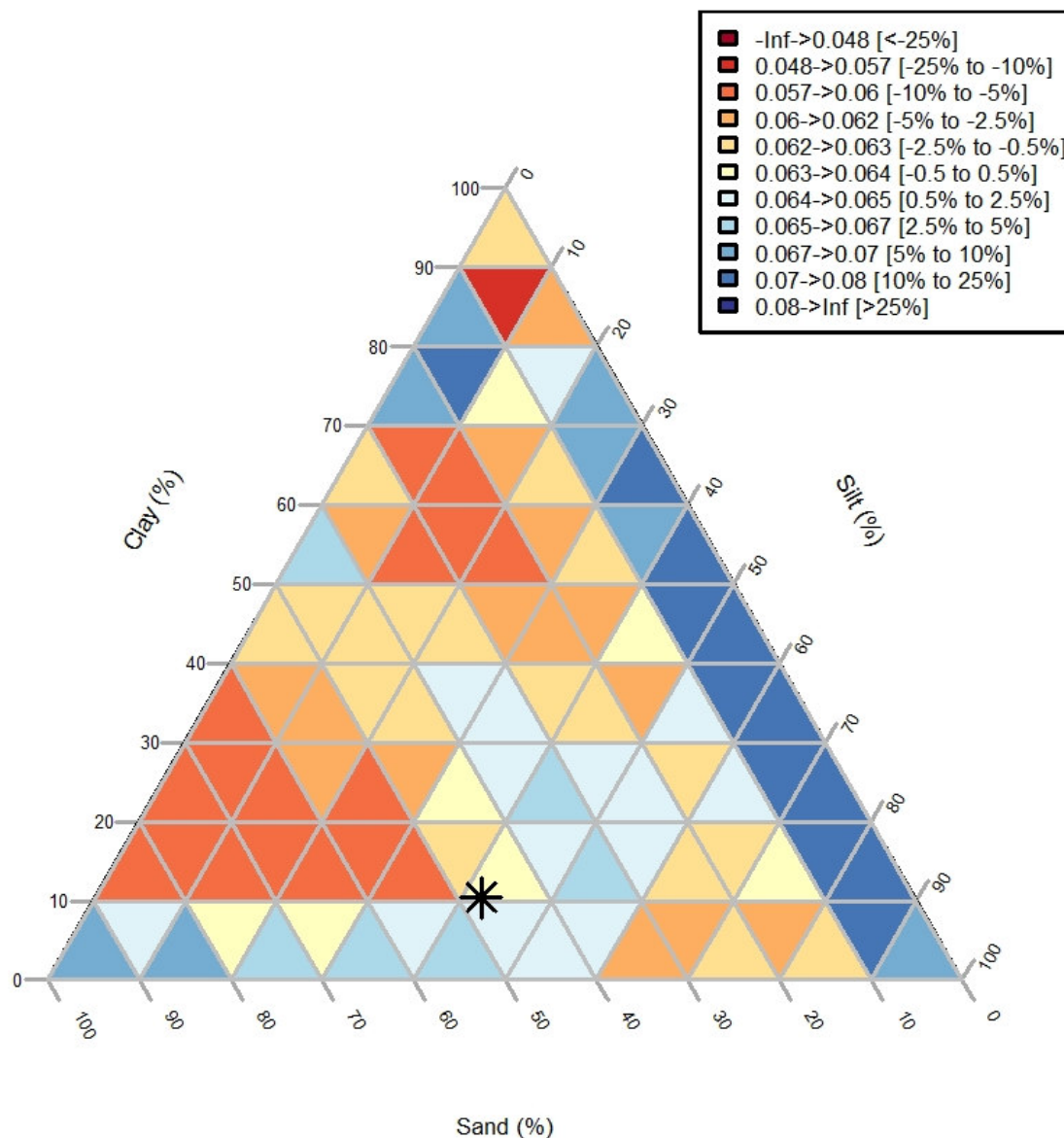


Fig. 5.11. Coefficient of variation of the date of maximum growth.

Low sandy (<10%) and low silty (<30%) soils appear to be most influential. The average CV is low (~0.063), indicating that the date of AGB peak is not changing much with the interannual weather variability (Fig. 5.11).

5.2.4 Mean AGB

Interannual mean of mean AGB (kgDM/m²)

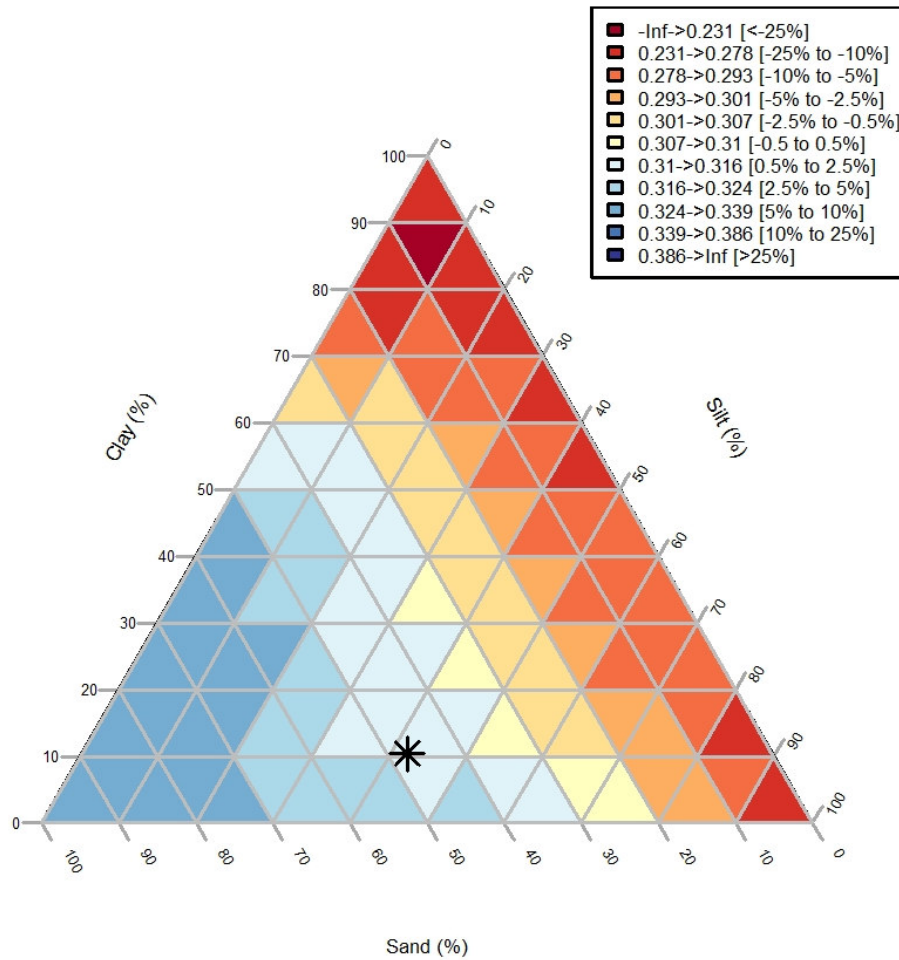


Fig. 5.12. Mean AGB (kg DM m⁻²).

We observed a distinct pattern towards an increasing AGB with sandy soils (Fig. 5.12). We then looked at the variations around this inter-annual average by representing the coefficients of variation (Fig. 5.13).

Interannual coefVariation of mean AGB (kgDM/m2)

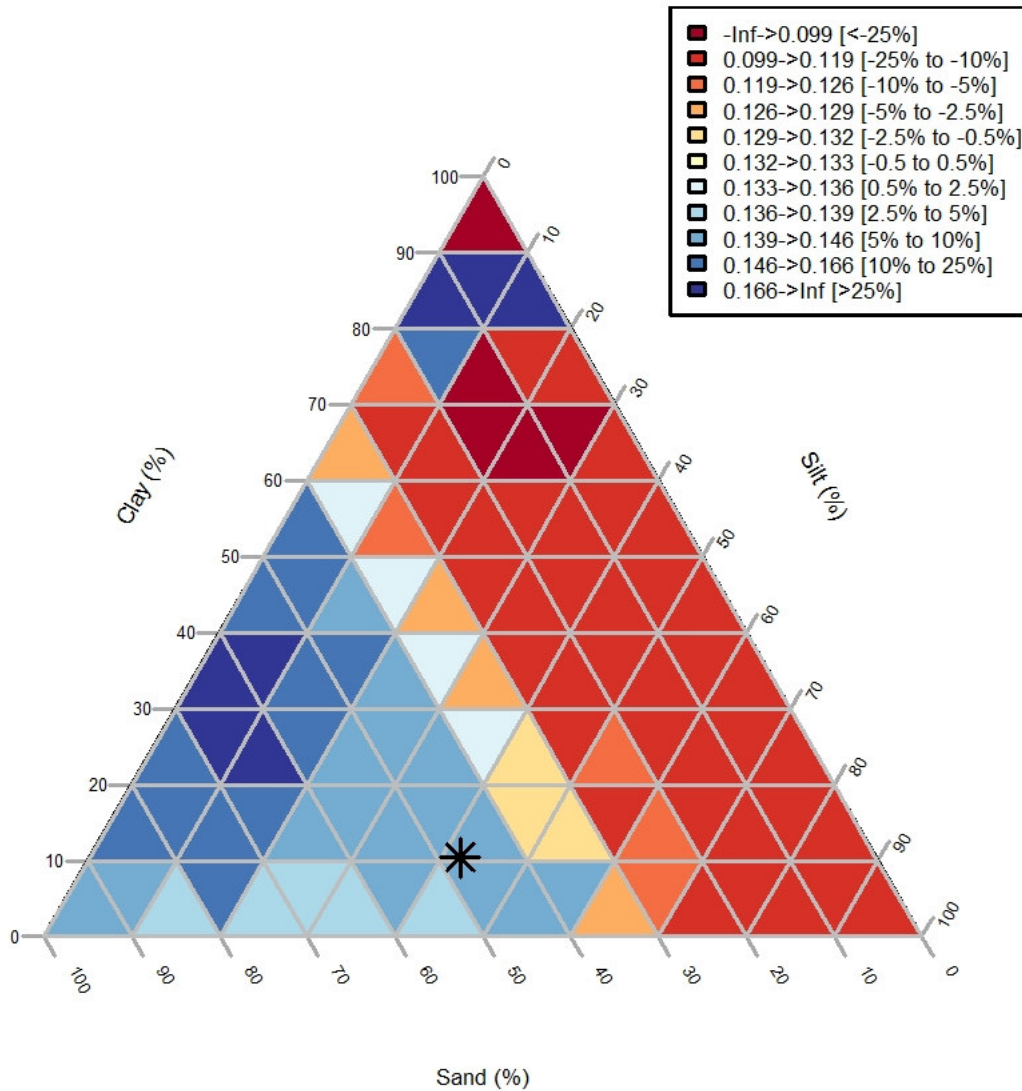


Fig. 5.13. Coefficient of variation of mean AGB.

Low sandy soils (sand<20%) seem to be more resilient to interannual variations. Moreover, AGB on low silty soils appears more sensitive to year-by-year fluctuations of weather conditions.

5.2.5 Maximum AGB

Interannual mean of max AGB (kgDM/m²)

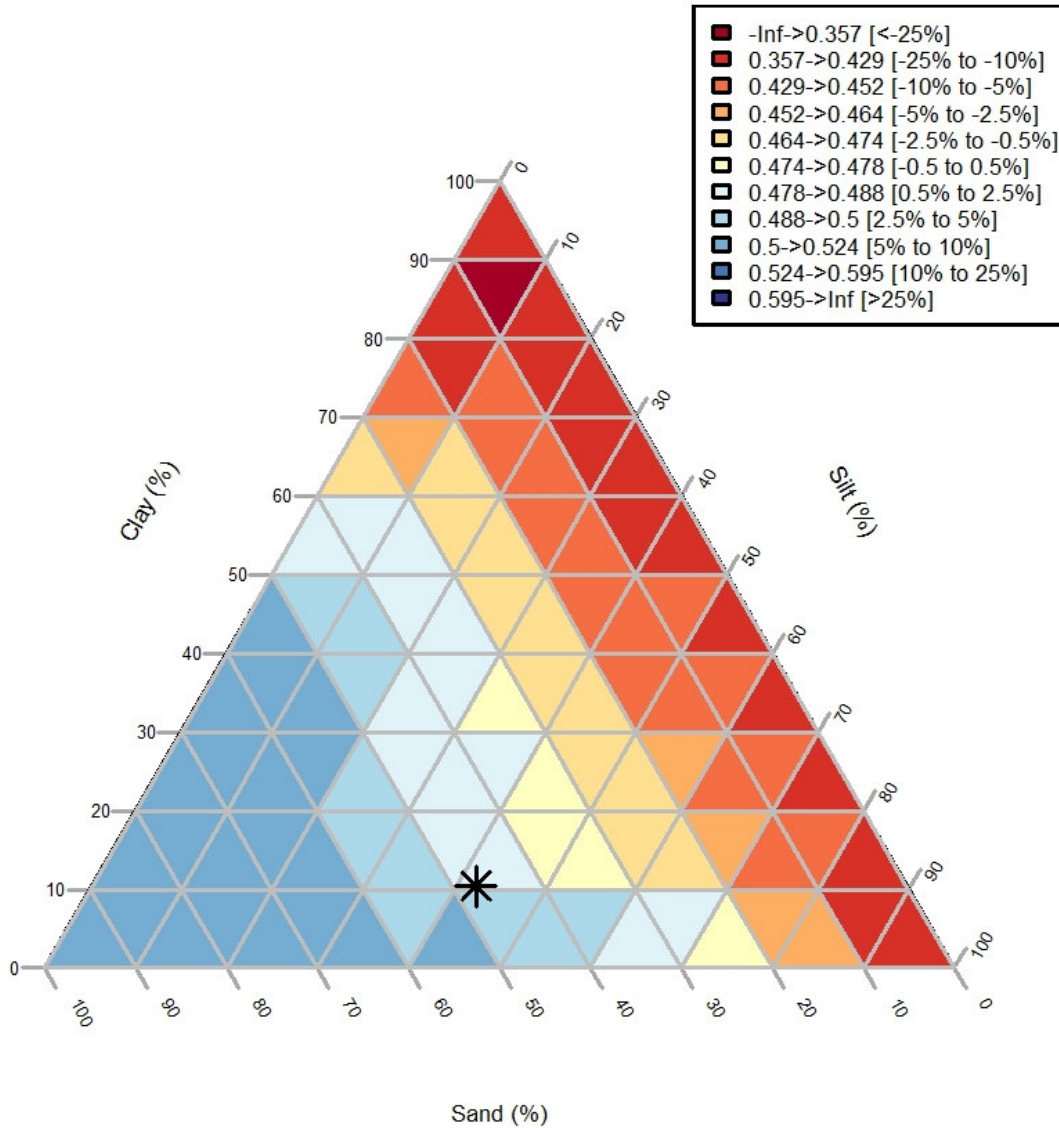


Fig. 5.14. Maximum AGB (kg DM m⁻²).

A distinct pattern is that the more the soil is sandy, the greater the maximum AGB is. It confirms the pattern found for the mean AGB (Fig. 5.14).

Interannual coefVariation of max AGB (kgDM/m2)

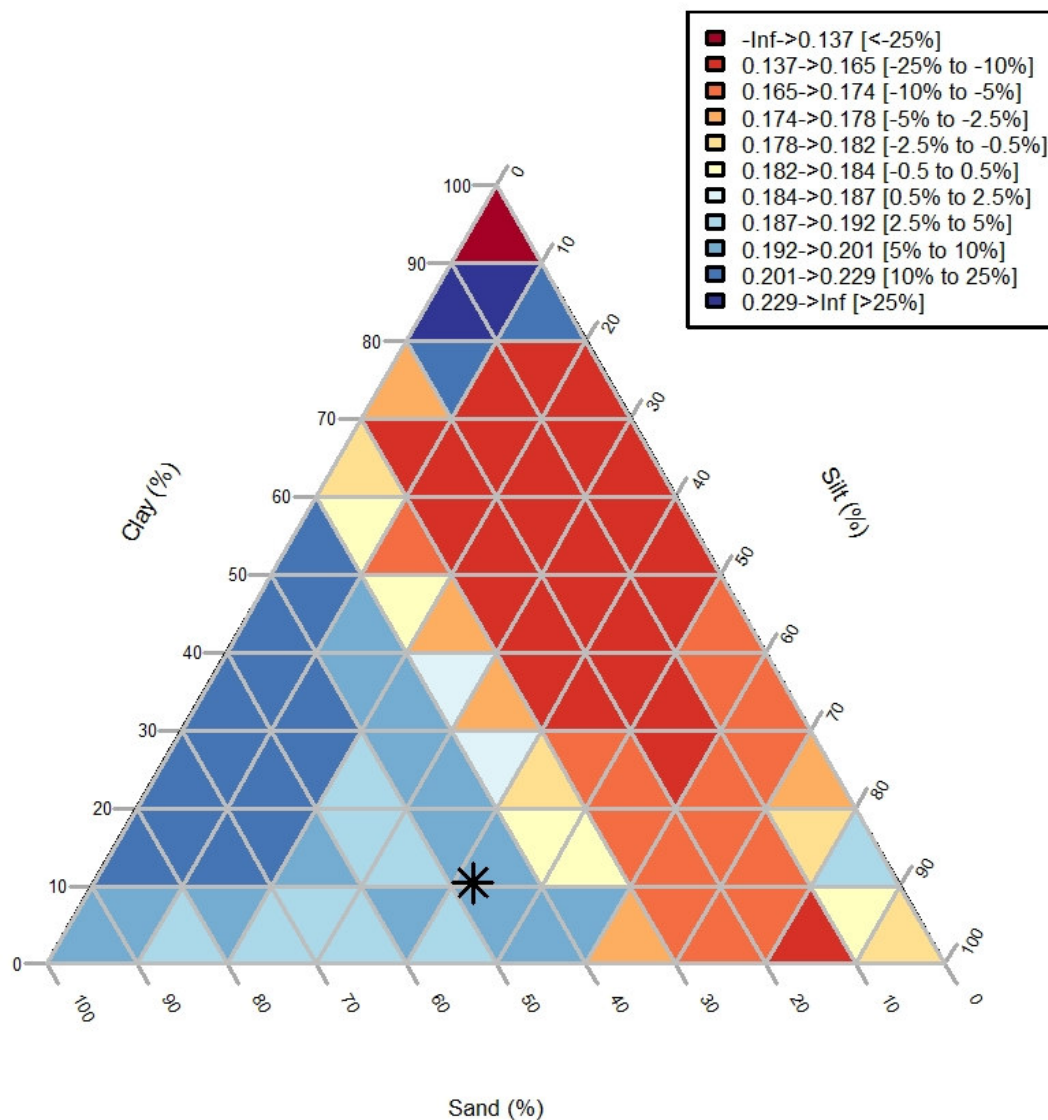


Fig. 5.15. Coefficient of variation of maximum AGB.

Maximum AGB on low sandy soils (sand<30%) seem more resilient to interannual weather variations (Fig. 5.15). Moreover, low silty soil seems to be more sensible to meteorological variations. It confirms the scheme from the mean AGB.

5.2.6 Mean LAI

Interannual mean of mean LAI (m²/m²)

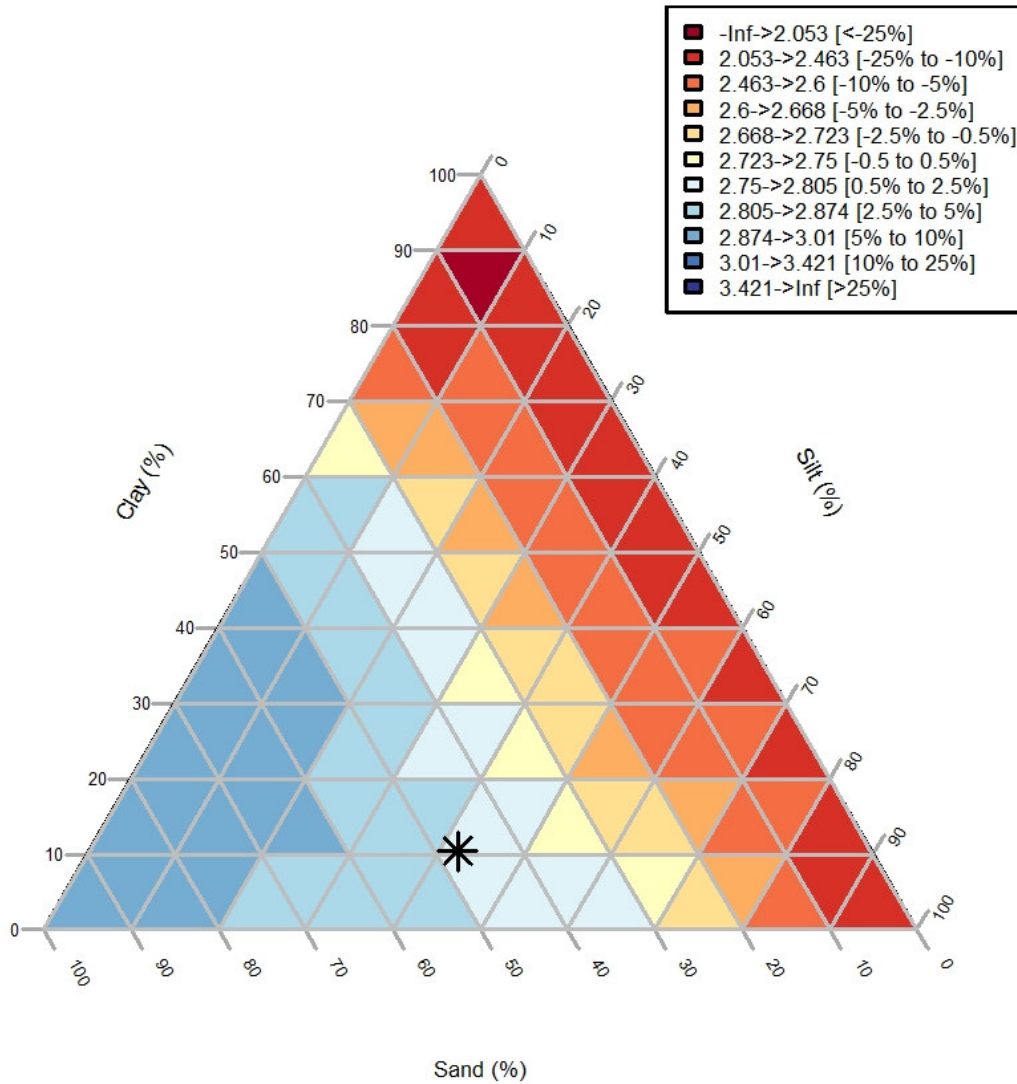


Fig. 5.16. Mean LAI (m² m⁻²).

Also here (Fig. 5.16), the more the soil was sandy the more it was suitable for leaf development. Moreover, an optimum could be identified in an area where sand was greater than 50% and silt varied between 0 and 20%.

Interannual coefVariation of mean LAI (m2/m2)

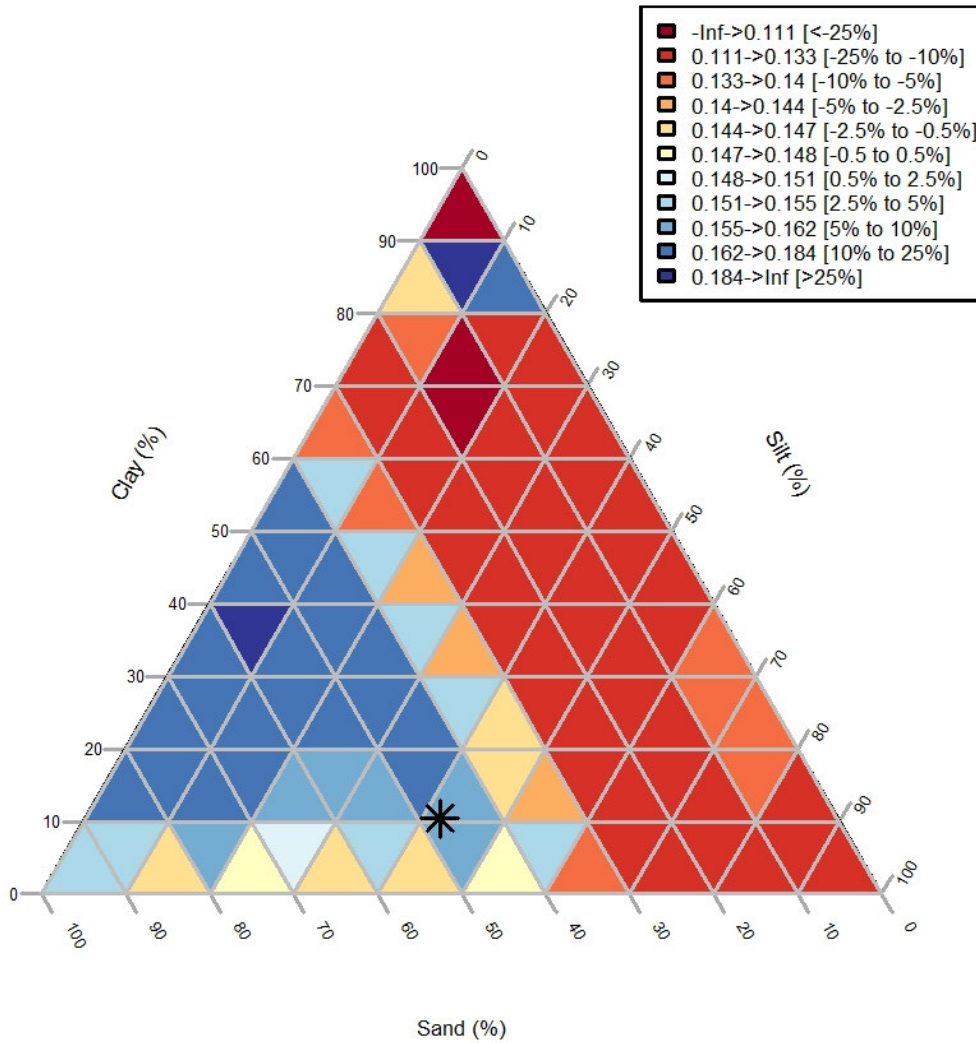


Fig. 5.17. Coefficient of variation of mean LAI.

Mean LAI appeared more resilient to yearly variations on low sandy soils (sand<30%). This confirms the results obtained with mean AGB (Fig. 5.17).

5.2.7 Maximum LAI

Interannual mean of max LAI (m²/m²)

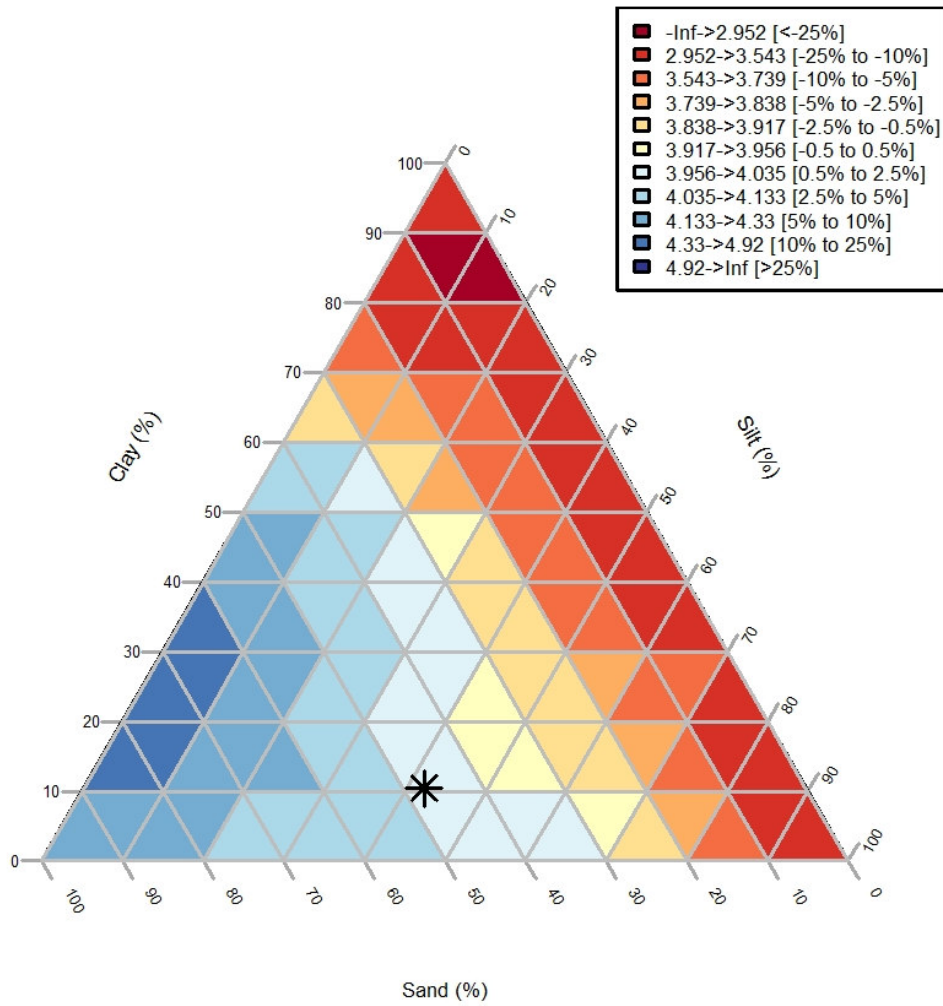


Fig. 5.18. Maximum LAI (m² m⁻²).

The pattern of response clearly indicates that the more the soil is sandy, the greater the LAI is (Fig. 5.18). Moreover, an optimum can be found if the sand percentage is between 60 to 90% and the silt percentage between 0 to 10%.

Interannual coefVariation of max LAI (m2/m2)

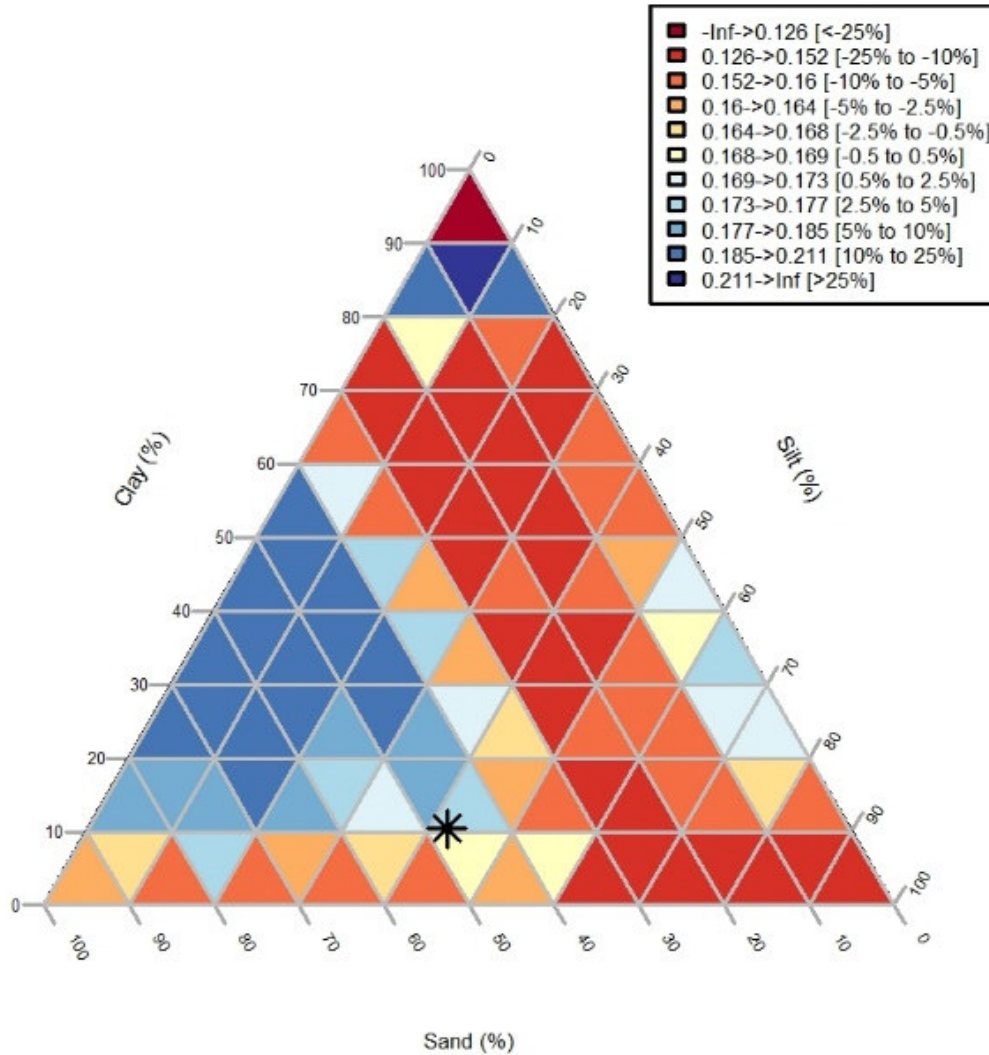


Fig. 5.19. Coefficient of variation of maximum LAI.

In Fig. 5.19, Maximum LAI appears more resilient to interannual weather variations on low sandy soils (<30%). Moreover, the response obtained on low silty soil seems to be more sensitive to meteorological variations.

To conclude for this study, the overall results indicate that, according to PaSim simulations, sandy soils are more productive (aboveground biomass, LAI, length of the vegetation growth season) and less resilient to inter-annual weather conditions. More specifically, indicate that uncertainties in soil texture in the range of $\pm 20\%$ are acceptable as they are not expected to influence significantly the vegetation response.

5.3 Impact of pH variations on AGB and LAI

In order to study the impact of pH variation, we launched 21 simulations by varying pH from 4 to 8 with a step of 0.2 (as initial value, we refer the Ph of Torgnon, equal to 5.14).

5.3.1 Growth start date

As we did with texture, we first computed the growth start date, i.e. the first date when the aboveground biomass (AGB) is greater than 0.1 kg DM m^{-2} (1 t DM ha^{-1}). In this way, we determined if some pH values allow the vegetation to start its growth earlier or later.

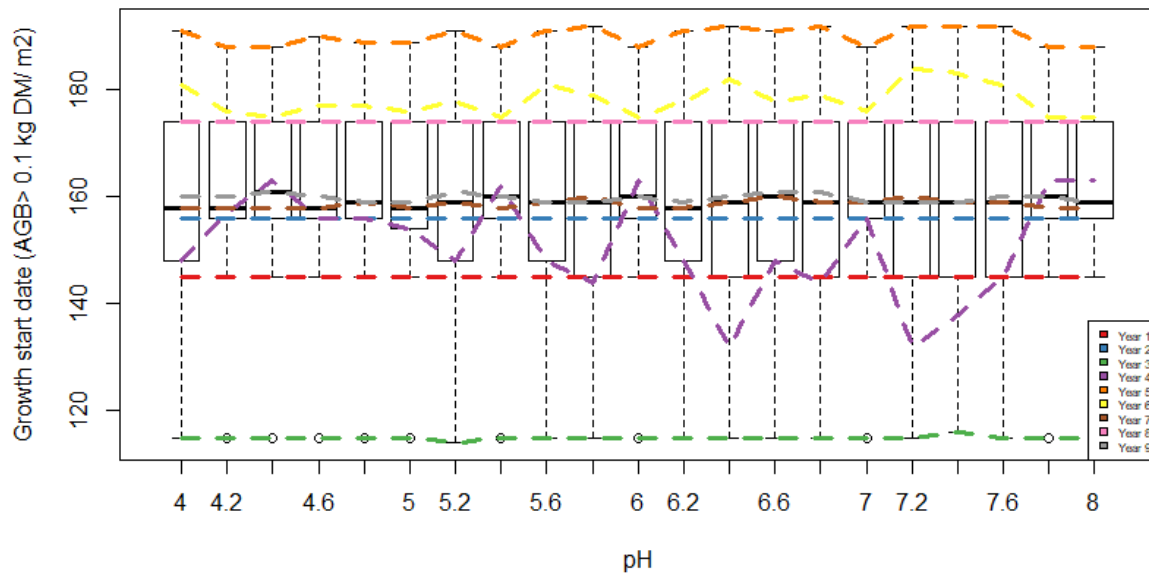


Fig. 5.20. Variation of growth start date with pH and by year.

From Fig. 5.20, we conclude that pH variations do not result into a significant shift in the growth start date. The median date is between days 160 and 162. However, important fluctuations are visible at year 4.

5.3.2 Growth end date

We looked at the last day when AGB is greater than 0.1 kg DM m^{-2} to get an insight into the length of the growing season.

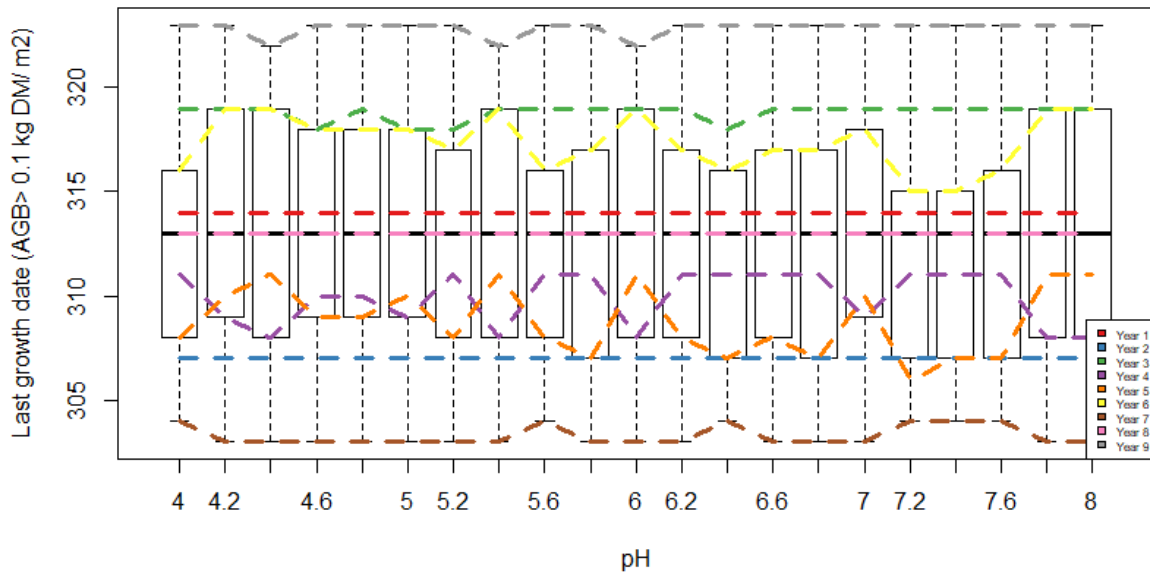


Fig. 5.21. Variation of growth end date with pH and by year.

From Fig. 5.21, it emerges that the last growth date is relatively insensitive to pH variations. The median is relatively stable around day 313 for the different pH values (minimum at day 303, maximum at day 323). Exceptions are years 4, 5 and 6, for which some higher fluctuations are visible.

5.3.3 Date of maximum growth

This is the date when the AGB achieves its maximum value.

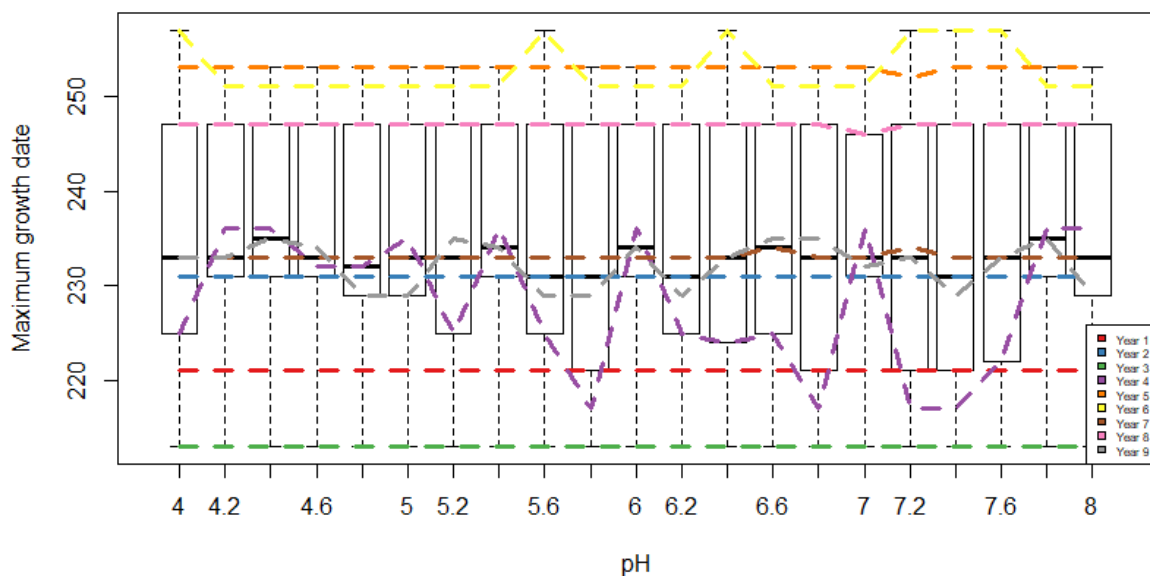


Fig. 5.22. Variation of the date of maximum growth with pH and by year.

The pattern of Fig. 5.22 distinctly indicates that pH variations do not result into a significant shift in the growth optimum date, with the exception of year 4. The median varies between day 233 and 235 days, within a range from day 213 and day 257.

5.3.4 Mean AGB

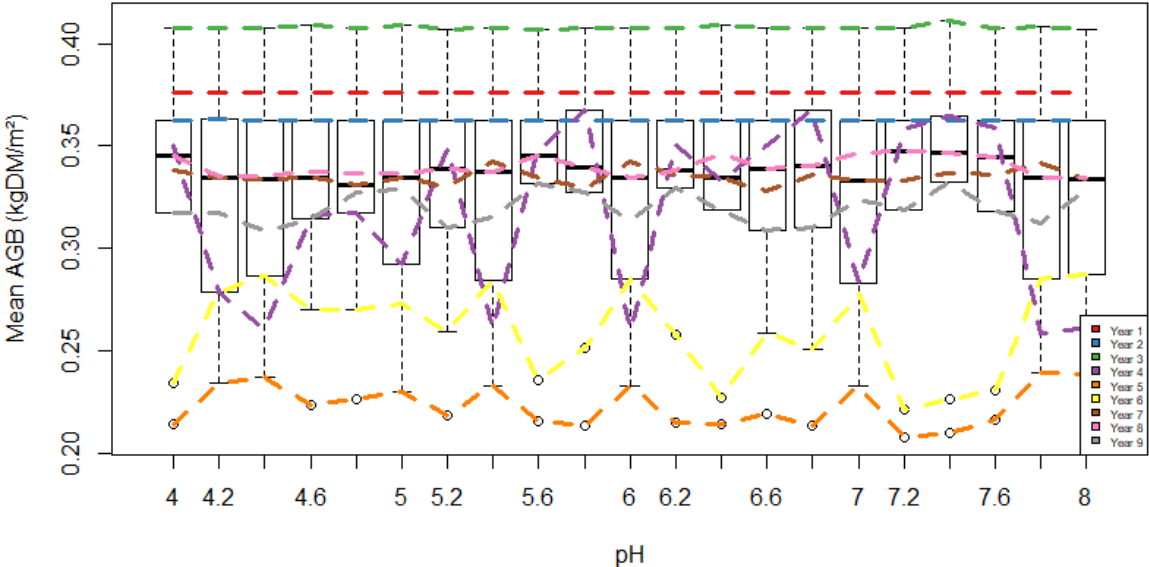


Fig. 5.23. Variation of mean AGB (kg DM m⁻²) with pH and by year.

The overall pattern of Fig. 5.23 is that AGB is not sensitive to pH variations. The median is between 0.33 and 0.35 kg DM m⁻². We can see that it is only over years 4 and 6 that distinct, apparently complementary variations emerge.

5.3.5 Maximum AGB

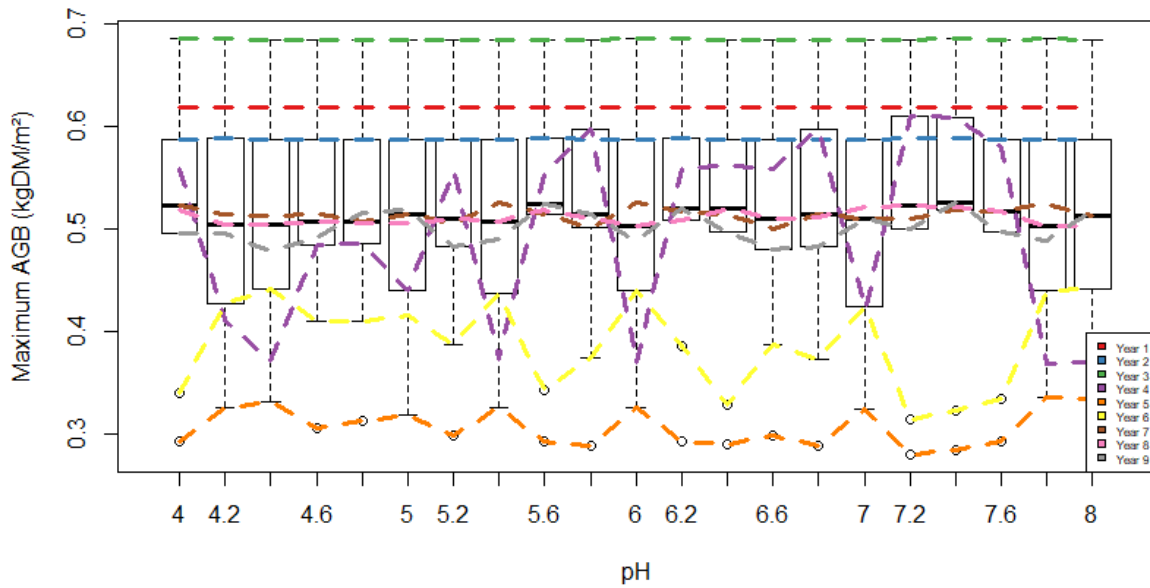


Fig. 5.24. Variation of maximum AGB (kg DM m⁻²) with pH and by year.

According to Fig. 5.24, the maximum AGB does not vary regarding pH with the exception of years 4 and 6.

5.3.6 Mean LAI

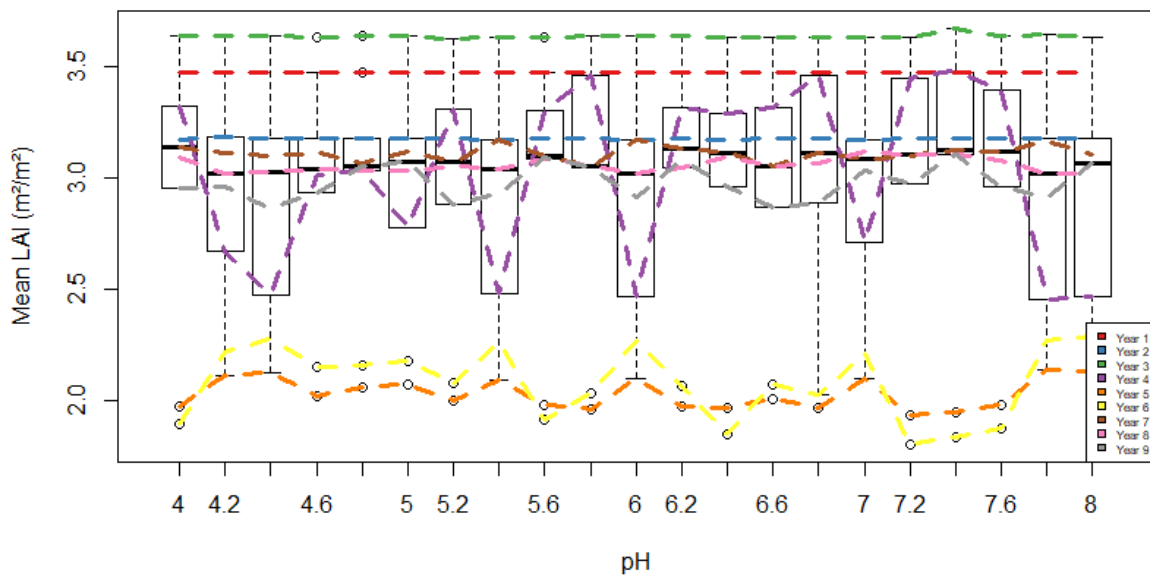


Fig. 5.25. Variation of mean LAI (m² m⁻²) with pH and by year.

In Fig. 5.25, there is a great asymmetry in the underlying distribution of the data. However, the median only varies by ±0.1 and, with the exception of year 4, mean LAI is not sensitive to variations in pH.

5.3.7 Maximum LAI

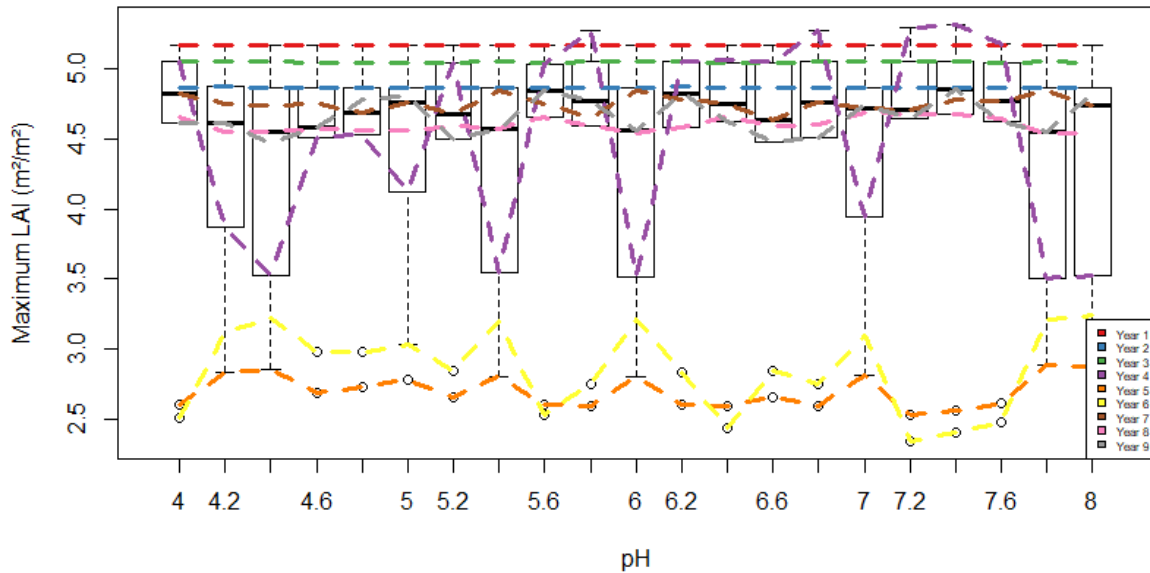


Fig. 5.26. Variation of maximum LAI ($m^2 m^{-2}$) with pH and by year.

Maximum LAI also does not change much with pH, with exception of year 4 (Fig. 5.26). The median varies between 4.5 and 4.8 $m^2 m^{-2}$.

5.4 Impact of SOC variations on AGB and LAI

To study the impact of SOC variations, we launched 20 simulations by varying SOC from 90% decrease to 200% increase, by 10% steps. Each of this change implied a re-estimation of:

- Saturated soil water content
- Saturated hydraulic conductivity
- Field capacity
- Wilting point

5.4.1 Growth start date

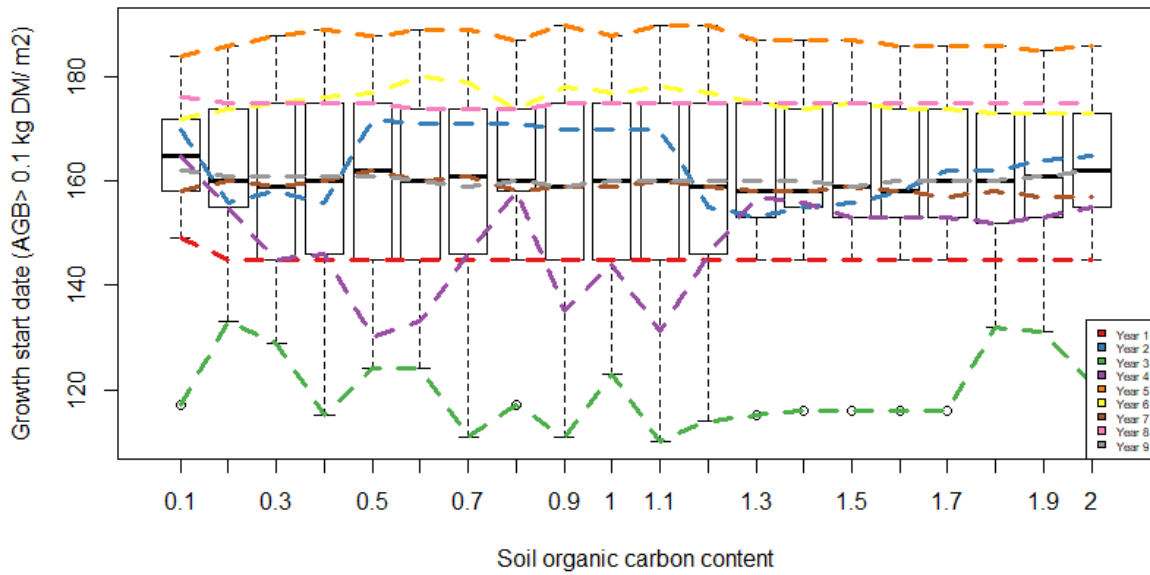


Fig. 5.27. Variation of growth start date with SOC and by year.

From Fig. 5.27, we conclude that SOC variations do not result into a significant shift in the growth start date. The median is between 160 and 165 days. Higher fluctuations are visible in years 2 and 4 (between SOC values equal to 0.4 and 1.2).

5.4.2 Growth end date

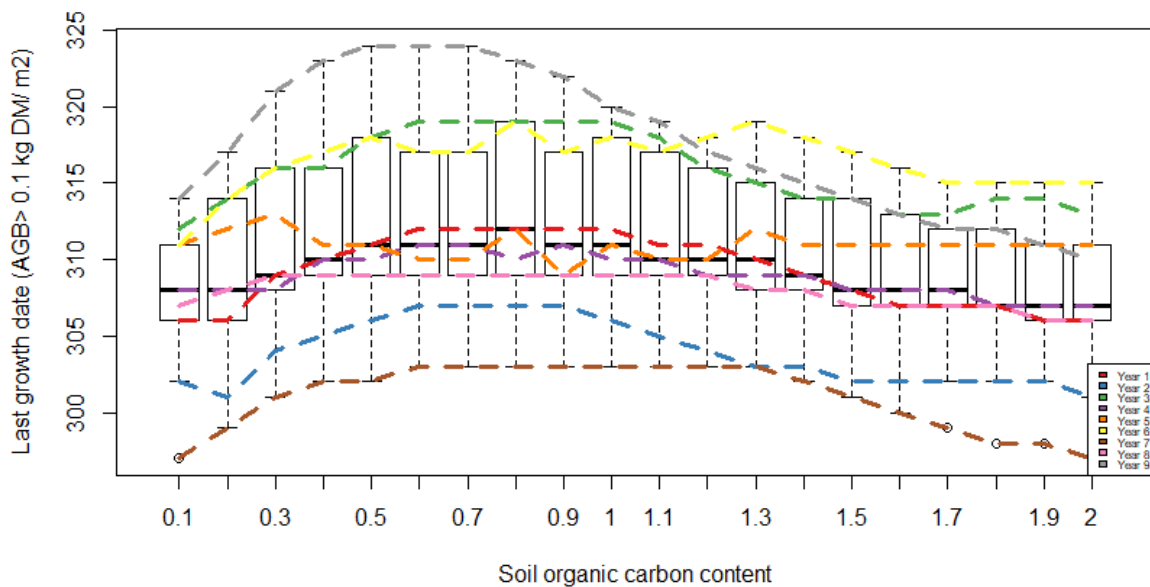


Fig. 5.28. Variation of growth end date with SOC and by year.

From Fig. 5.28, we conclude that SOC variations result into a significant shift in the last growth date for SOC values equal to 0.4 and 0.5 (median at day 324) except for the years 1 and 2.

5.4.3 Date of maximum growth

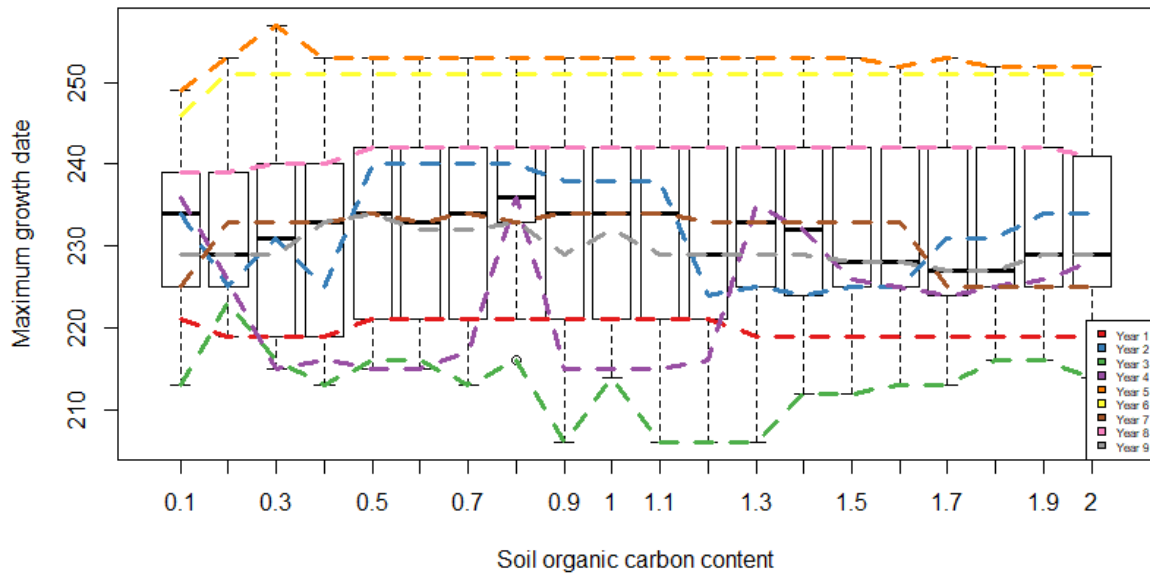


Fig. 5.29. Variation of the date of maximum growth with SOC and by year.

There is not a large shift in the dates of maximum growth, with the exception of years 2 and 4 (Fig. 5.29). Median values vary from day 225 to day 235.

5.4.4 Mean AGB

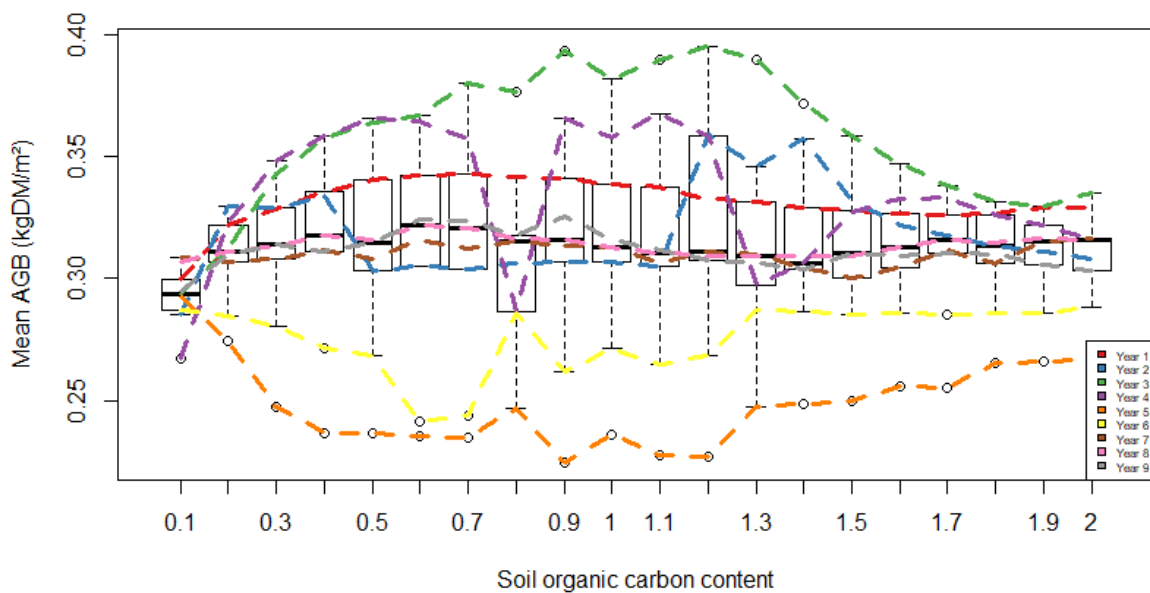


Fig. 5.30. Variation of mean AGB (kg DM m^{-2}) with SOC and by year.

Fig. 5.30 shows that it is difficult to find an explanatory scheme of the important intra-annual variability observed in the mean AGB (median ~ 0.30).

5.4.5 Maximum AGB

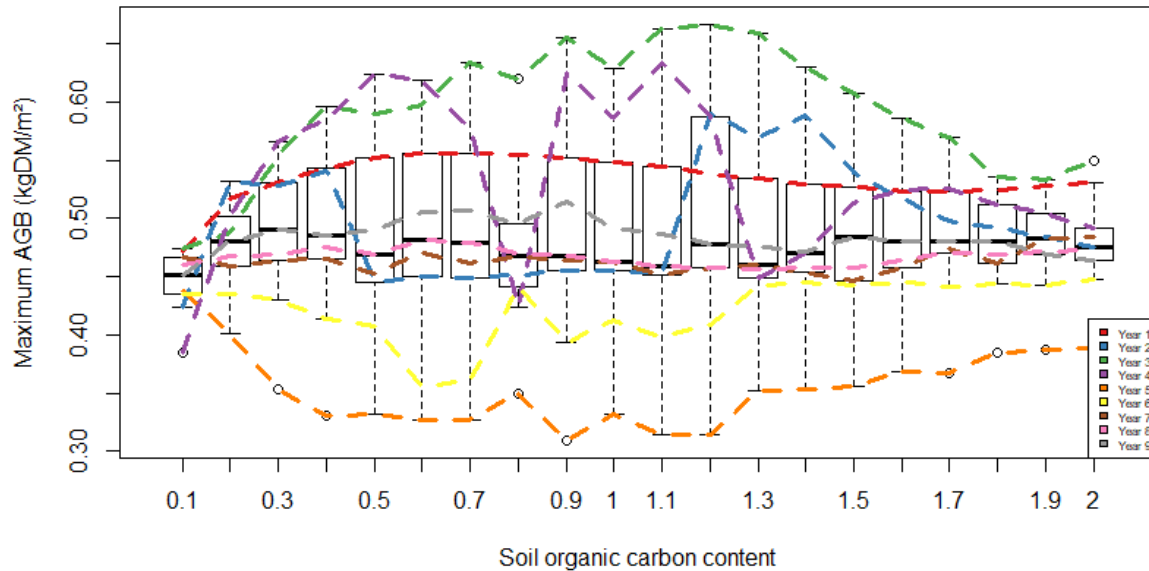


Fig. 5.31. Variation of maximum AGB (kg DM m^{-2}) with SOC and by year.

As with mean AGB, there is no explanatory pattern emerging from Fig. 5.31. The interannual variability of maximum AGB is important especially for years 2, 3 and 4.

5.4.6 Mean LAI

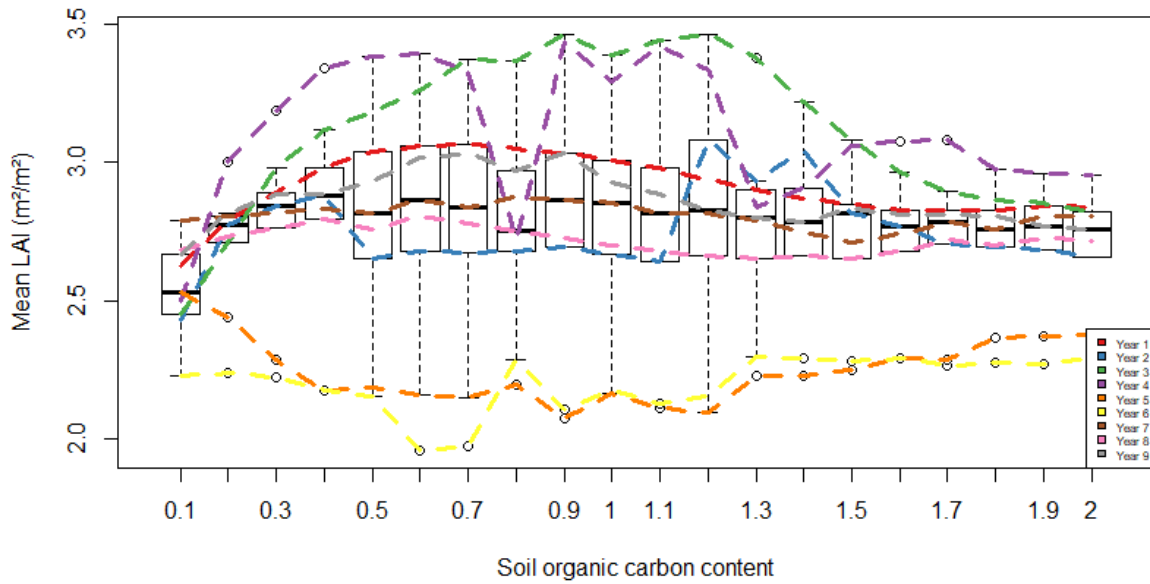


Fig. 5.32. Variation of mean LAI ($m^2 m^{-2}$) with SOC and by year.

Similar to mean AGB, we conclude that mean LAI does not result into a large shift of variation, with the exception of years 2, 3 and 4 (Fig. 5.32). Median values vary from 2.5 to 2.9 $m^2 m^{-2}$.

5.4.7 Maximum LAI

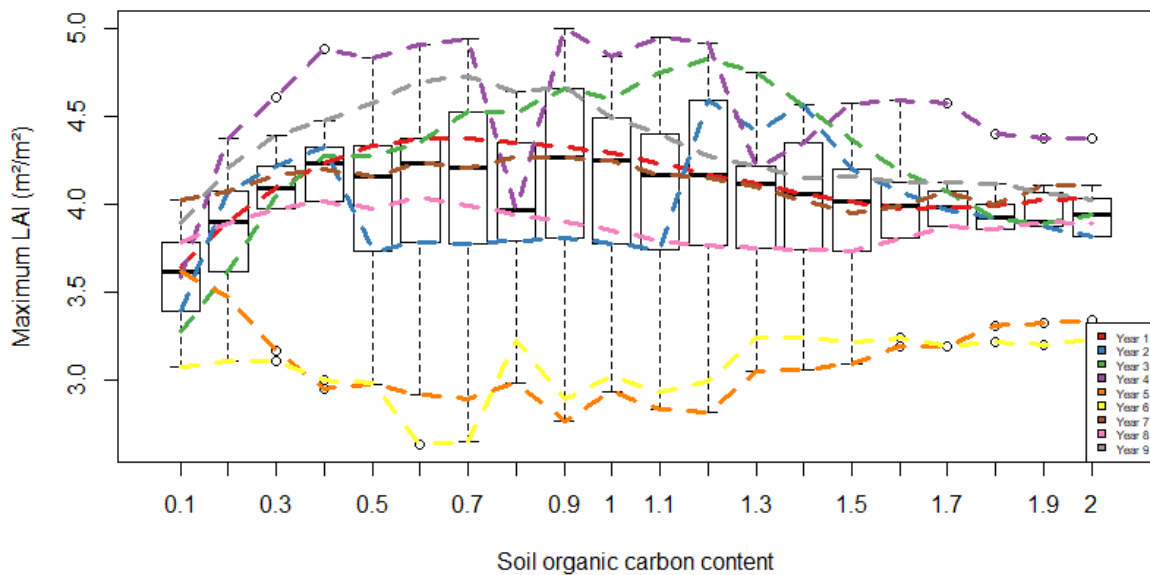


Fig. 5.33. Variation of maximum LAI ($m^2 m^{-2}$) with SOC and by year.

As for Fig. 5.32, it is difficult to find an explanatory scheme in Fig. 5.33. We note however a significant intra-annual variability for roughly every year. Median values vary between 3.6 and 4.1 $m^2 m^{-2}$.

5.5 Climate analysis

In order to understand the origin of AGB and LAI variations for particular years and to know what would be the main factor that affects these two variables, the possible effect of weather conditions was explored.

Temperature (°C) and rainfall (mm d⁻¹)

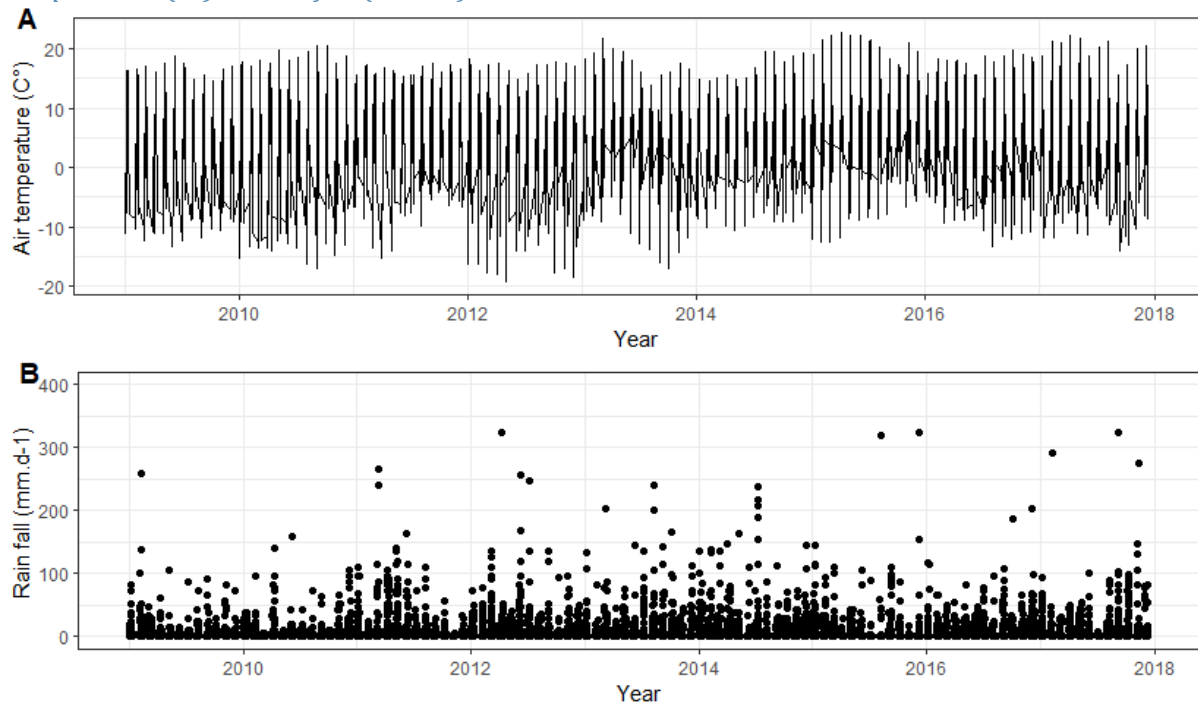


Fig. 5.34. Time series of (A) air temperature (°C) and (B) rainfall (mm d⁻¹) at Torgnon.

Temperatures are relatively low at Torgnon, as in Fig. 5.34 (A). The lowest temperatures were recorded in 2012 (year 4), which partly explains the variations in AGB and LAI for with variations of pH and SOC.

Soil water content

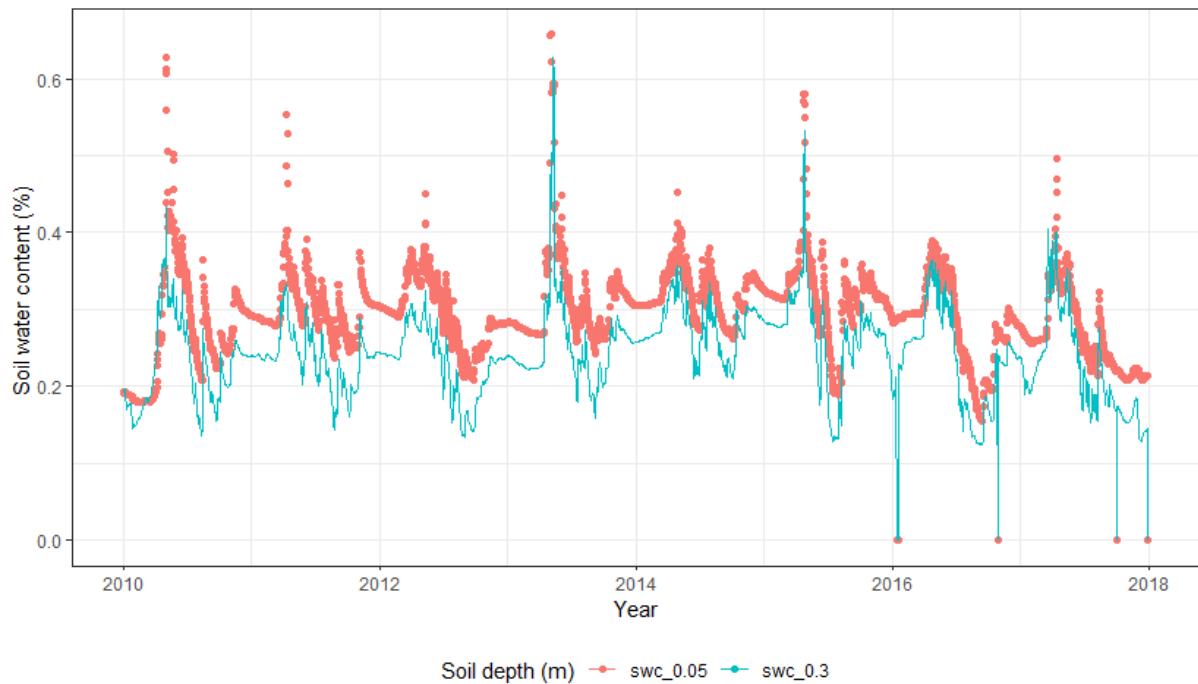


Fig. 5.35. Soil water content (%) observed at Torgnon.

Soil water content was observed to decrease with depth (Fig. 5.35). In the deepest layer (0.3 m), we observe a decrease of soil water content in 2011 and 2012 (years 3 and 4). Even if as of 2016 (year 8) low peaks occasionally approach zero, the robust decrease of soil water content in 2012 can explain the variations of AGB and LAI observed in year 4 by varying the pH.

Aridity index

An aridity index (b) from De Martonne-Gottmann (De Martonne, 1942), which has already been used in recent studies to characterize climatic conditions in grassland systems (Sándor et al., 2017, 2018). It offers the possibility of distinguishing different site-specific thermo-pluviometric conditions, according to the ranges of values published by Diodato and Ceccarelli (2004): $b < 5$: extreme aridity; $5 \leq b < 14$: aridity; $15 \leq b < 19$: semi-aridity; $20 \leq b < 29$: sub-humidity; $30 \leq b < 59$: humidity; $b \geq 59$: high humidity:

$$b = \frac{1}{2} \cdot \left(\frac{P_y}{T_y + 10} + 12 \cdot \frac{P_a}{T_a + 10} \right)$$

where P_y (mm): total annual precipitation; T_y (°C): average annual temperature; p_a (mm): total precipitation for the driest month; T_a (mm): mean monthly temperature of the driest month.

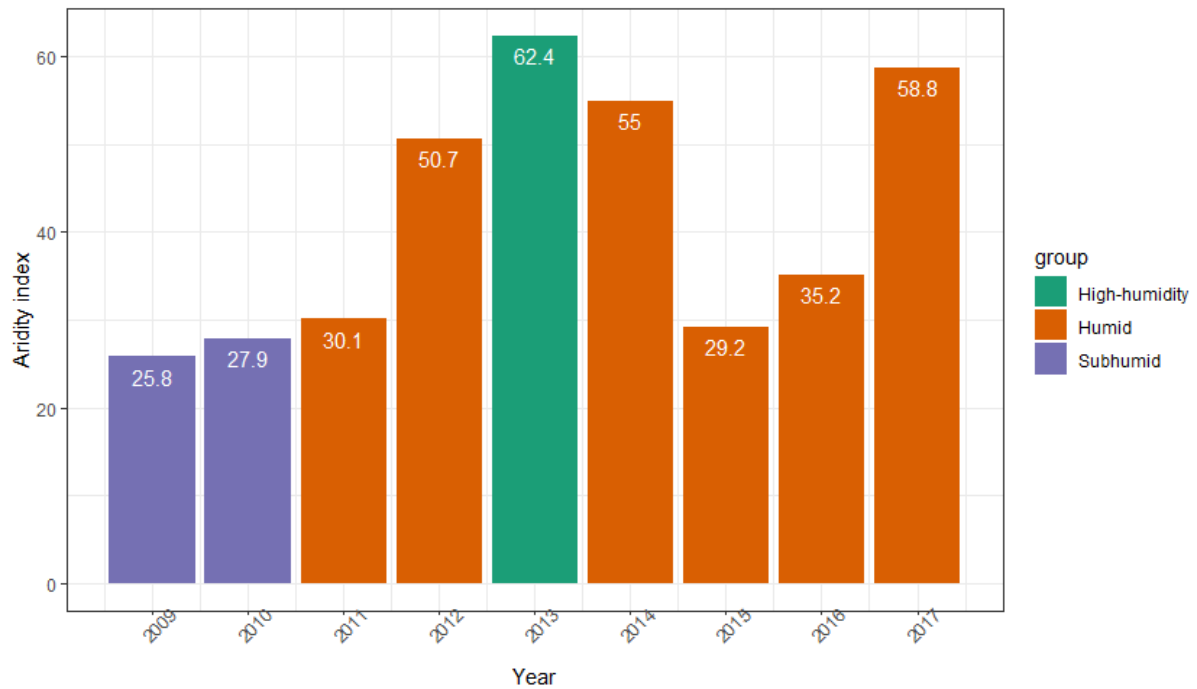


Fig. 5.36. De Martonne-Gottmann aridity index.

The climate of Torgnon is essentially humid (Fig. 5.36). The maximum value of the aridity index, 62.4, was observed in 2013, when there was the highest precipitation. Exceptionally, a sub-humid character, with little precipitation and an aridity index equal to 25.8 and 27.9 respectively, marked the years 2009 and 2010. To go further, we sought to know the thermo-pluviometric conditions of each month for the year 2011 and 2012 since it is on the year 2012 (year 4) that we observe significant variations of AGB and LAI.

Another aridity index that the United Nations Environment Program (UNEP, 1993) has adopted is defined as follows:

$$AI_U = \frac{P}{PET}$$

where PET is the potential (reference) evapotranspiration (extracted from the PaSim outputs) and P is the average annual precipitation. In this case, the ranges of values are as follows: $AI_U < 0.05$: hyper-arid; $0.05 < AI_U < 0.20$: arid; $0.20 < AI_U < 0.50$: semi-arid; $0.50 < AI_U < 0.65$: sub-humid; $AI_U > 0.65$: humid.

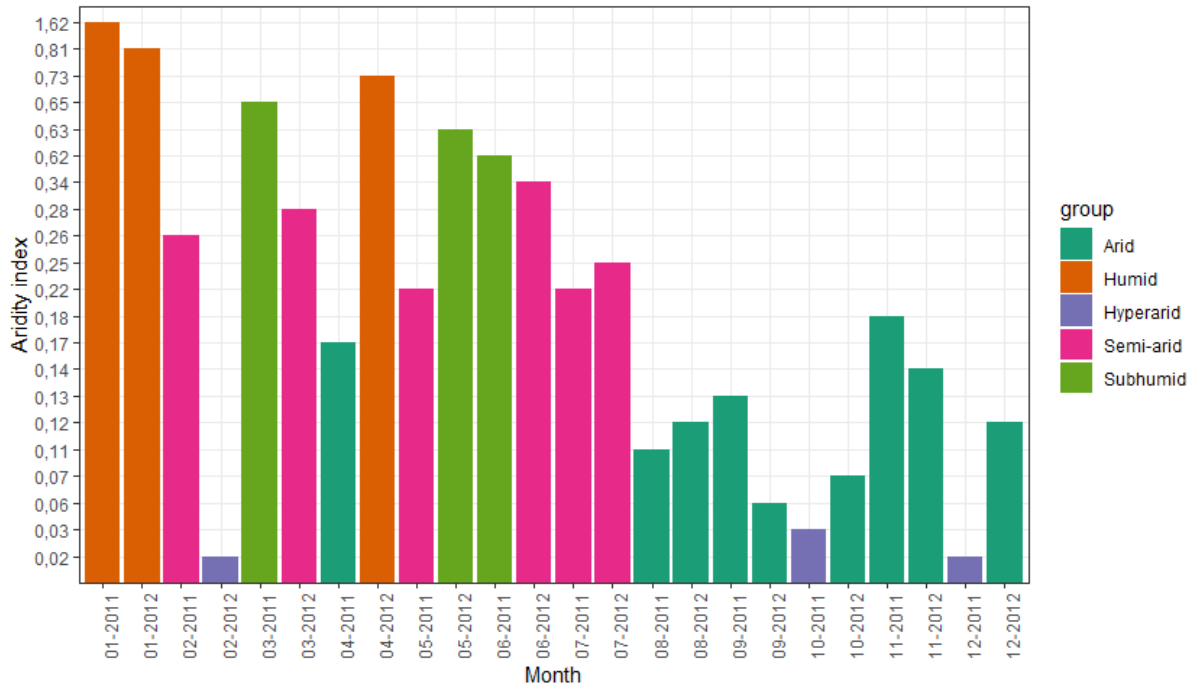


Fig. 5.37. UNEP aridity index.

Although 2012 had been a humid year, month-to-month variability is high (Fig. 5.37). At the beginning of the growing season, conditions were mostly semi-arid, varying from sub-humid to semi-arid and arid during the growing season. Humid conditions occurred in January and April.

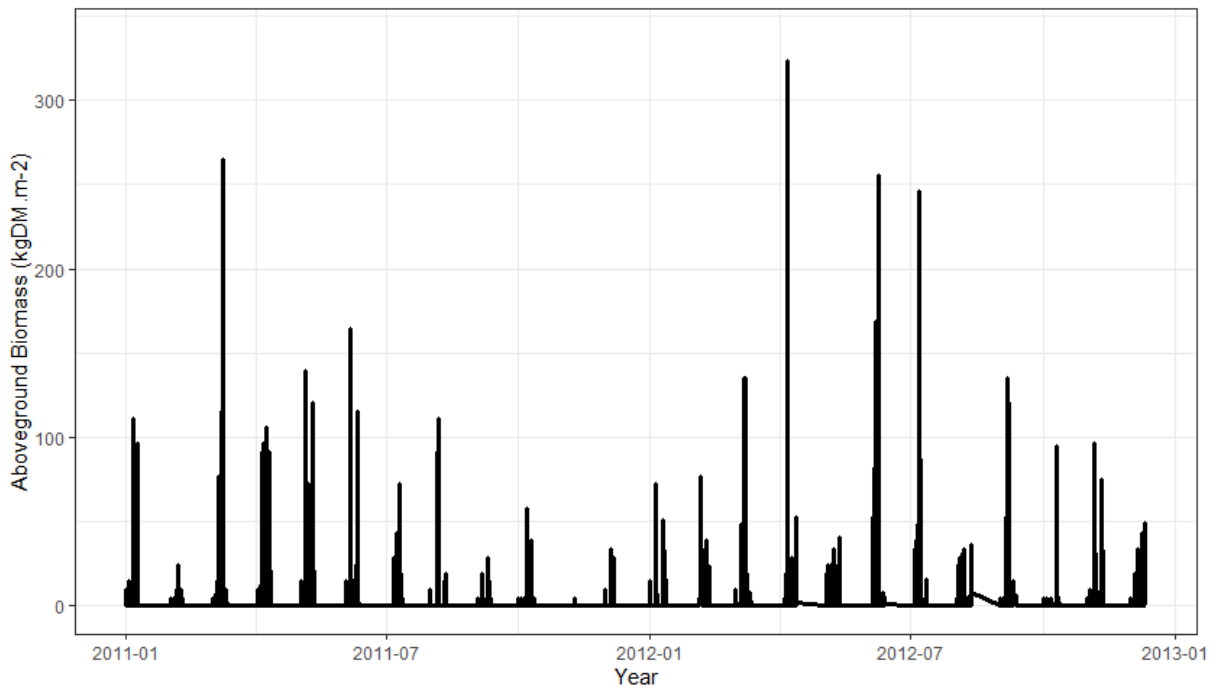


Fig. 5.38. Simulated aboveground biomass ($kg DM m^{-2}$).

The droughts recorded in 2011 and 2012 could have affected the structure of the community, which translated into variations in the rate of forage production for the two years (simulated AGB in Fig. 5.38).

To conclude, this analysis revealed that the large variations in pH values and SOC content induce only minimal variations in AGB ($0.02 \text{ kg DM m}^{-2}$) and LAI ($0.1\text{-}0.3 \text{ m}^2 \text{ m}^{-2}$). On average, AGB and LAI appear insensitive to variations in pH and SOC, which do not cause significant changes in these outputs. Lack of soil water, as revealed by aridity indices, may affect AGB and LAI, which can explain the variability observed in some years with these two outputs under varying pH.

6 Random Forest set up and assessment

In order to assess the impacts of projected climate on the distribution of pasturelands across the two study areas (namely, Parco Nazionale Gran Paradiso - PNGP and Parc des Ecrins - PNE), the Random Forest machine-learning approach (RF; Breiman, 2001) was first trained for the near-past period 1990-2010. Then, it was applied to simulate changes of future pasture occurrence over RCP 4.5 and 8.5 scenarios (as predicted by CNRM-ALADIN, ICTP-RGCM4, and CMCC-CCLM4, Regional Circulation Models - RCMs) for two future time slices (2011-2040 and 2041-2070) compared to the near past (1990-2010). To that, current pasturelands' distribution was assumed in equilibrium with the present environmental conditions.

6.1 Methodology

6.1.1 The Random Forest (RF) machine-learning statistical model

RF, a machine-learning algorithm based on decision-tree classifiers, consists of a combination of decision trees where each classifier is generated using a bootstrap sample randomly split into two subsets, one for training (66%) and one for internal testing (33%). RF prediction is made giving a majority vote for model classification of an ensemble of classification trees, and the final model prediction is generated by taking the most voted model prediction from all the tree predictors in the forest. Observations of the original dataset that do not occur in a bootstrap sample are called Out-Of-Bag (OOB). The OOB-error estimate is calculated for each tree over the data split out of the corresponding bootstrap sample and then averaged over all observations. Hence, OOB is not used in the fitting of the trees and essentially constitutes a cross-validated accuracy estimates. To avoid over-fitting at each bootstrap sample, the number of variables randomly used at each random split can be fixed setting the "mtry" parameter. Each classification tree is fully grown until a final node is reached and then it is used to predict the classes of OOB observations. Moreover, setting the desired number of trees ("ntree" parameter), this procedure can be repeated until the value of this parameter is reached. Along the calibration phase, RF provides measures of variable importance, which is based on the computation of the mean decrease of classification accuracy as well as the dependence of the probability of presence on one predictor variable (partial dependence plots), after averaging out the effects of the other predictor variables in the model.

RF requests an input predictor/response tables, the environmental variables included in the topographic-soil-climate dataset represented the predictors, the presence/absence of pasturelands were the binary response variable (1/0, respectively). RF (as implemented in R environment (package "randomForest") was first trained to simulate pasturelands and pasture macro-types distribution against current climate (baseline 1990-2010) and then applied over the future climate dataset as downscaled and elaborated in Action C.1 (see Deliverable C.1 - Report on future climate scenarios for the two study areas).

6.1.2 Ancillary data for RF training

Predictive variables (soil, topography and climatic data) were extracted from the Harmonized World Soil Database (Nachtergaele et al., 2008) and WorldClim (Hijmans et al., 2005), and used as input variable to feed RF. The predictors extracted are: soil pH (pH), elevation, slope, mean maximum temperature of the warmest month (July) (TMAX_Jul), the mean minimum temperature of the coldest month (January) (TMIN_Jan), seasonal precipitation (Prec_DJF, Prec_MAM, Prec_JJA, Prec_SON) - respectively referred to Winter, Spring, Summer and Autumn seasons. The datasets shared the same spatial resolution, namely $1 \times 1 \text{ km}$.

The current extent of mountain pasturelands (i.e. RF response variables) was retrieved from CORINE land cover map (namely codes 321, 322 and 324) integrated with maps produced in

Action C.2 (Pastures typologies survey and mapping) for PNGP study area. For PNE study area, the current pastureland distribution was retrieved from the French land cover map (Inglada et al., 2017). Both maps were converted into a grid dataset, spatially consistent with the predictor variables dataset (1 x 1 km spatial resolution, EPSG: 4326). Since the response variable of RF is binary, i.e. presence (1) and absence (0), pixels referring to the “absence” response variables were extracted from the aforementioned maps (Corine land Cover and the French land cover map). This was done by spatially selecting the codes which corresponded to areas potentially to be niche of pasturelands (e.g. agricultural and forested areas, bare soils) but that are not currently due to human activity. Both maps were then harmonized with the predictive dataset onto a unique comprehensive 1 x 1 km spatial grid comprising 261,000 ha of pasturelands in total (200,600 and 60,400 ha in PNGP and PNE, respectively).

6.1.3 RF calibration and validation

For RF training, 10 sub-sampling datasets were randomly down-sampled from the whole dataset to have a proportion of the majority class (presence of pastures) consistent (i.e. with the same number of occurrences) with the minority-class (i.e. other land uses). The random sub-samples of RF models were then comprehensively combined into a final model, and thus applied over the whole dataset against the abiotic independent variables of current climate. In all runs, RF “mtry” parameter was set to 3 (value depending on the number of input predictive variables), while the number of trees (“ntree” parameter) was set to 100 (Oshiro et al., 2012) for all runs. The accuracy of simulations was assessed against an independent sub-sampled dataset (validation dataset), not used in the calibration runs, by computing the OOB-error calculation (confusion matrix). The relative importance of each independent variable and the partial dependence plot of probability of pastures were also calculated, which give the importance of predictors and the graphical depiction of the marginal effect of predictors on the RF class classification, respectively. Accordingly, the RF models was applied over the entire dataset to predict site-level probability of occurrence of pastures across the study areas in the current (near-past) time period and under RCP 4.5 and 8.5 future climate scenarios in the near (2011-2040) and far (2041-2070) future, as projected by CNRM-ALADIN, ICTP-RGCM4, and CMCC-CCLM4 RCM models.

6.2 Results

6.2.1 RF calibration outputs and accuracy

RF classification accuracy was estimated by comparing simulated presence/absence of pastures against 2610 grid points of the validation dataset along the climatic baseline period (1970-2000). RF calibration showed to be robust, with a whole mean accuracy of 94.5%.

The relative importance of each predicting variable in the classification process was determined via the permutation of each single variable in the calibration process and testing the relevant accuracy of the results (Mean Decrease Accuracy, MDA). The more important a variable is in the accuracy of the prediction, the higher the relevant MDA is (Fig. 6.1). The results (Figs. 6.2 and 6.3) indicate that the most important variables were slope followed by the maximum air temperature of July (Tmax_jul) and spring precipitation (Prec_mam). Tmin_jan yielded the lowest importance as drivers of the presence of pastures across both PNGP and PNE study areas.

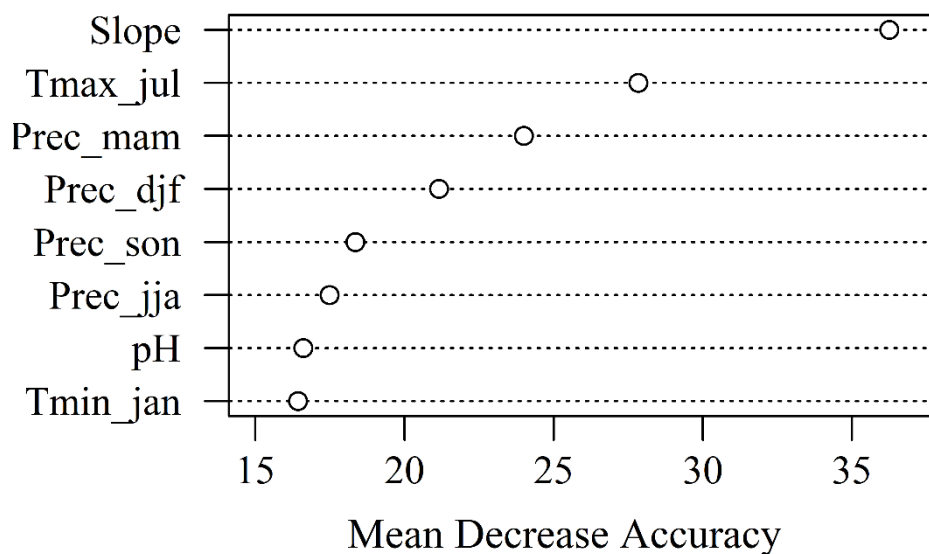


Fig. 6.1 displays the partial plots of predictors, i.e. the graphical depiction of the marginal effect of predictors on the RF class classification for both PNGP and PNE areas.

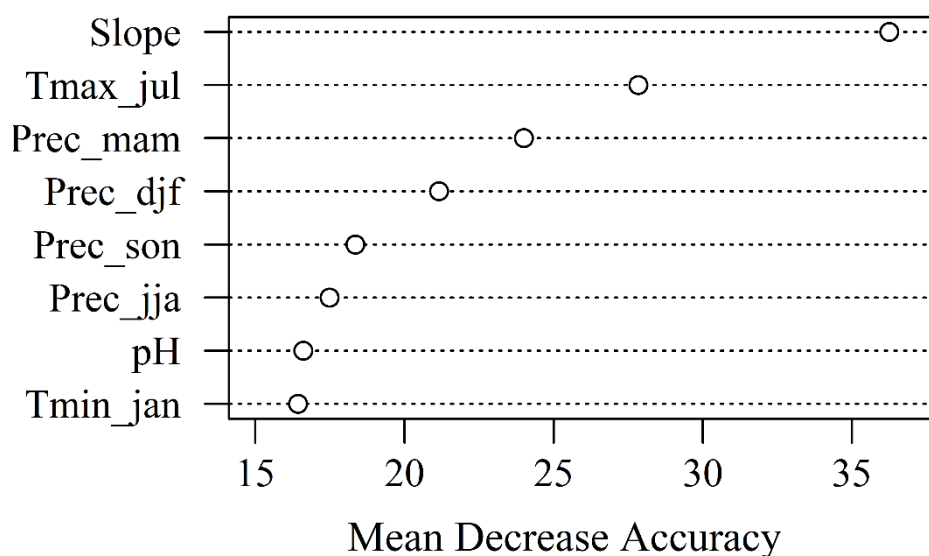


Fig. 6.2. Relative importance of climatic variables, expressed as mean decrease accuracy, in the classification process as derived from random forest calibration. Variables are pH; slope; Tmax_jul: monthly average maximum temperature of July; Tmin_jan: monthly average minimum temperature of January; Prec_djf, Prec_mam, Prec_jja, and Prec_son cumulated precipitation of winter, spring, summer and autumn season, respectively.

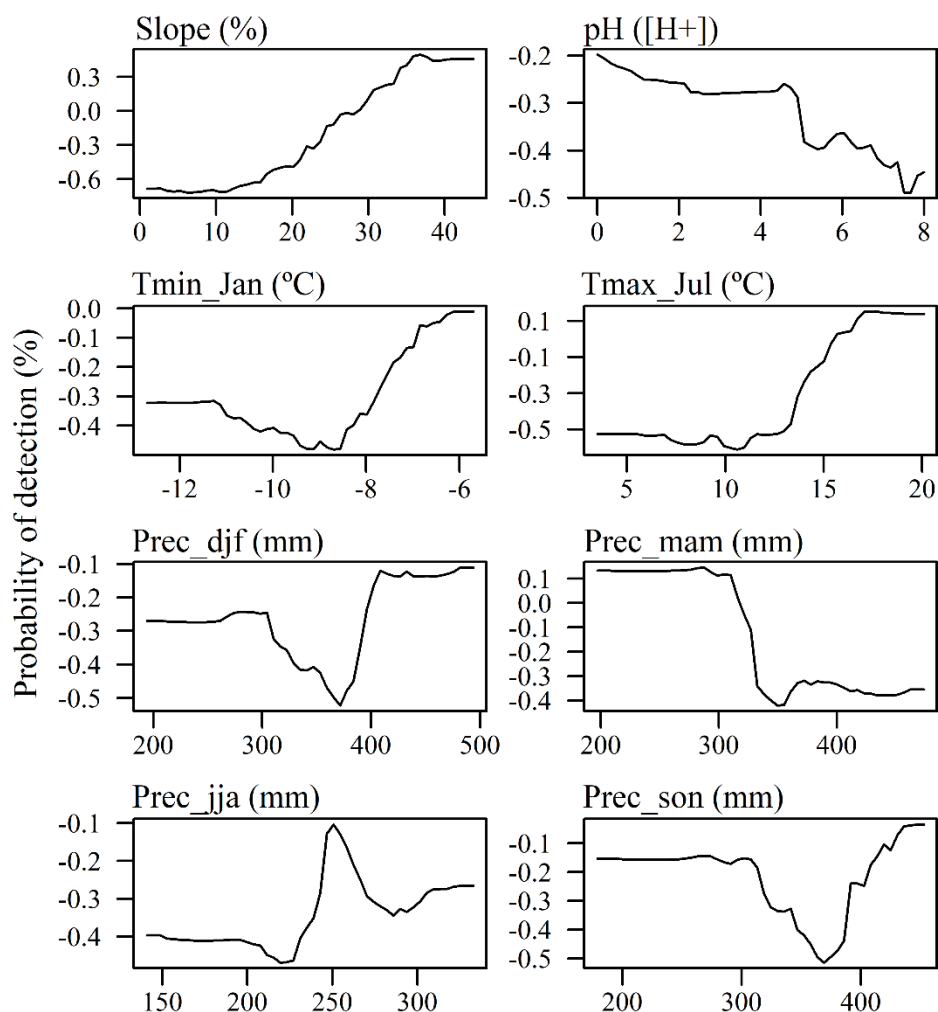


Fig. 6.3. Partial Dependence Plot of the probability of presence of pastures across PNGP and PNE versus increasing values of Slope, pH, Tmin_Jan, Tmax_Jul, Prec_djf, Prec_mam, Prec_jja, Prec_son. The original data were interpolated using a polynomial function.

6.2.2 Future pasture distribution

RF simulations against future climate indicated a global slight reduction of pastures suitability for all time-slices and scenarios, particularly for 2041-2070 where pasturelands decreased in a range of -8% to -5% with respect to present period under RCP 4.5 and 8.5, respectively (Table 6.1a). The main losses are expected at Gran Paradiso National Park in RCP 4.5 in the far future (Table 6.1b). Parc des Ecrins is expected to be affected by lower losses in pastoral suitability (-2%) with respect to the present under both RCP scenarios.

Table 6.1 displays results from RF simulations under RCP 4.5 and 8.5 scenarios (as predicted by CNRM-ALADIN, ICTP-RGCM4, and CMCC-CCLM4, Regional Circulation Models - RCMs) and two future time slices (2011-2040 and 2041-2070) compared to the baseline (1990-2010) for both areas (a), and distinctly for PNGP (b) and PNE (c). The results are also spatially displayed in Figs. 6.4 and 6.5 (for PNGP and PNE, respectively), depicting gains and losses of pastoral suitability as simulated by RF using the three RCMs, as simulated by RF under near and far future according to RCP 4.5 and 8.5 scenarios.

Table 6.1. Current occurrence (in terms of number of pixels, i.e. 100 ha wide each) of pasturelands and expected changes (%) of suitability under future climate conditions, as reported by the three Regional Circulation Models (RCMs) and their ensemble, time slices (2011-2070 and 2071-2100) and RCP scenarios (4.5 and 8.5).

ENSEMBLE OF PNE AND PNGP (a)									
		Number of pixels				%			
RCM	Present	RCP 4.5		RCP 8.5		RCP 4.5		RCP 8.5	
---	---	2011- 2040	2041- 2070	2011- 2040	2041- 2070	2011- 2040	2041- 2070	2011- 2040	2041- 2070
Aladin	2610	2653	2339	2377	2521	2%	-10%	-9%	-3%
CMCC	2610	2231	2384	2562	2270	-15%	-9%	-2%	-13%
ICTP	2610	2740	2503	2741	2684	5%	-4%	5%	3%
Ensemble	2610	2541	2409	2560	2492	-3%	-8%	-2%	-5%

GRAN PARADISO NATIONAL PARK (PNGP) (b)									
		Number of pixels				%			
RCM	Present	RCP 4.5		RCP 8.5		RCP 4.5		RCP 8.5	
---	---	2011- 2040	2041- 2070	2011- 2040	2041- 2070	2011- 2040	2041- 2070	2011- 2040	2041- 2070
Aladin	2006	2010	1702	1745	1880	0%	-15%	-13%	-6%
CMCC	2006	1709	1807	1980	1693	-15%	-10%	-1%	-16%
ICTP	2006	2126	1935	2116	2057	6%	-4%	5%	3%
Ensemble	2006	1948	1815	1947	1877	-3%	-10%	-3%	-6%

PARC DES ECRINS (PNE) (c)									
		Number of pixels				%			

RCM	Present	RCP 4.5		RCP 8.5		RCP 4.5		RCP 8.5	
		2011-2040	2041-2070	2011-2040	2041-2070	2011-2040	2041-2070	2011-2040	2041-2070
---	---								
Aladin	604	643	637	632	641	6%	5%	5%	6%
CMCC	604	522	577	582	577	-14%	-4%	-4%	-4%
ICTP	604	614	568	625	627	2%	-6%	3%	4%
Ensemble	20874	593	594	613	615	-2%	-2%	1%	2%

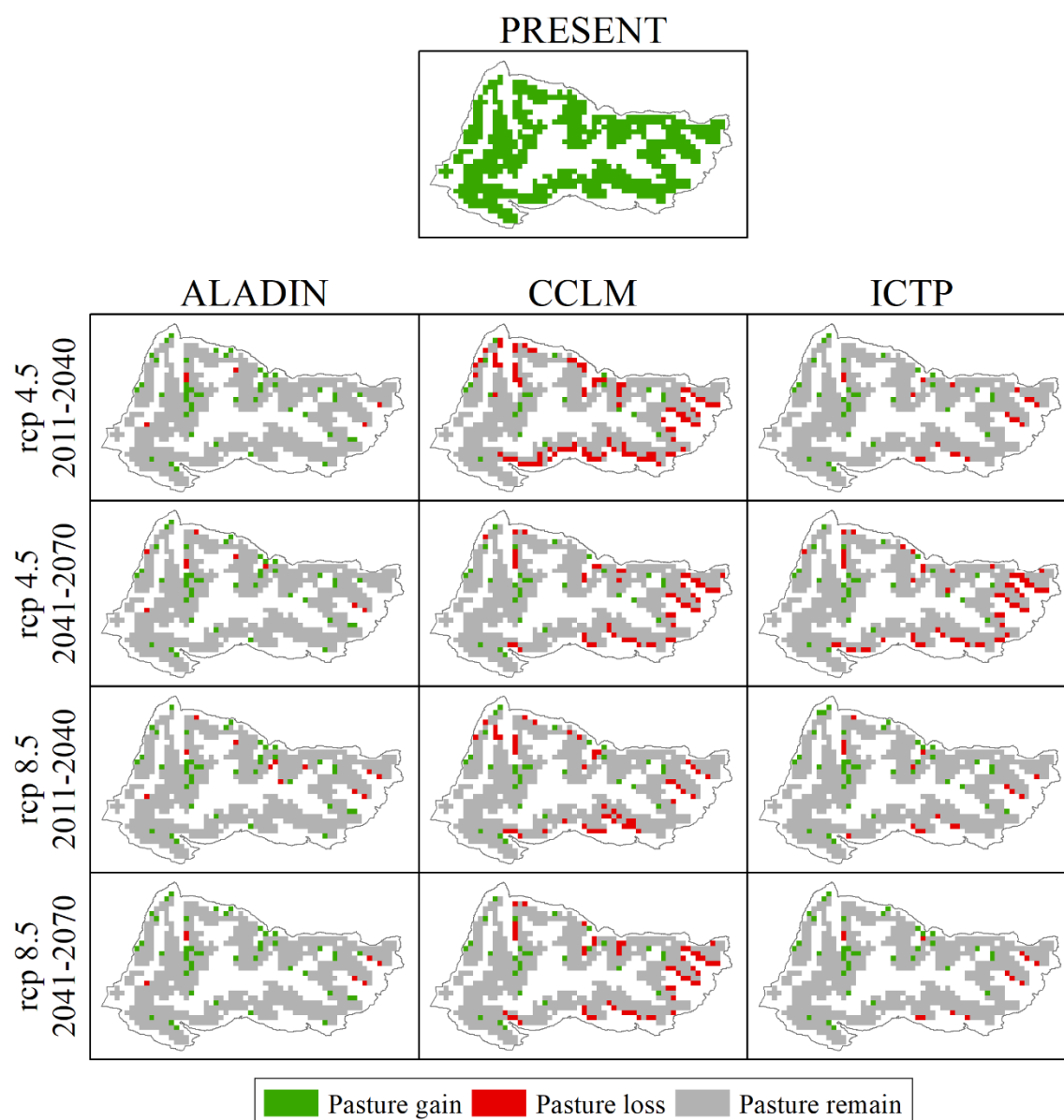


Fig. 6.4. Grid cell map representing the distribution of pastures across PNGP in the present (top of the figure) and variations (in red losses, in green gains and in grey no change) in the near (2011-2040) and far future (2041-2070) under RCP 4.5 and 8.5 RCP scenarios according to the three RCMs with respect to the present, as simulated by RF.

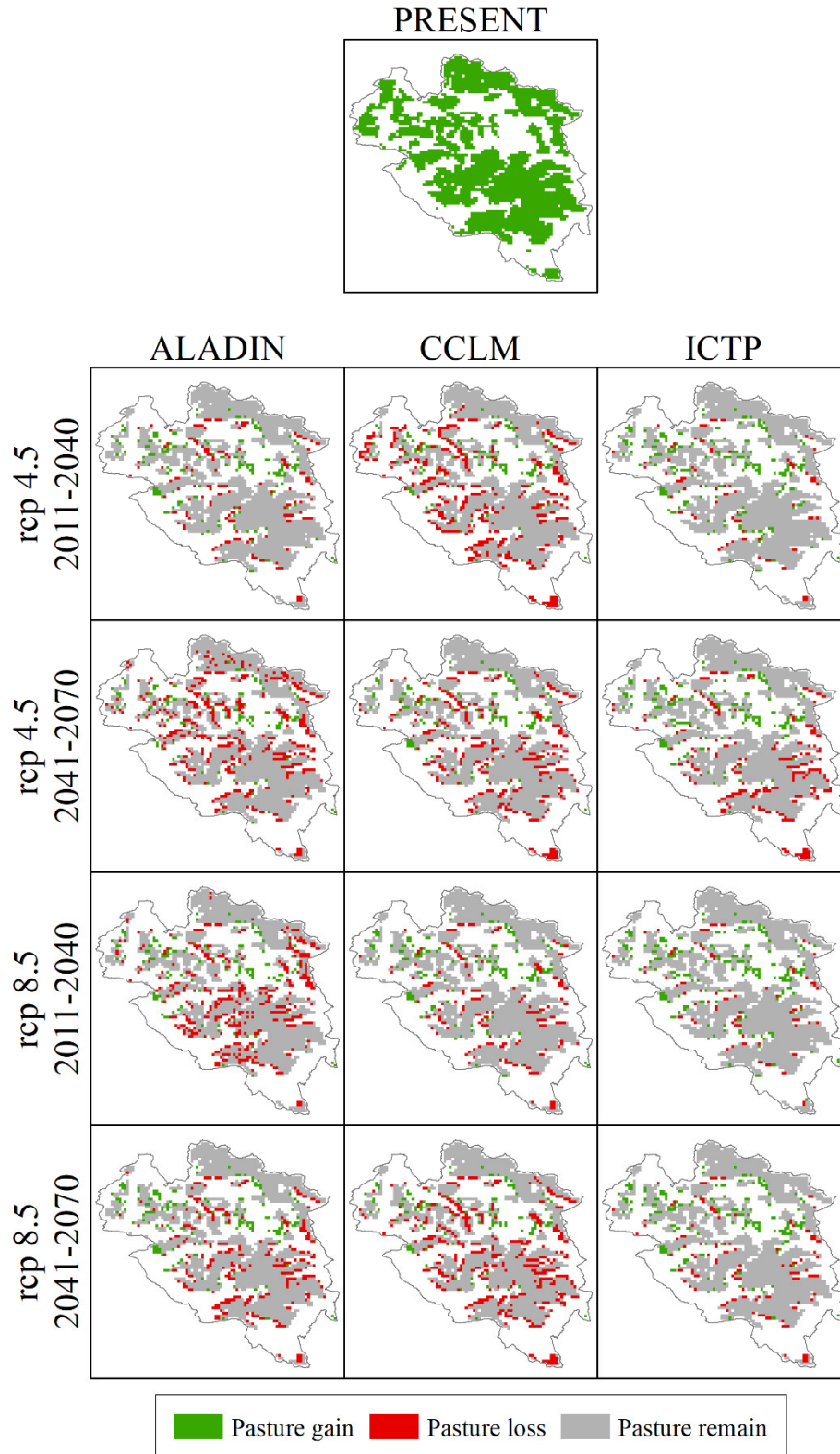


Fig. 6.5. Grid cell map representing the distribution of pastures across PNE study area in the present (top of the figure) and variations (in red losses, in green gains and in grey no change) in the near (2011-2040) and far future (2041-2070) under RCP 4.5 and 8.5 RCP scenarios according to the three RCMs with respect to the present, as simulated by RF.

7 Simulations under future scenarios (DayCent, PNGP) – based on site-specific calibration

Some results of possible impacts of future climate change are anticipated, as simulated by DayCent for the PNGP.

Once calibrated and validated, DayCent was run under RCP 4.5 and 8.5 scenarios of future climate (as predicted by CNRM-ALADIN, ICTP-RGCM4, and CMCC-CCLM4, Regional Circulation Models - RCMs) and for two time slices (2011-2040 and 2041-2070), and then compared to near past (1990-2010). For understanding the possible impacts of the expected conditions under future climate change, three variables were considered, which globally might influence animal-husbandry enterprises over alpine pastures: i) height of snow cover; ii) length of growing season; iii) biomass pattern. The first variable was considered in order to take in account the possible decrease of water availability for plants and changes in the physiological activity of vegetation (i.e. early starts), which may change the pasture evolution over these areas. The length of growing season was considered based on the presence of snow cover. This variable may provide information on expected changes in farm management. The last variable was considered since it may affect the timing of farmers' cultivation practices. Results generally indicate for all sites a decrease in snow cover, an increase in the length of growing season and a slight increase in productivity by approaching warmer scenarios (Figs. 7.1, 7.2 and 7.3).

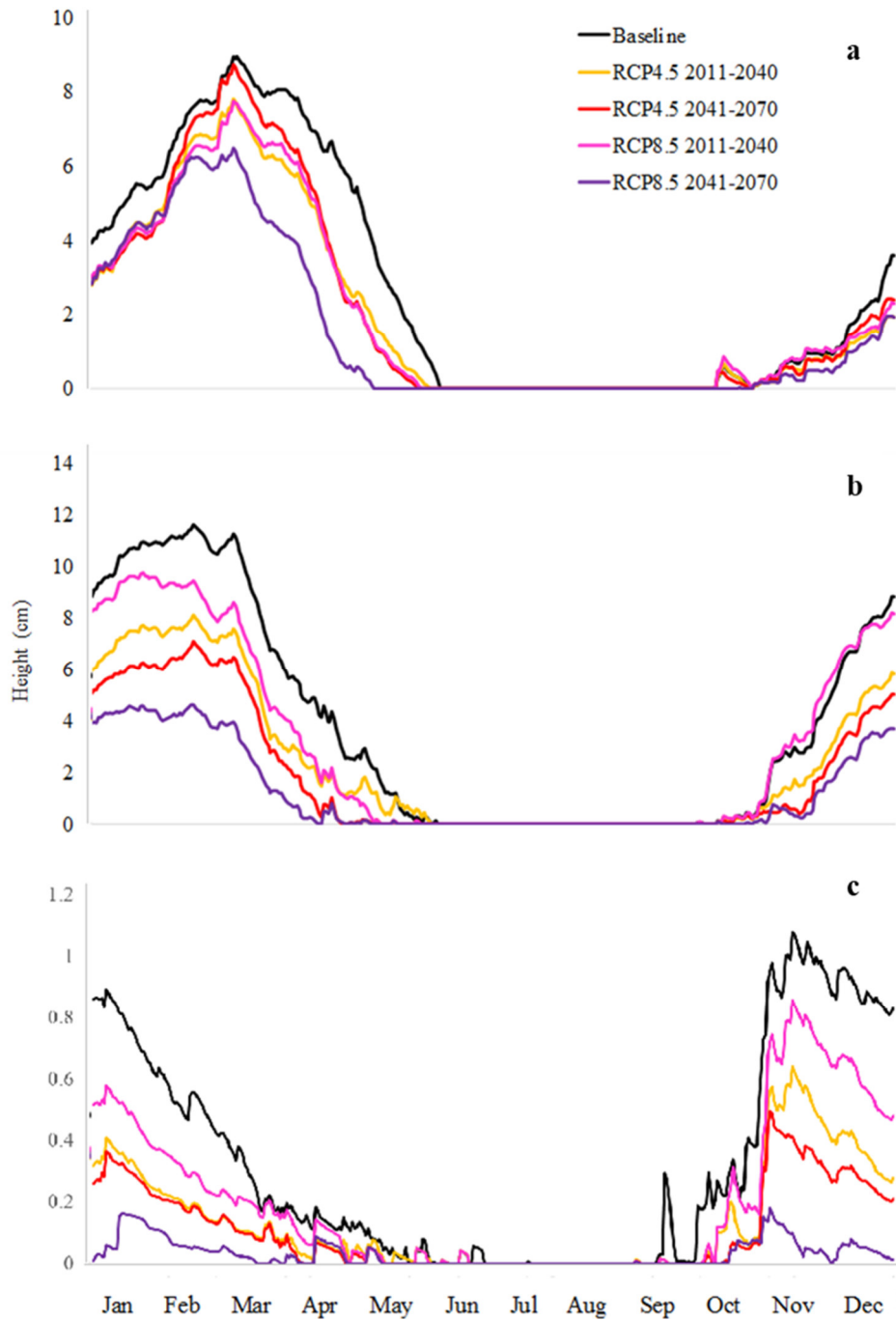


Fig. 7.1. Projected snow-cover height trend under near (2011-2040) and far (2041-2070) future, as predicted by the ensemble of RCMs (CNRM-ALADIN, ICTP-RGCM4, and CMCC-CCLM4) for RCP 4.5 and 8.5 scenarios at (a) Torgnon, (b) Entrelor (Alto) and (c) Oisans (average of sites 2, 3, 4 and 5).

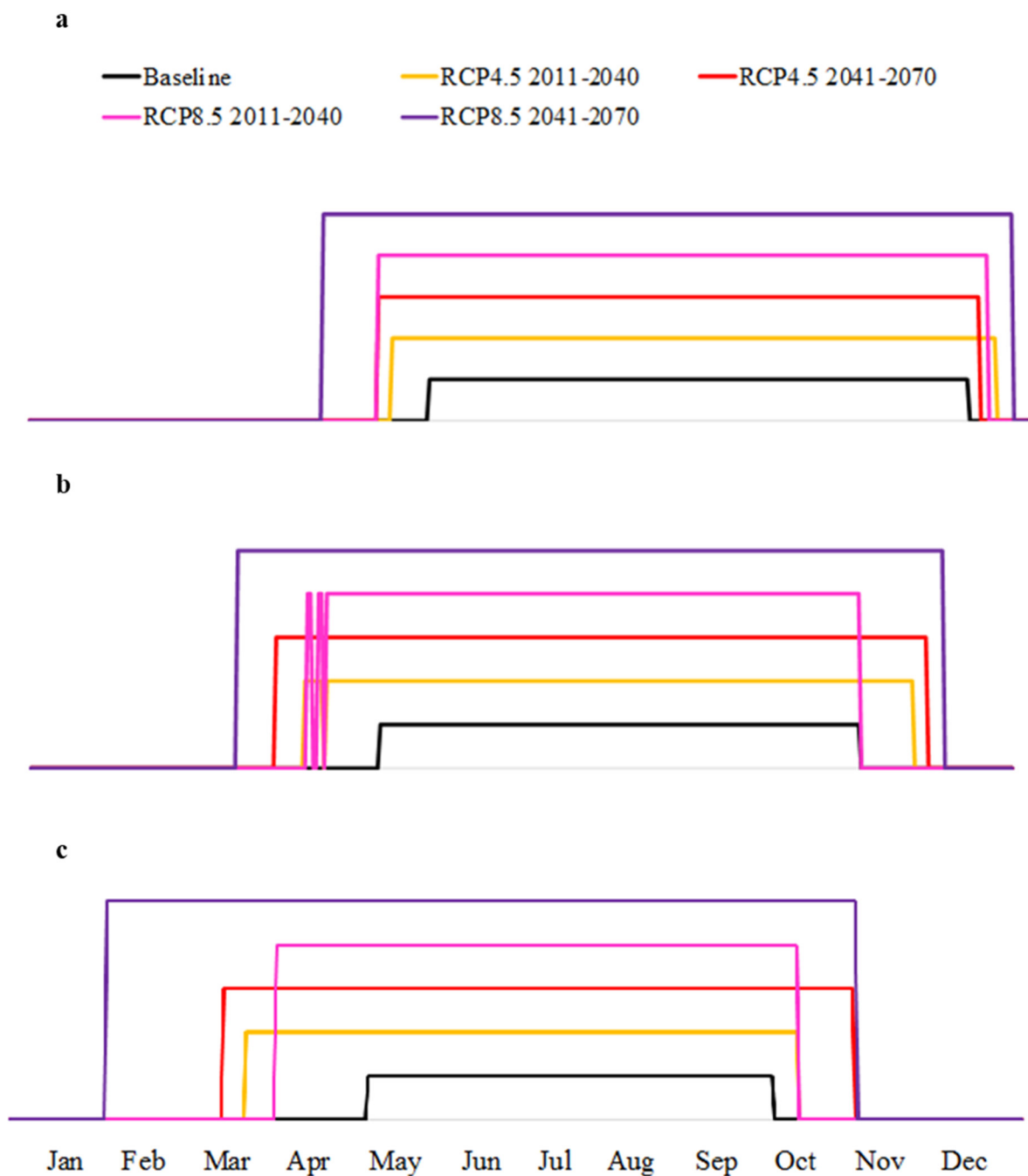


Fig. 7.2. Projected duration of vegetation period under near (2011-2040) and far (2041-2070) future, as predicted by the ensemble of RCMs (CNRM-ALADIN, ICTP-RGCM4, and CMCC-CCLM4) for RCP 4.5 and 8.5 scenarios at (a) Torgnon, (b) Entrelor (Alto) and (c) Oisans (average of sites 2, 3, 4 and 5).

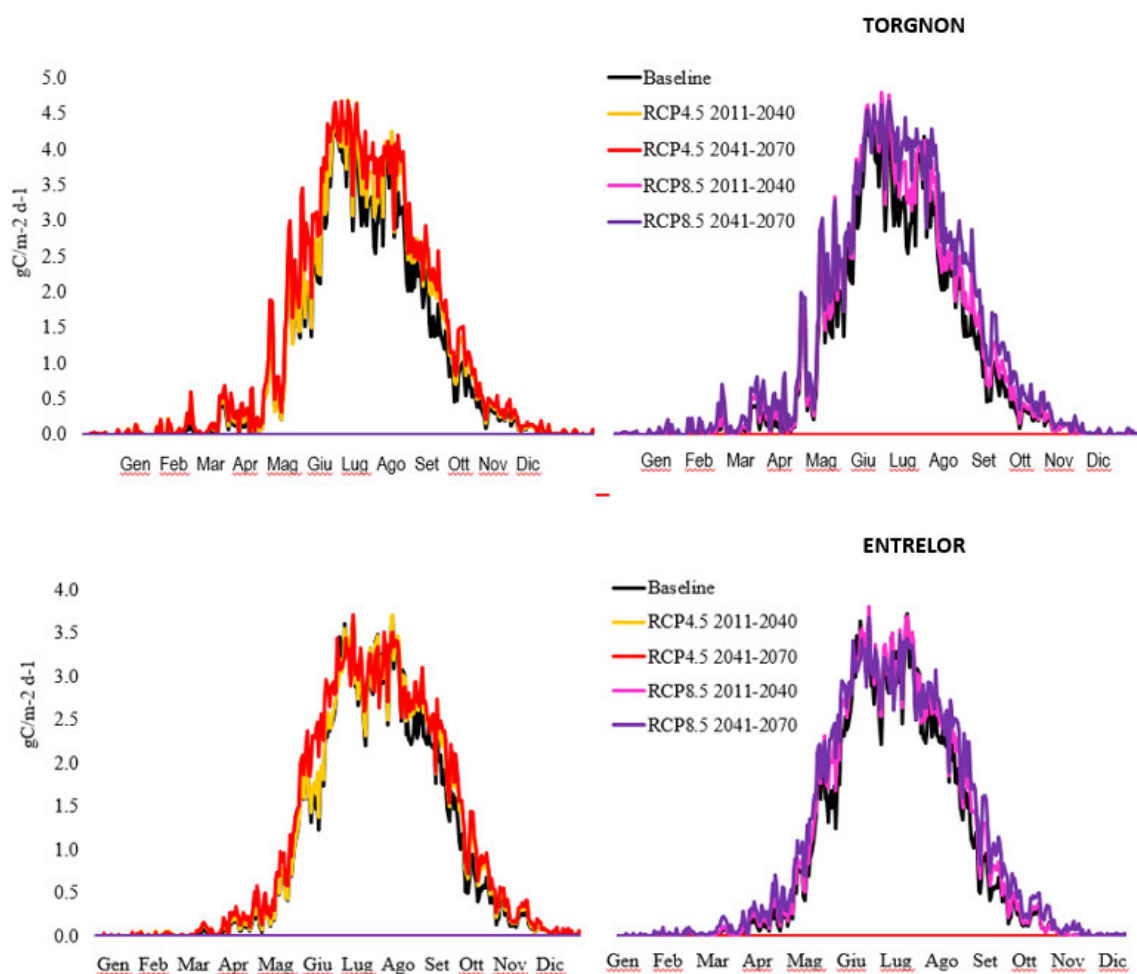


Fig. 7.3. Projected net primary production pattern ($g C m^{-2} d^{-1}$) under near (2011-2040) and far (2041-2070) future, as predicted by the ensemble of RCMs (CNRM-ALADIN, ICTP-RGCM4, and CMCC-CCLM4) for RCP 4.5 and 8.5 scenarios at Torgnon (top graph) and Entrelor Alto (bottom graph).

8 Extraction of satellite-derived vegetation spectral indices

Vegetation spectral indices were extracted from satellite imagery in order to track the seasonal development of the vegetation in the selected pastures. These data streams support model calibration/validation exercises. Study areas were selected within the mapping units defined during the activity of pasture mapping (for PNGP, action C2) or belonging to long-established, permanent study sites in the framework of Alpages Sentinelles monitoring programme (PNE). For each study areas, three grid points were selected, representing three levels of biomass productivity (Table 8.1 for PNGP).

Table 8.1. Characteristics of the study areas in the PNGP.

Label	Location: longitude, latitude (WGS84)	Elevation (m a.s.l.)	Productivity range ($kg ha^{-1}$)
Low	7.288638, 45.58242	2806	1000-3000
Medium	7.193540, 45.56793	2336	400-1000
High	7.212193, 45.58749	1627	200-400

In order to extract the best available satellite product for the description of seasonal vegetation development, we opted for the Copernicus Sentinel S2 dataset. Despite the atmospherically corrected product is available only since 2017, this satellite imagery features 5-day temporal and 20-m spatial resolutions, matching the scale of the processes we seek to investigate. Fig. 8.1 presents the 3-year time series of NDVI, as calculated from Sentinel 2 radiometrically corrected red and near infrared bands in the three grid points above described. The seasonal profiles correctly reproduce the productivity ranges detected in the field.

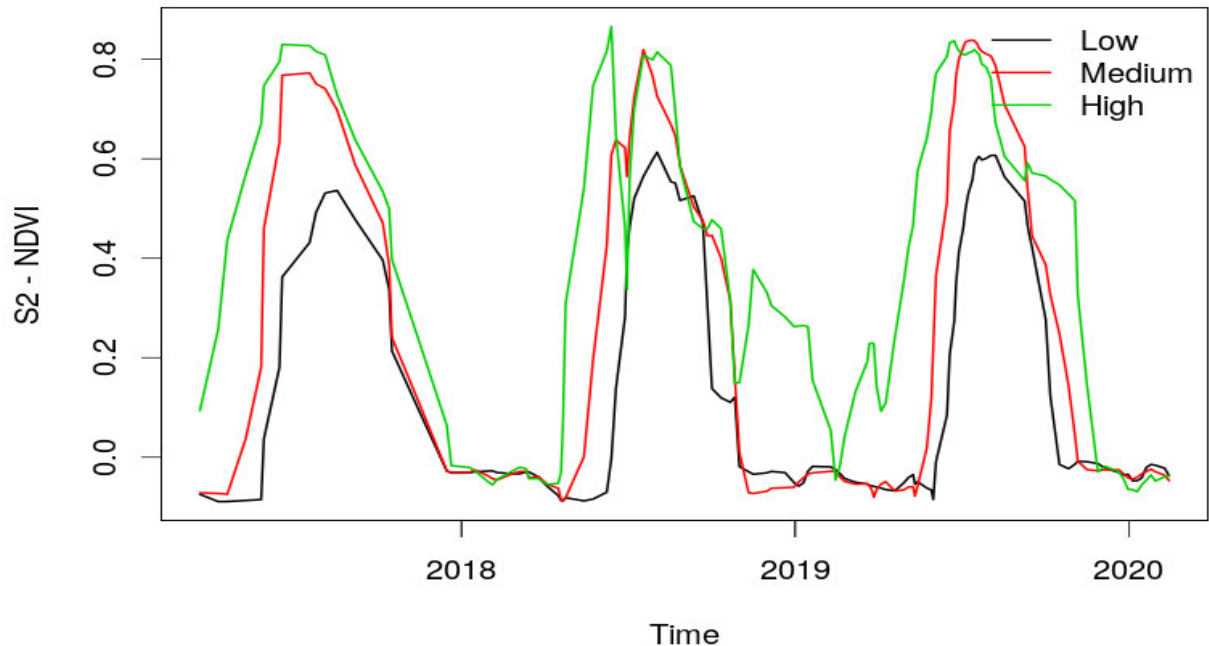


Fig. 8.3. Three-year seasonal trajectories of S2-derived NDVI values in selected PNGP pastures.

In order to obtain a dataset directly usable in model calibration/validation, leaf area index (LAI) was calculated following two alternative procedures. First, the biophysical processor available in the Sentinel Application Platform (SNAP) was used to obtain the seasonal trajectories presented in Fig. 8.2. The retrieval algorithm includes the inversion of a radiative transfer model and the application of machine learning (neural network). The full algorithm implementation, along with relevant literature, is described in http://step.esa.int/docs/extra/ATBD_S2ToolBox_L2B_V1.1.pdf.

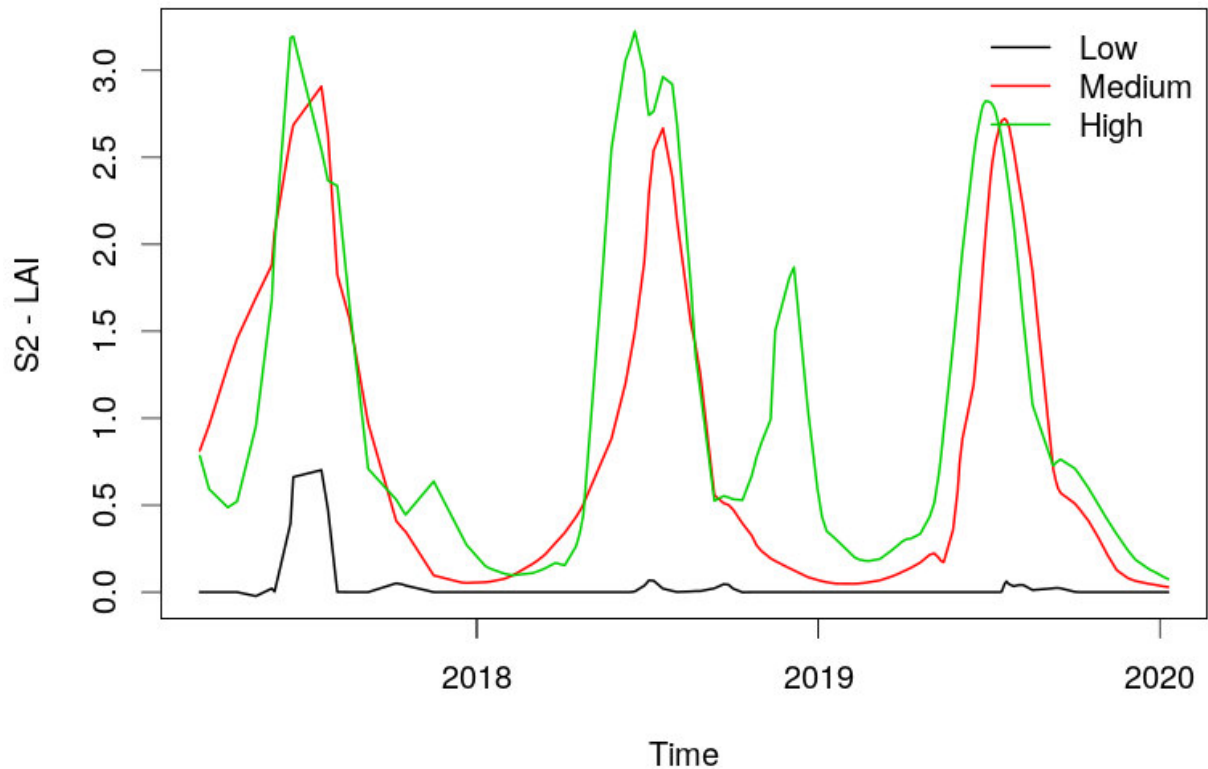


Fig. 8.2. Three-year seasonal trajectories of S2-derived LAI values in selected PNGP pastures.

Since the SNAP biophysical processor was mainly tested and implemented in crop fields or forests, it may lead to a poor representation of alpine pasture seasonal dynamics. For instance, this appears distinctly in the low productive subset of PNGP pastures shown in Fig. 8.2, where the signal is almost suppressed for the growing seasons 2018 and 2019. We thus opted to take advantage of the logarithmic relationship between LAI and NDVI, as calibrated in the alpine pasture of Col du Lautaret (unpublished data, courtesy of Philippe Choler - CNRS, Grenoble, France):

$$LAI = -1.323 \cdot \log[(a - NDVI) / 0.714] \quad (1)$$

where a is an empirically derived coefficient, adjusted based on the maximum seasonal NDVI value. The resulting seasonal trajectories are represented in Fig. 8.3.

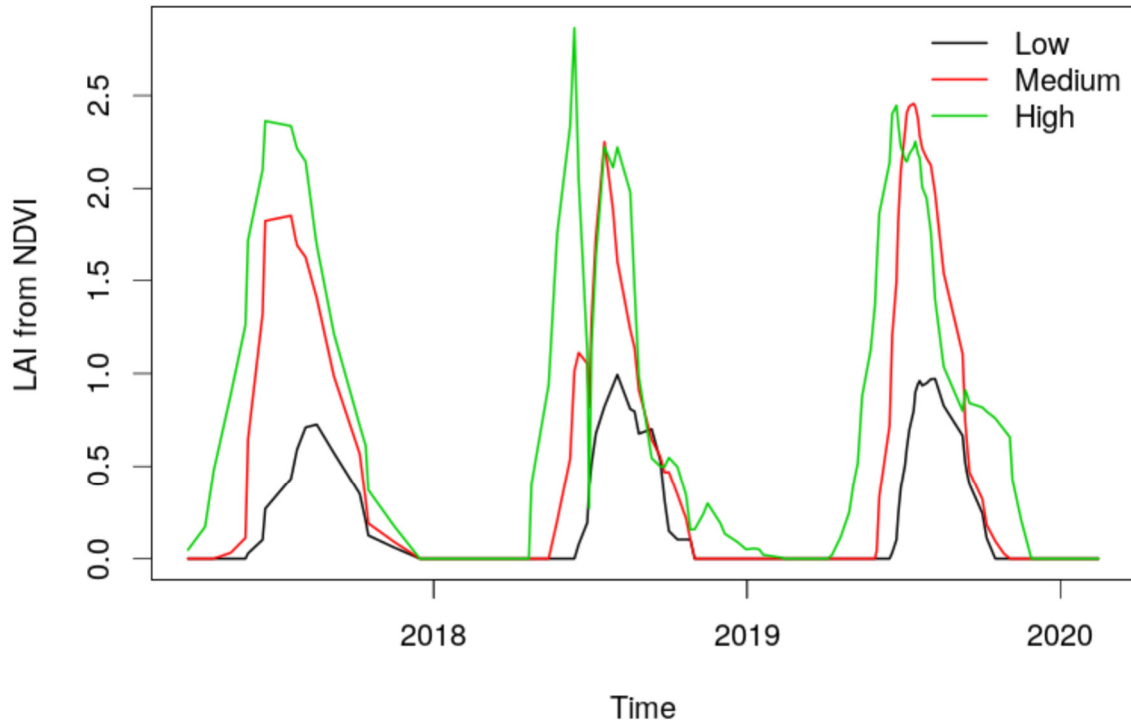


Fig. 8.4. Three-year seasonal trajectories of LAI, as calculated from Eq. (1).

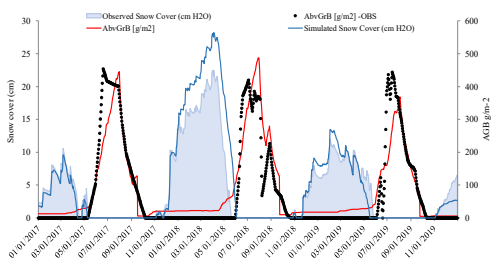
This second version of LAI-derived values is more consistent with NDVI trajectories and with the expected ranges of LAI in the study area.

Additional info to support the NDVI analysis is provided in Appendix D.

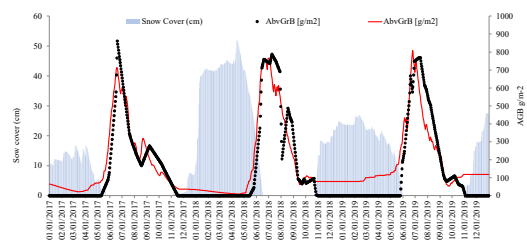
9 Simulations under future scenarios – based on macro-type calibration

Calibration results obtained with NDVI-derived LAI and AGB data were sufficiently accurate (exemplary results with DayCent in Fig. 9.1).

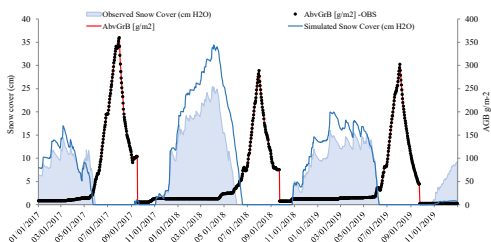
PNE-HP



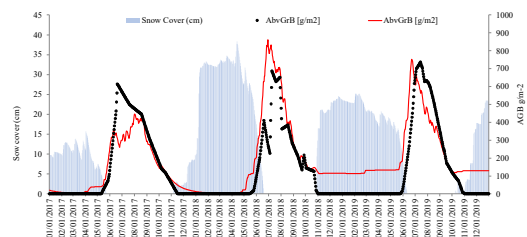
PNGP-HP



PNE-MP



PNGP-MP



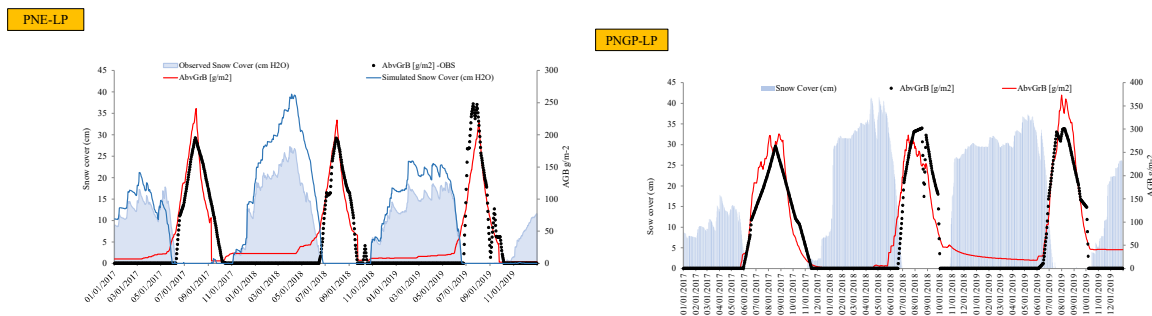


Fig. 9.1. Comparisons of DayCent simulations of aboveground biomass (AGB, g DM m⁻², red line) and snow cover (cm, H₂O, blue lines) with observations (black lines and grey areas, respectively) at PNE and PNGP for three macro-types (HP, MP, LP).

Possible impacts of future climate change were thus simulated for the three macro-types (HP: high productivity; MP: medium productivity; LP: low productivity) of both parks (PNE and PNGP) with DayCent and PaSim, recalibrated against NDVI-derived LAI and AGB data using the reference management as in Table 9.1. In the simulations, two future time-slices (2011-2040 and 2041-2070), reflect the assumptions of Representative Concentration Pathways (RCPs 4.5 and 8.5) with two increased levels of atmospheric CO₂ (450 and 540 ppm, respectively), compared to current conditions (400 ppm). RCP-timeframe combinations are indicated with acronyms, e.g. 451140 stands for RCP4.5 in the near future (2011-2040).

Table 9.1. Grazing periods in the three macro-types of both parks.

Gran Paradiso National Park	Grazing period 1		Grazing period 2	
	Start	End	Start	End
High productivity	152	186	244	263
Medium productivity	213	243	-	-
Low productivity	213	243	-	-

Ecrins National Park	Grazing period 1		Grazing period 2	
	Start	End	Start	End
High productivity	152	186	244	263
Medium productivity	152	186	244	263
Low productivity	213	243	- - -	- - -

While we can likely expect a longer growing season with higher temperatures in both parks (Fig. 9.2), the simulated aboveground biomass (Fig. 9.3) reflects the general tendency of PNE grasslands to benefit of future conditions, while late-season growth can be negatively affected in the PNGP (especially in the second peak of production for HP).

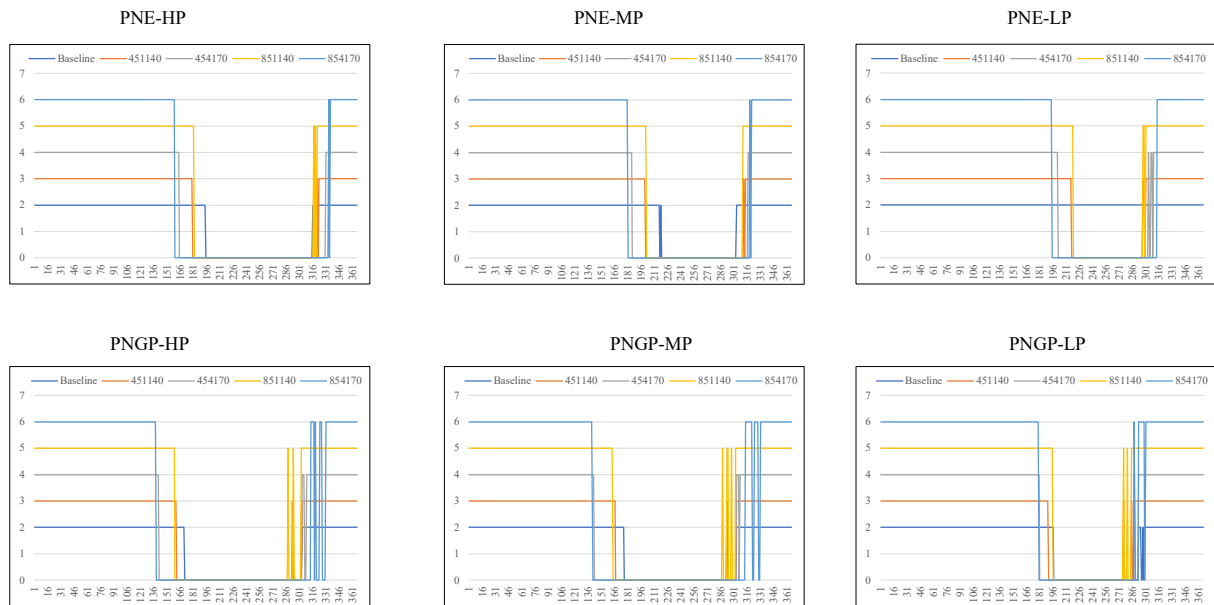


Fig. 9.2. Projected mean duration of the vegetation period for the baseline, near (2011-2040) and far (2041-2070) future, as predicted by DayCent with the ensemble of RCMs (CNRM-ALADIN, ICTP-RGCM4, and CMCC-CCLM4) for RCP 4.5 and 8.5 scenarios for the three macro-types (HP, MP, LP) of PNE and PNGP.

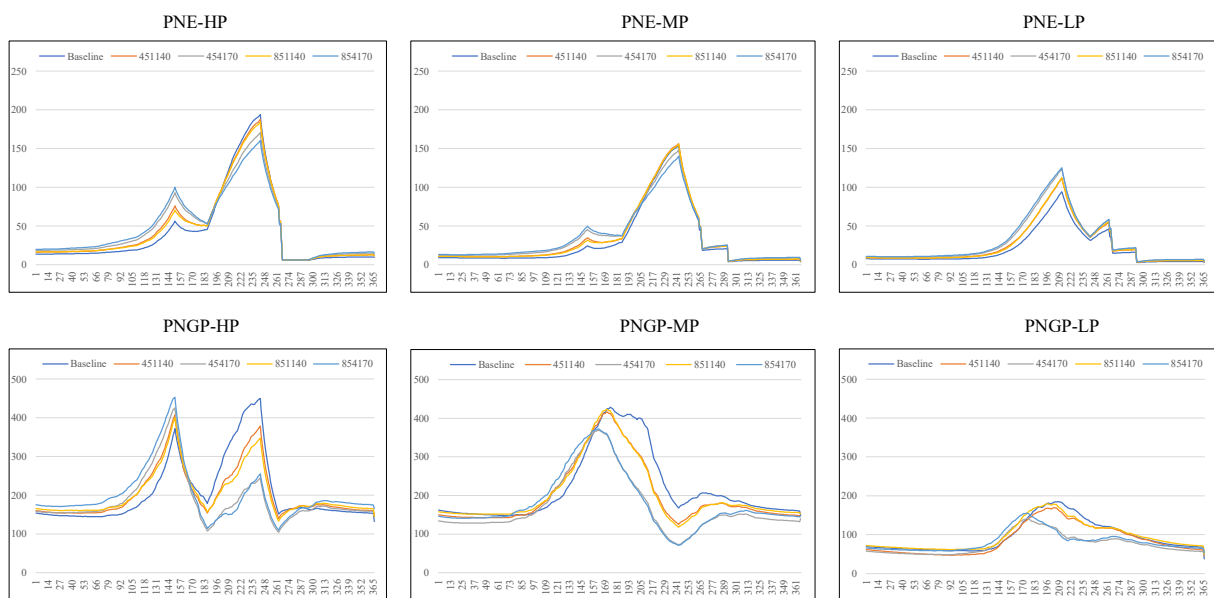


Fig. 9.3. Projected aboveground biomass mean pattern (g C m^{-2}) for the baseline, near (2011-2040) and far (2041-2070) future, as predicted by DayCent with the ensemble of RCMs (CNRM-ALADIN, ICTP-RGCM4, and CMCC-CCLM4) for RCP 4.5 and 8.5 for the three macro-types (HP, MP, LP) of PNE and PNGP.

Fig. 9.4 outlines, on a probabilistic basis, the trend towards greater biomass production at PNE (as shown for HP and LP) as we move towards higher temperatures and CO_2 levels.

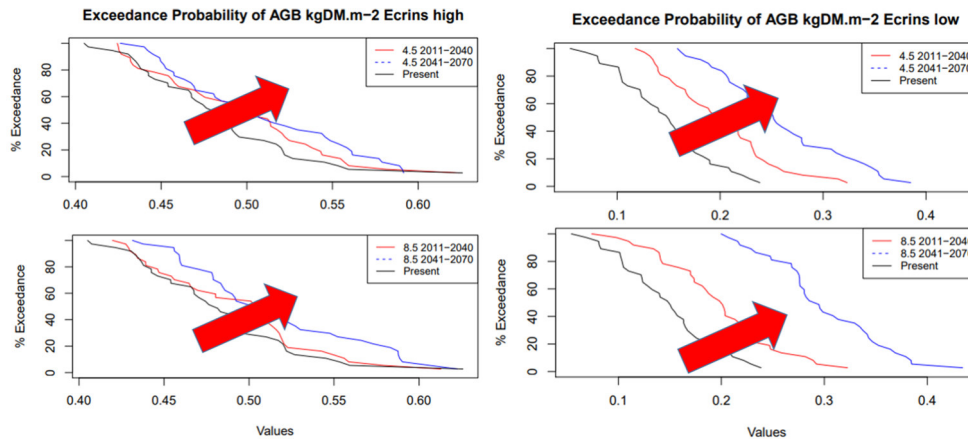


Fig. 9.4. Exceedance probability (%) distribution functions of PaSim-simulated annual values of present and future above ground biomass (kg DM m^{-2}) in the PNE, as predicted by the ensemble of RCMs (CNRM-ALADIN, ICTP-RGCM4, and CMCC-CCLM4) for RCP 4.5 and 8.5. The red arrows indicate the trend towards higher values with future scenarios.

A clear trend towards an earlier biomass peak under future climate scenarios was also estimated (Fig. 9.5).

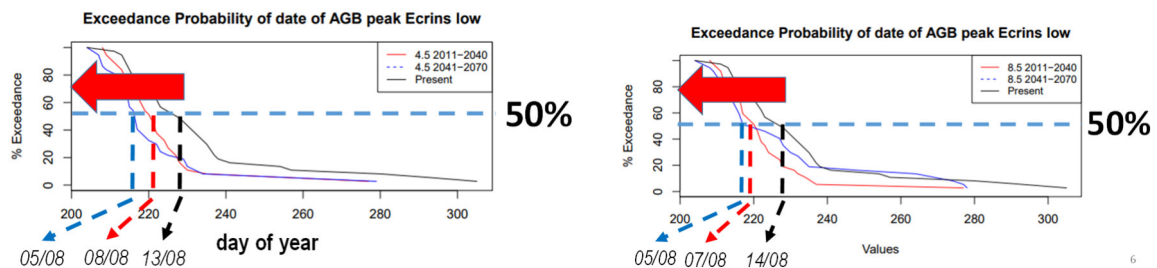


Fig. 9.5. Exceedance probability (%) distribution functions of present and future annual dates (days of year) of PaSim-simulated aboveground biomass peak in the PNE, as predicted by the ensemble of RCMs (CNRM-ALADIN, ICTP-RGCM4, and CMCC-CCLM4) for RCP 4.5 and 8.5. The red arrows indicate the trend towards earlier biomass peaks with future scenarios. Dates exceeding 0.5 probability are reported.

The expected reduction in soil water availability (Fig. 9.6) could increase the risk of summer fodder losses.

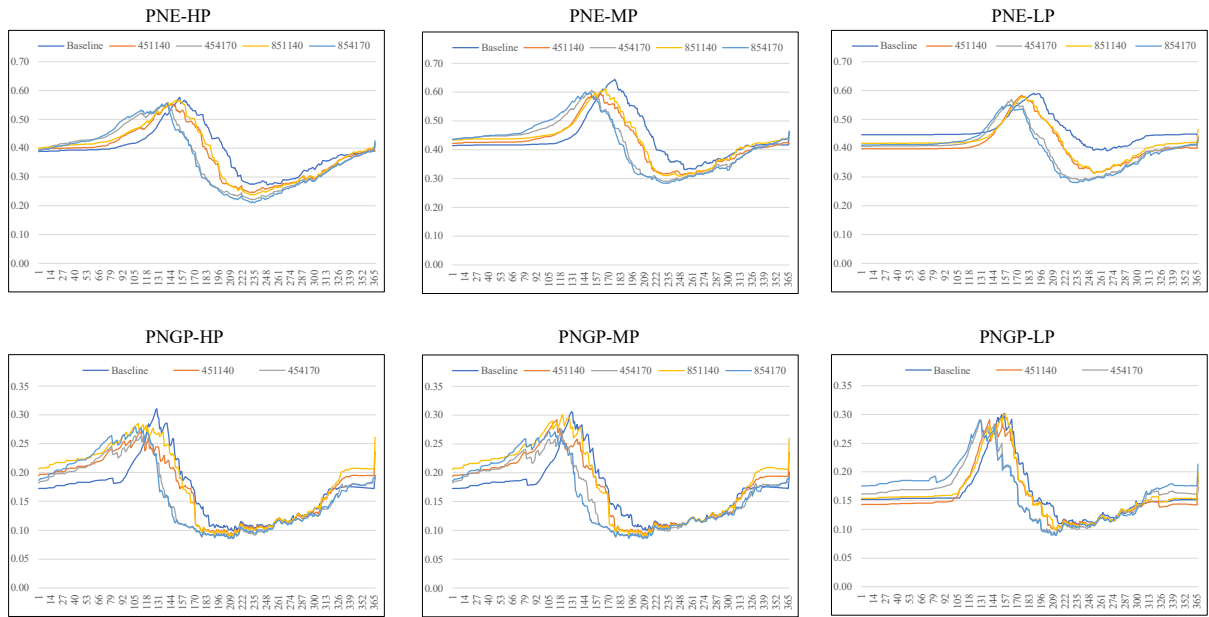


Fig. 9.6. Projected soil water content mean pattern ($m^3 m^{-3}$) for the baseline, near (2011-2040) and far (2041-2070) future, as predicted by DayCent with the ensemble of RCMs (CNRM-ALADIN, ICTP-RGCM4, and CMCC-CCLM4) for RCP 4.5 and 8.5 for the three macro-types (HP, MP, LP) of PNE and PNGP.

In terms of carbon (C) balance ($NEE < 0$: C sequestration; $NEE > 0$: C emission), the simulations (Fig. 9.7) indicate that C sinks in Alpine grasslands C sinks might turn into C sources with higher temperature/ CO_2 levels, especially during the dry season (e.g. at PNGP HP).

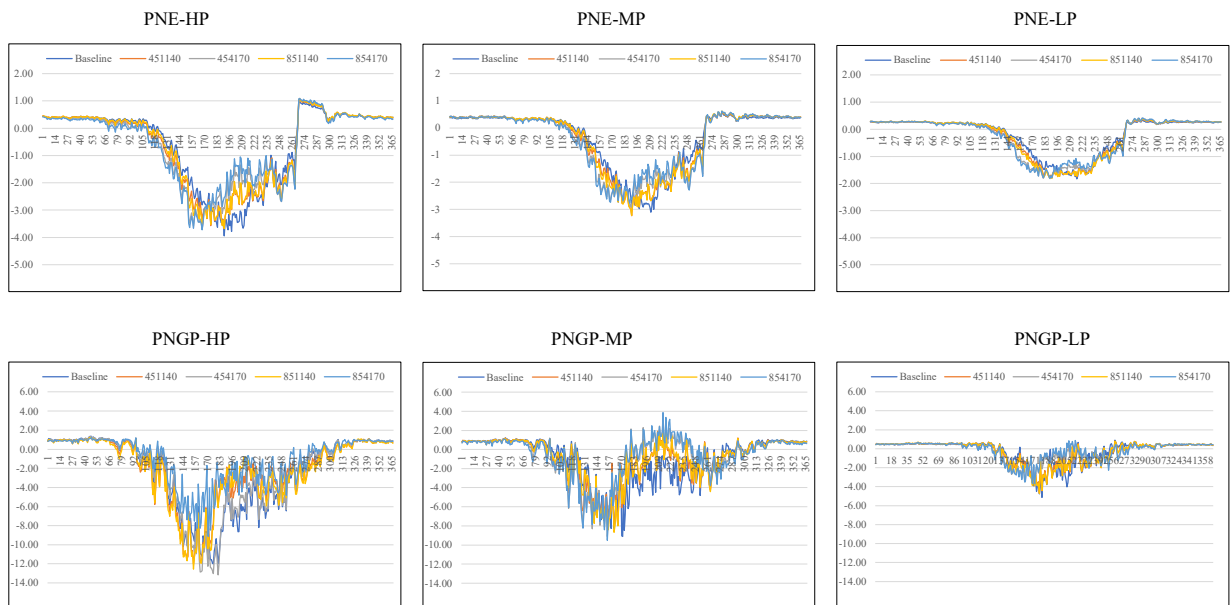


Fig. 9.7. Projected net ecosystem exchange (NEE) mean pattern ($g C m^{-2}$) for the baseline, near (2011-2040) and far (2041-2070) future, as predicted by DayCent with the ensemble of RCMs (CNRM-ALADIN, ICTP-RGCM4, and CMCC-CCLM4) for RCP 4.5 and 8.5 for the three macro-types (HP, MP, LP) of PNE and PNGP.

10 Concluding statements

The experimental and modelling framework developed so far underlines the big preparatory and progressive work done by partners in view of a robust assessment of the vulnerability of alpine pasturelands. By increasing knowledge on the response of these systems to external factors (e.g. via sensitivity analysis or random-forest machine learning), it has created the basis for an improved modelling work to the level of pasture macro-types representative of contrasting situations (beyond site-specific calibration, which has to be considered a preliminary step for a satisfactory use of models). The latter work, which has not been completed at this stage, is ongoing based on satellite-derived measurements. Its results will be embedded in the frame of the vulnerability assessment, whose implementation has been prepared in this deliverable thanks to exemplary climate-change based projection scenarios and will be completed with the assessment of alternative management practices in different pasture macro-types. Output variables as well as environmental and socio-economic drivers for the vulnerability assessment will be finalised there beyond the tentative lists put forward in previous deliverables (e.g. deliverable C.3).

11 References

- Breiman, L., 2001. Random Forests. *Machine Learning* 45, 5–32.
- De Martonne, E., 1942. Nouvelle carte mondiale de l'indice d'aridité. *Annales de Géographie* 51, 242-250. (in French)
- Diodato, N., Ceccarelli, M., 2004. Multivariate indicator Kriging approach using a GIS to classify soil degradation for Mediterranean agricultural lands. *Ecological Indicators* 4, 177-187.
- Dunford, R.W., Smith, A.C., Harrison, P.A., Hanganu, D., 2015. Ecosystem service provision in a changing Europe: adapting to the impacts of combined climate and socioeconomic change. *Landscape Ecology* 30, 443-461.
- Durand, Y., Giraud, G., Laternser, M., Etchevers, P., Merindol, L., Lesaffre, B., 2009. Reanalysis of 47 years of climate in the French Alps (1958–2005): Climatology and trends for snow cover. *Journal of Applied Meteorology and Climatology* 48, 2487–2512.
- Fakarayi, T., Mashapa, C., Gandiwa, E., Kativu, S., 2017. Pattern of land-use and land cover changes in Driefontein grassland important bird area, Zimbabwe. *Tropical Conservation Science* 8, 274-283.
- Galvagno, M., Wohlfahrt, G., Cremonese, E., Rossini, M., Colombo, R., Filippa, G., Julitta, T., Manca, G., Siniscalco, C., di Cella, U.M., Migliavacca, M., 2013. Phenology and carbon dioxide source/sink strength of a subalpine grassland in response to an exceptionally short snow season. *Environmental Research Letters* 8: 25008.
- Gibson, L., Münch, Z., Palmer, A., Mantel, S., 2018. Future land cover change scenarios in South African grasslands - implications of altered biophysical drivers on land management. *Heliyon* 4: e00693.
- Graux, A.-I., Bellocchi, G., Lardy, R., Soussana, J.-F., 2013. Ensemble modelling of climate change risks and opportunities for managed grasslands in France. *Agricultural and Forest Meteorology* 170, 114-131.
- Graux, A.-I., Lardy, R., Bellocchi, G., Soussana, J.-F., 2012. Global warming potential of French grassland-based dairy livestock systems under climate change. *Regional Environmental Change* 12, 751-763.

Hijmans, R.J., Cameron, S.E., Parra, J.L., Jones, P.G., Jarvis, A., 2005. Very high resolution interpolated climate surfaces for global land areas. *International Journal of Climatology* 25, 1965-1978.

Inglada, J., Vincent, A., Arias, M., Tardy, B., Morin, D., Rodes, I., 2017. Operational high resolution land cover map production at the country scale using satellite image time series. *Remote Sensing* 9: 95.

Isselstein, J., Jeangros, B., Pavlu, V., 2005. Agronomic aspects of extensive grassland farming and biodiversity management. *Agronomy Research* 10, 211-220.

Münch, Z., Okoye, P.I., Gibson, L., Mantel, S., Palmer, A., 2017. Characterizing degradation gradients through land cover change analysis in rural Eastern Cape, South Africa. *Geoscience Journal* 7, 1-7.

Nachtergaele, F., van Velthuizen, H., Verelst, L., 2008. The harmonized world soil database. version 1.0. *Fao/Iiasa/Isric/Iss-Cas/Jrc Version 1*, 34-37.

Oshiro, T.M., Perez, P.S., Baranauskas, J.A., 2012. How many trees in a random forest? In: ; Perner, P. (Ed.) *Proceedings of the Lecture Notes in Computer Science*. Springer, Berlin and Heidelberg, pp. 154-168.

Parton, W.J., Hartman, M., Ojima, D., Schimel, D., 1998. DAYCENT and its land surface submodel: description and testing. *Global and Planetary Change* 19, 35-48.

Peyraud, J.L., Peeters, A., De Vliegheer, A., 2012. Place et atouts des prairies permanentes en France et en Europe. *Fourrages* 211, 195-204. (in French)

Pontes, L.d.S., Louault, F., Carrère, P., Maire, V., Andueza, D., Soussana, J.-F., 2010. The role of plant traits and their plasticity in the response of pasture grasses to nutrients and cutting frequency. *Annals of Botany* 105, 957-965.

Pontes, L.d.S., Maire, V., Schellberg, J., Louault, F., 2015. Grass strategies and grassland community responses to environmental drivers: a review. *Agronomy for Sustainable Development* 35, 1297-1318.

Riedo, M., Grub, A., Rosset, M., Fuhrer, J., 1998. A Pasture Simulation model for dry matter production, and fluxes of carbon, nitrogen, water and energy. *Ecological Modelling* 105, 141-183.

Sándor, R., Barcza, Z., Acutis, M., Doro, L., Hidy, D., Köchy, M., Minet, J., Lellei-Kovács, E., Ma, S., Perego, A., Rolinski, S., Ruget, F., Sanna, M., Seddaiu, G., Wu, L., Bellocchi, G., 2017. Multi-model simulation of soil temperature, soil water content and biomass in Euro-Mediterranean grasslands: Uncertainties and ensemble performance. *European Journal of Agronomy* 88, 22-40.

Sándor, R., Picon-Cochard, C., Martin, R., Louault, F., Klumpp, K., Borrás, D., Bellocchi, G., 2018. Plant acclimation to temperature: Developments in the Pasture Simulation model. *Field Crops Research* 222, 238-255.

Schirpke, U., Kohlera, M., Leitinger, G., Fontana, V., Tasser, E., Tappeiner, U., 2017. Future impacts of changing land-use and climate on ecosystem services of mountain grassland and their resilience. *Ecosystem Services* 26, 79-94.

Silvestro, F., Gabellani, S., Rudari, R., Delogu, F., Laiolo, P., Boni, G., 2015. Uncertainty reduction and parameter estimation of a distributed hydrological model with ground and remote-sensing data. *Hydrology and Earth System Sciences* 19, 1727-1751.

Soudani, K., Hmimina, G., Delpierre, N., Pontallier, J.Y., Aubinet, M., Bonal, D., Caquet, B., de Grandcourt, A., Burban, B., Flechard, C., Guyon, D., Granier, A., Gross, P., Heinesh, B., Longdoz, B., Loustau, D., Moureaux, C., Ourcival, J.M., Rambal, S., Saint André, L., Dufrêne, E., 2012. Ground-based network of NDVI measurements for tracking temporal dynamics of canopy structure and vegetation phenology in different biomes. *Remote Sensing of Environment* 123, 234-245.

UNEP, 1993. World atlas of desertification. The United Nations Environment Programme, London, UK.

Van Oijen, M., Bellocchi, G., Höglind, M., 2018. Effects of climate change on grassland biodiversity and productivity: the need for a diversity of models. *Agronomy* 8: 14.

Appendix A - Sites description

This modelling study was carried out on three alpine sites. Oisans is located in the natural park of the Ecrins (France), while Torgnon and Entrelor are located in the national park of the Gran Paradiso (Italy).

1. Torgnon

Torgnon is located in the Aosta Valley in Italy, at 2109 m a.s.l.

Elevation	2109 m a.s.l
Longitude	7.3 E
Latitude	45.8
Dominant plant species	<i>Agrostis alpina</i> <i>Agrostis capillaris</i> <i>Agrostis rupestris</i> <i>Alchemilla xanthochlora</i> <i>Festuca nigrescens</i> <i>Leontodon hispidus</i> <i>Plantago alpina</i> <i>Plantago atrata</i> <i>Trifolium alpinum</i>
Management	Abandonment

a) Soil data

upper limit (cm from surface)	lower limit (cm from surface)	pH	Sand (%)	Silt (%)	Clay (%)	TOC (g kg ⁻¹)	TN (g kg ⁻¹)
0	20	4.5	45.2	41.7	13.1	71.9	5
20	60	5.2	52.1	43.3	4.6	19.9	1.1
60	100	5.4	71.7	26.8	1.5	11	0.6

b) Meteorological data

Year	Raw meteorological data Consolidated meteorological data % gap						
	Precipitation	Mean temperature	Average wind speed	Average radiation	Average water vapour pressure	[CO ₂]	[NH ₃]
	(mm yr ⁻¹)	(°C)	(m s ⁻¹)	(W cm ⁻²)	(kPa)	(ppm)	(ppm)
2009	0	3.02	3.11	169.23	0	380	2
	474.15	2.69	3.32	165.90	0.57		
	100%	8.94%	14.45%	8.93%	100%		
2010	0	1.78	2.09	162.15	0.27	380	2
	573	1.70	2.14	161.17	0.55		

	100%	1.23%	3.45%	1.21%	53.72%		
2011	0	3.93	1.63	171.56	0.32		
	718	3.93	1.62	171.54	0.57		
	100%	0.3%	5.31%	0.3%	1.82%		
2012	125	3.40	1.65	164.48	0.32		
	773	3.43	1.64	165.38	0.55		
	73.11%	0.31%	9.91%	0.31%	1.8%		
2013	522	2.66	1.68	159.90	0.32		
	1044	2.69	1.71	160.37	0.55		
	0.29%	0.27%	1.97%	0.56%	1.79%		
2014	542	3.38	1.61	157.72	0.26		
	1085	3.39	1.63	157.86	0.57		
	0.07%	0.03%	1.79%	0.03%	0.55%		
2015	408	4.40	1.68	173.72	0.34		
	817	4.40	1.70	173.70	0.58		
	0%	0%	0.7%	0%	0.98%		
2016	416	3.59	1.60	164.79	0.31		
	846	3.50	1.60	163.82	0.55		
	0.8%	0.8%	2.16%	0.8%	4.14%		
2017	352	3.78	1.83	176.54	0.37		
	710	3.84	1.87	175.35	0.53		
	1.9%	0.84%	9.2%	2.57%	3.74%		

In red and orange, the data that change respectively by a factor 2+ or 1.5+ between observation and input data of PaSim.

2. Entrelor

Entrelor occupies a narrow valley of the Italian Alps in Valle d'Aosta, at about 2100 m a.s.l.

Elevation	2100 m a.s.l
Longitude	7.1 E
Latitude	45.3 N
Dominant plant species	<i>Agrostis alpina</i> <i>Agrostis capillaris</i> <i>Agrostis rupestris</i> <i>Alchemilla xanthochlora</i> <i>Anthoxanthum odoratum</i> <i>Anthyllis vulneraria</i> <i>Carex sempervirens</i> <i>Festuca halleri</i> <i>Festuca nigrescens</i> <i>Festuca rubra</i> <i>Festuca violacea</i> <i>Helictotrichon versicolor</i> <i>Hieracium glaciale</i> <i>Juncus jacquinii</i> <i>Juncus trifidus</i> <i>Kobresia myosuroides</i> <i>Leontodon hispidus</i> <i>Nardus stricta</i> <i>Phleum alpinum</i> <i>Plantago alpina</i> <i>Plantago atrata</i> <i>Plantago serpentina</i> <i>Poa alpina</i> <i>Polygonum bistorta</i>

	<i>Trifolium alpinum</i> <i>Trifolium badium</i> <i>Trisetum flavescens</i>
Management	Grazing

a) Soil data

upper limit (cm from surface)	lower limit (cm from surface)	pH	Sand (%)	Silt (%)	Clay (%)	Bulk density (t m ⁻³)	Field capacity (m ³ m ⁻³)	Wilting point (m ³ m ⁻³)	Roots (%)	OM (%)	Minimum SWC (m ³ m ⁻³)	SHC (cm s ⁻¹)
0	20	8.1	36	56.5	7.5	1.34	0.35	0.115	3	1.8	0.11	0.00053
20	50								7		0.08	
50	100								13		0.05	
100	200								20		0.01	
200	300		27	66	7	1.38			23	0.9	0	
300	450								19			
450	600								10			
600	750								4			
750	900		45	48	7	1.41			0.11	1	0.7	

b) Meteorological data

Year	Consolidated meteorological data							
	Precipitation	Average minimum temperature	Average maximum temperature	Average wind speed	Average radiation	Average water vapour pressure	[CO ₂]	[NH ₃]
	(mm yr ⁻¹)	(C°)	(°C)	(m s ⁻¹)	(J cm ⁻²)	(%)	(ppm)	(ppm)
2008	1272.7	6.13	-2.43	1.48	1196.8	1,85	380.828	2
2009	934.7	6.53	-2.62	1.50	1209.3	1,96	382.777	
2010	902.8	5.32	-3.48	1.51	1203.9	0,91	384.800	
2011	888.4	7.55	-1.65	1.36	1236.2	2,95	386.952	
2012	804.6	6.80	-2.07	1.40	1224.4	2,36	389.128	
2013	1019.3	5.87	-2.86	1.43	1195.2	1,51	391.274	
2014	865	7.20	-1.55	1.51	1203.5	2,83	393.421	
2015	866.8	8.57	-1.08	1.34	1239.5	3,74	395.583	

3. Oisans

The French site of Oisans is located in the departments of Isère and Hautes-Alpes, spanning an altitude from 1800 to 2400 m a.s.l.

Elevation	1800-2400 m a.s.l
Longitude	6.4 E
Latitude	45.1 N
Dominant plant species	<i>Alchemilla pentaphylla</i> <i>Carex myosuroides</i> <i>Carex sempervirens</i>

	<i>Patzkea paniculata</i> <i>Vaccinium uliginosum</i>
Management	Grazing

a) *Soil data*

• site 1

upper limit (cm from surface)	lower limit (cm from surface)	pH	Sand (%)	Silt (%)	Clay (%)	TOC (g/kg)
0	5	5.86	15.1	42.2	42.7	109
5	20	4.94	15.3	41.8	37.5	52.9
20	30	4.84	32.1	37.6	30.3	34.6
30	45	4.79	31.4	39.1	29.5	24.2

• site 2

upper limit (cm from surface)	lower limit (cm from surface)	pH	Sand (%)	Silt (%)	Clay (%)	TOC (g kg ⁻¹)
0	5	5.04	15.4	39.4	45.2	214
5	25	4.71	28.7	37.7	33.6	69.6
25	60	4.85	35.5	38	26.5	35.6
60	100	5.23	65.5	22.7	11.8	13.9

• site 3

upper limit (cm from surface)	lower limit (cm from surface)	pH	Sand (%)	Silt (%)	Clay (%)	TOC (g kg ⁻¹)
0	5	4.52	17.8	42.6	39.6	116
5	20	4.85	46.4	37.8	15.8	30.5
20	60	5.38	55.4	34.4	10.2	15

• site 4

upper limit (cm from surface)	lower limit (cm from surface)	pH	Sand (%)	Silt (%)	Clay (%)	TOC (g kg ⁻¹)
0	5	6.52	53.3	25.1	21.6	162
5	15	6.69	55.4	25.8	18.8	115
15	30	7.49	71	18.5	10.4	19.9
30	40	8.3	50.8	27.6	20.3	5.83

• site 5

upper limit (cm from surface)	lower limit (cm from surface)	pH	Sand (%)	Silt (%)	Clay (%)	TOC (g kg ⁻¹)
0	10	5.06	16.9	55.6	27.5	31.2
10	20	4.45	26.5	50.0	23.5	16.6
20	30	4.6	49.4	33.3	17.3	12.9
30	50	4.72	19.1	52.7	28.2	17.8
50	150	NA	NA	NA	NA	NA

b) *Meteorological data*

• Site 1

Year	Consolidated meteorological data
------	----------------------------------

	Precipitation	Mean temperature	Average wind speed	Average radiation	Average water vapour pressure	[CO ₂]	[NH ₃]
	(mm yr ⁻¹)	(°C)	(m s ⁻¹)	(J cm ⁻²)	(kPa)	(ppm)	(ppm)
2004	598.81	4.82	1.76	114.70	0.57	380	2
2005	593.03	3.72	1.47	118.43	0.56		
2006	690.68	5.13	1.72	115.26	0.58		
2007	559.48	5.03	1.67	111.73	0.57		

- site 2, site 3, site 4 and site 5

Year	Precipitation	Mean temperature	Average wind speed	Average radiation	Average water vapour pressure	[CO ₂]	[NH ₃]
	(mm yr ⁻¹)	(°C)	(m s ⁻¹)	(J cm ⁻²)	(kPa)	(ppm)	(ppm)
2004	525.47	3.08	1.83	120.44	0.65	380	2
2005	516.84	2.11	1.54	125.00	0.63		
2006	621.13	3.21	1.68	121.04	0.66		
2007	456.67	3.23	1.59	116.50	0.64		

Appendix B - Site-specific parameterisation data (PaSim)

1. Torgnon

	Soil layer					
	1	2	3	4	5	6
Latitude N (rad)	0.8001					
Slope (rad)	0.232					
Orientation (rad)	0.07					
Altitude (m)	2109					
Depth of the layer (mm)	0-20	20-59	59-137	137-294	294-529	529-843
Ground limit layer (mm)	1000					
Fraction of legume (kg kg ⁻¹)	0.03					
Bulk Density (kg l ⁻¹)	1.48	1.48	1.48	1.56	1.65	1.78
Fraction of sand (-)	0.452	0.452	0.452	0.493	0.521	0.673
Fraction of clay (-)	0.131	0.131	0.131	0.08	0.046	0.022
Fraction of silt (-)	0.417	0.417	0.417	0.427	0.433	0.305
pH	5.14					

2. Entrelor

a) Alto

	Soil layer					
	1	2	3	4	5	6
Latitude N (rad)	0.795					
Slope (rad)	0.01					
Orientation (rad)	0.00					
Altitude (m)	2200					
Depth of the layer (mm)	0-20	20-55	55-125	125-266	266-477	477-759
Ground limit layer (mm)	900					
Fraction of legume (kg kg ⁻¹)	0.11					
Bulk Density (kg l ⁻¹)	1.34	1.34	1.34	1.34	1.38	1.41
Fraction of sand (-)	0.36	0.36	0.36	0.318	0.27	0.276
Fraction of clay (-)	0.075	0.075	0.075	0.073	0.07	0.07
Fraction of silt (-)	0.565	0.565	0.565	0.609	0.66	0.654
pH	8.1					

The grazing period was split into four periods of six days each.

Year	Dates (day of year) Duration of grazing season (number of days) Stocking rate (nb animals m ⁻²) Weight of the animal (kg animal ⁻¹)
2008	
2009	
2010	206
2011	24
2012	0.0000114
2013	625
2014	
2015	

b) Basso

Parameters	Soil layer
------------	------------

	1	2	3	4	5	6
Latitude N (rad)	0.795					
Slope (rad)	0.01					
Orientation (rad)	0.00					
Altitude (m)	2143					
Depth of the layer (mm)	0-20	20-55	55-125	125-266	266-477	477-759
Ground limit layer (mm)	900					
Fraction of legume (kg kg ⁻¹)	0.11					
Bulk Density (kg l ⁻¹)	1.34	1.34	1.34	1.34	1.38	1.41
Fraction of sand (-)	0.36	0.36	0.36	0.318	0.27	0.276
Fraction of clay (-)	0.075	0.075	0.075	0.073	0.07	0.07
Fraction of silt (-)	0.565	0.565	0.565	0.609	0.66	0.654
pH	8.1					

The first grazing period was split into four periods of five days each.

Year	Dates (Julian day)		Duration of pasture (number of days)		Stocking rate (nb animals m ⁻²)		Weight of the animal (kg animal ⁻¹)	
	1				2			
2008								
2009								
2010	186				243			
2011	20				6			
2012	0.000012				0.000012			
2013	625				625			
2014								
2015								

3. Oisans

a) Site 1

Parameters	Soil layer					
	1	2	3	4	5	6
Latitude N (rad)	0.82					
Slope (rad)	0.08					
Orientation (rad)	0.00					
Altitude (m)	2055					
Depth of the layer (mm)	0-20	20-40	40-71	71-140	140-243	243-381
Ground limit layer (mm)	450					
Fraction of legume (kg kg ⁻¹)	0.12					
Bulk Density (kg l ⁻¹)	1.248	1.248	1.268	1.278	1.3	1.332
Fraction of sand (-)	0.151	0.151	0.189	0.207	0.255	0.317
Fraction of clay (-)	0.427	0.427	0.392	0.375	0.345	0.298
Fraction of silt (-)	0.422	0.422	0.419	0.418	0.4	0.385
pH	4.9					

The grazing period was split into eight periods of 10 days each.

year	Dates (day of year) Duration of pasture (number of days) Stocking rate (nb animals m ⁻²) Weight of the animal (kg animal ⁻¹)
2004	180
2005	80
2006	1.1406e-5
2007	625

b) Site 2

Parameters	Soil layer					
	1	2	3	4	5	6
Latitude N (rad)	0.82					
Slope (rad)	0.08					
Orientation (rad)	0.00					
Altitude (m)	2220					
Depth of the layer (mm)	0-20	20-59	59-173	173-294	294-529	529-843
Ground limit layer (mm)	1000					
Fraction of legume (kg kg ⁻¹)	0.12					
Bulk Density(kg l ⁻¹)	1.248	1.256	1.309	1.323	1.357	1.494
Fraction of sand (-)	0.154	0.185	0.287	0.306	0.355	0.587
Fraction of clay (-)	0.452	0.425	0.336	0.316	0.265	0.151
Fraction of silt (-)	0.394	0.390	0.377	0.378	0.380	0.262
pH	5					

year	Dates (Julian day) Duration of pasture (number of days) Stocking rate (nb animals m ⁻²) Weight of the animal (kg animal ⁻¹)								
	1	2	3	4	5	6	7	8	9
2004	182	190	197	205	213	220	230	240	250
2005	5	5	5	5	5	5	5	5	10
2006	0.001095	0.001095	0.001095	0.001095	0.001095	0.001095	0.001095	0.001095	0.001095
2007	625	625	625	625	625	625	625	625	625

c) Site 3

Parameters	Soil layer					
	1	2	3	4	5	6
Latitude N (rad)	0.82					
Slope (rad)	0.08					
Orientation (rad)	0.00					
Altitude (m)	2434					
Depth of the layer (mm)	0-20	20-43	43-89	89-182	182-321	321-507
Ground limit layer (mm)	600					
Fraction of legume (kg kg ⁻¹)	0.12					
Bulk Density(kg l ⁻¹)	1.264	1.264	1.425	1.454	1.525	1.536
Fraction of sand (-)	0.178	0.178	0.420	0.464	0.542	0.554
Fraction of clay (-)	0.396	0.396	0.194	0.158	0.109	0.102
Fraction of silt (-)	0.426	0.426	0.385	0.378	0.348	0.344

pH	5.2
----	-----

Year	Dates (day of year) Duration of pasture (number of days) Stocking rate (nb animals m ⁻²) Weight of the animal (kg animal ⁻¹)								
	1	2	3	4	5	6	7	8	9
2004	182	190	197	205	213	220	230	240	250
2005	5	5	5	5	5	5	5	5	10
2006	0.000365	0.000365	0.000365	0.000365	0.000365	0.000365	0.000365	0.000365	0.000365
2007	625	625	625	625	625	625	625	625	625

d) Site 4

Parameters	Soil layer					
	1	2	3	4	5	6
Latitude N (rad)	0.82					
Slope (rad)	0.08					
Orientation (rad)	0.00					
Altitude (m)	2640					
Depth of the layer (mm)	0-20	20-40	40-65	65-126	126-217	217-339
Ground limit layer (mm)	400					
Fraction of legume (kg kg ⁻¹)	0.12					
Bulk density (kg l ⁻¹)	1.421	1.421	1.436	1.446	1.532	1.563
Fraction of sand (-)	0.533	0.533	0.546	0.554	0.670	0.650
Fraction of clay (-)	0.216	0.216	0.199	0.188	0.126	0.136
Fraction of silt (-)	0.251	0.251	0.255	0.258	0.204	0.214
pH	7.7					

Year	Dates (day of year) Duration of pasture (number of days) Stocking rate (nb animals m ⁻²) Weight of the animal (kg animal ⁻¹)								
	1	2	3	4	5	6	7	8	9
2004	210	215	220	225	230	235	240	245	250
	5	5	5	5	5	5	5	5	10
	0.000365	0.000365	0.000365	0.000365	0.000365	0.000365	0.000365	0.000365	0.000365
	625	625	625	625	625	625	625	625	625
2005	210	215	220	225	230	235	240	245	250
	5	5	5	5	5	5	5	5	10
	0.000365	0.000365	0.000365	0.000365	0.000365	0.000365	0.000365	0.000365	0.000365
	625	625	625	625	625	625	625	625	625
2006	210	215	220	225	230	235	240	245	250
	5	5	5	5	5	5	5	5	10
	0.000365	0.000365	0.000365	0.000365	0.000365	0.000365	0.000365	0.000365	0.000365
	625	625	625	625	625	625	625	625	625
2007	210	215	220	225	230	235	240	245	250
	5	5	5	5	5	5	5	5	10
	0.000365	0.000365	0.000365	0.000365	0.000365	0.000365	0.000365	0.000365	0.000365
	625	625	625	625	625	625	625	625	625

e) Site 5

Parameters	Soil layer					
	1	2	3	4	5	6
Latitude N (rad)	0.82					
Slope (rad)	0.08					
Orientation (rad)	0.00					
Altitude (m)	2530					
Depth of the layer (mm)	0-20	20-40	40-71	71-140	140-243	243-381
Ground limit layer (mm)	450					
Fraction of legume (kg kg ⁻¹)	0.12					
Bulk Density (kg l ⁻¹)	1.248	1.248	1.268	1.278	1.3	1.332
Fraction of sand (-)	0.151	0.151	0.189	0.207	0.255	0.317
Fraction of clay (-)	0.427	0.427	0.392	0.375	0.345	0.298
Fraction of silt (-)	0.422	0.422	0.419	0.418	0.4	0.385
pH	4.9					

Appendix C - List of PaSim vegetation parameters

Parameters	Description	Variation range
PARAM_SLAM	Maximum specific leaf area ($\text{m}^2 \text{kg}^{-1}$)	20 - 35
PARAM_TASUMREP	Normalization factor for development (K-d)	200 - 250
PARAM_DAH	Soil depth below which there is neither plant N uptake, nor soil texture effect of active SOM decomposition (m)	0.1 - 0.3
PARAM_DEVEAR	Development stage at which ear emergence starts (-)	0.4 - 0.64
PARAM_FCR	Fractional C content of root structural dry matter (kg C kg^{-1})	0.3 - 0.56
PARAM_FCSH	Fractional C content of shoot structural dry matter (kg C kg^{-1})	0.3 - 0.56
PARAM_FNREF	Parameter controlling nitrogen concentration of structural dry matter (kg N kg^{-1})	0.01 - 0.03
PARAM_HCANMAX	Flowering plant height, highest leaf not elongated (m)	0.5 - 0.9
PARAM_KTURNRT20	Rate parameter for root turnover at 20 °C (d^{-1})	0.008 - 0.016
PARAM_KTURNSSH20	Rate parameter for shoot turnover at 20 °C (d^{-1})	0.036 - 0.06
PARAM_NDFEAR	Fraction of fibres in the total ear ingested (%)	0.6 - 0.9
PARAM_NDFLAM	Fraction of fibres in the total lam ingested (%)	0.4 - 0.7
PARAM_NDFSTEM	Fraction of fibres in the total stem and sheaths ingested (%)	0.5 - 0.8
PARAM_NTOTMAX	Maximum of the total nitrogen concentration in plant (kg N kg^{-1})	0.02 - 0.04
PARAM_PMCO2VEG	Light-saturated leaf photosynthetic rate at 20°C for vegetative stage ($\mu\text{mol m}^{-2} \text{s}^{-1}$)	15 - 25
PARAM_PMCO2REP	Light-saturated leaf photosynthetic rate at 20°C for reproductive stage ($\mu\text{mol m}^{-2} \text{s}^{-1}$)	10 - 20
PARAM_DNDFLAM1	Fraction of digestible fibres in total fibres, in age class 1 of lamina (-)	0.81-1
PARAM_DNDFLAM2	Fraction of digestible fibres in total fibres, in age class 2 of lamina (-)	0.67-0.87
PARAM_DNDFLAM3	Fraction of digestible fibres in total fibres, in age class 3 of lamina (-)	0.53-0.73
PARAM_DNDFLAM4	Fraction of digestible fibres in total fibres, in age class 4 of lamina (-)	0.25-0.45
PARAM_DNDFSTEM1	Fraction of digestible fibres in total fibres, in age class 1 of stem (-)	0.82-1
PARAM_DNDFSTEM2	Fraction of digestible fibres in total fibres, in age class 2 of stem (-)	0.69-0.89
PARAM_DNDFSTEM3	Fraction of digestible fibres in total fibres, in age class 3 of stem (-)	0.56-0.76
PARAM_DNDFSTEM4	Fraction of digestible fibres in total fibres, in age class 4 of stem (-)	0.3-0.5
PARAM_DNDFEAR1	Fraction of digestible fibres in total fibres, in age class 1 of ear (-)	0.83-1
PARAM_DNDFEAR2	Fraction of digestible fibres in total fibres, in age class 2 of ear (-)	0.67-0.87
PARAM_DNDFEAR3	Fraction of digestible fibres in total fibres, in age class 3 of ear (-)	0.53-0.73
PARAM_DNDFEAR4	Fraction of digestible fibres in total fibres, in age class 4 of ear (-)	0.25-0.45
PARAM_KFACTOR	Temperature dependence factor of the soil respiration (-)	0.2-0.9
Water content of lower soil boundary layer in spring ($\text{m}^3 \text{m}^{-3}$)		0.4-0.7
Water content of lower soil boundary layer in autumn ($\text{m}^3 \text{m}^{-3}$)		0.4-0.7
Average temperature of lower soil boundary layer (K)		278.9-288.9

Amplitude of temperature of lower soil boundary layer (K)	6.8-9.8
Phase of temperature of lower soil boundary layer (rad)	1.6-2.6
NH ₄ ⁺ deposition other than gaseous NH ₃ (kg N m ⁻² d ⁻¹)	1.35-1.55
NO ₃ ⁻ deposition (kg N m ⁻² d ⁻¹)	1.4-1.6
Parameter a for soil NH ₄ ⁺ partitioning (-)	1-1.15
Parameter b for soil NH ₄ ⁺ partitioning (-)	0.55-0.75

Appendix D - NDVI data analysis

In order to expand the dataset for model calibration, we explored the possibility to translate remote sensing-derived NDVI data into biomass and LAI data via conversion equations.

Site description

NDVI measurements were carried out by the FLUXALP station at Lautaret-Charmase, in the north of the Ecrins Natural Park, in the commune of Le Monétier-les-Bains (05220), locality « Pré des Charmasses ». It is a subalpine meadow located at 2050 m a.s.l., dominated by *Patzkea (Festuca) paniculata*. NDVI data acquisition was performed using Campbell Scientific CR3000 with the ESE sensor (Fig. D1; for more technical details on the sensor see Soudani et al., 2012). NDVI time series provide efficient estimates of photosynthetic biomass and are accurate estimates of the dates of major phenological events such as bud burst. The sensor used can replace and exceed visual observations. NDVI ground measurement network provides the data necessary for the calibration and direct validation of observations and satellite products (Soudani et al., 2012).



Fig. D.1. NDVI sensor.

What is NDVI?

The Normalized Difference Vegetation Index (NDVI) quantifies vegetation by measuring the difference between the near infrared (which vegetation strongly reflects) and red light (which vegetation absorbs). NDVI always varies from -1 to +1, the negative values corresponding to surfaces other than plant cover, such as snow, water or clouds for which the reflectance in red is greater than that of the near infrared. NDVI is a standardized way of measuring healthy vegetation when its values are positive, usually between 0.1 and 0.7. High NDVI values indicate healthier vegetation, while low NDVI indicate a land with little or no vegetation.

NDVI data

We extracted daily NDVI values measured with the ESE sensor from 10/17/2012 to 07/20/2019, which are shown graphically in Fig. D.2.

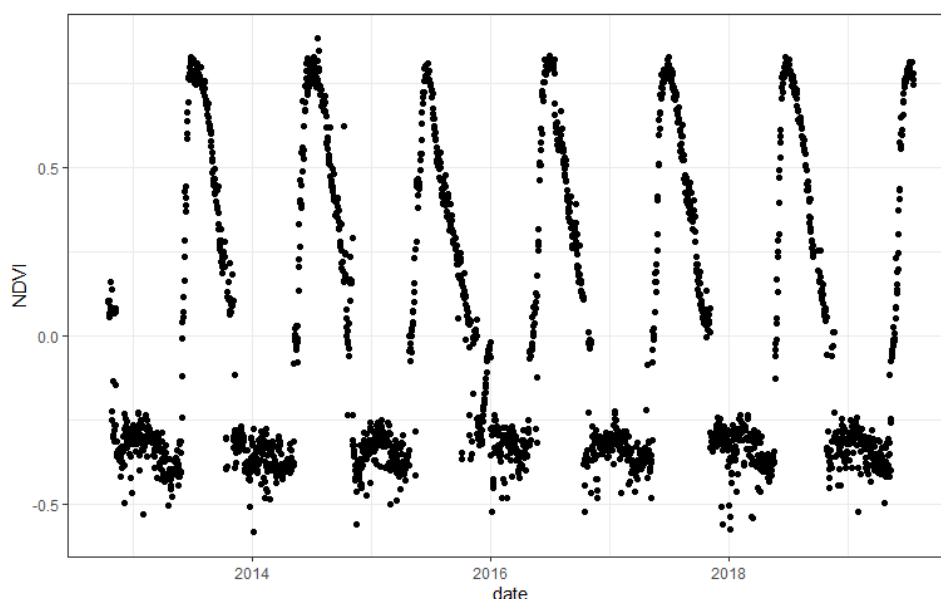


Fig. D.2. Interannual dynamics of NDVI (FLUXALP Lautaret-Charmase station, PNE, France).

This figure shows the temporal dynamics of the structure and phenology of the canopy at a daily time step (NDVI values <0 do not represent the canopy).

Calibration data

Correlation curves connect NDVI to LAI and aboveground biomass (AGB) to LAI.

Relation between the above-ground biomass AGB (g m⁻²) and leaf area index LAI (m² m⁻²)

The relationship between AGB and LAI was based on the meters of leaf area observed after cutting aerial vegetation and sorting green material. The equation looks like this:

$$AGB = 56.26 LAI + 15.29$$

which is illustrated in Fig. D.3.

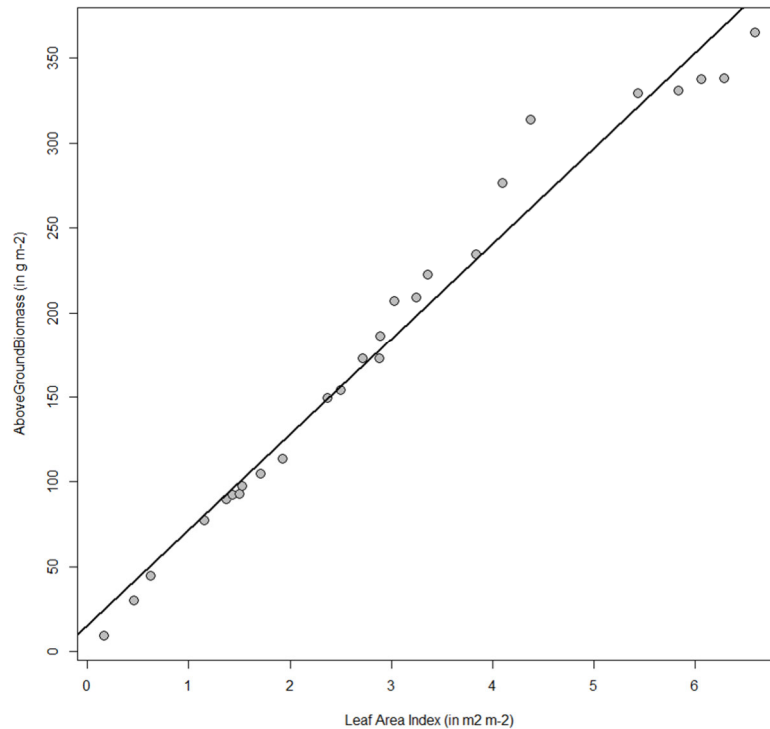


Fig. D.3. Relation between leaf area index (LAI) and above ground biomass (AGB).

AGB and LAI values are related as data points tend to line up around the regression line.

Relationship between NDVI and LAI (m² m⁻²)

The relationship between LAI and NDVI was based on NDVI ground measurements using a portable field device, calculated with the following equation:

$$LAI = -1.323 \max\left(0; \log\left(\frac{0.88 - NDVI}{0.714}\right)\right)$$

LAI is a suitable indicator of plant growth and biomass, as well as the density of a stand. It is a dimensionless quantity with always positive values, which generally varies from 0 for bare soils to 5 m² m⁻² for grasslands, and 8 m² m⁻² for dense temperate forests. For much closed tropical forests or coniferous forests, LAI value can exceed 15 m² m⁻².

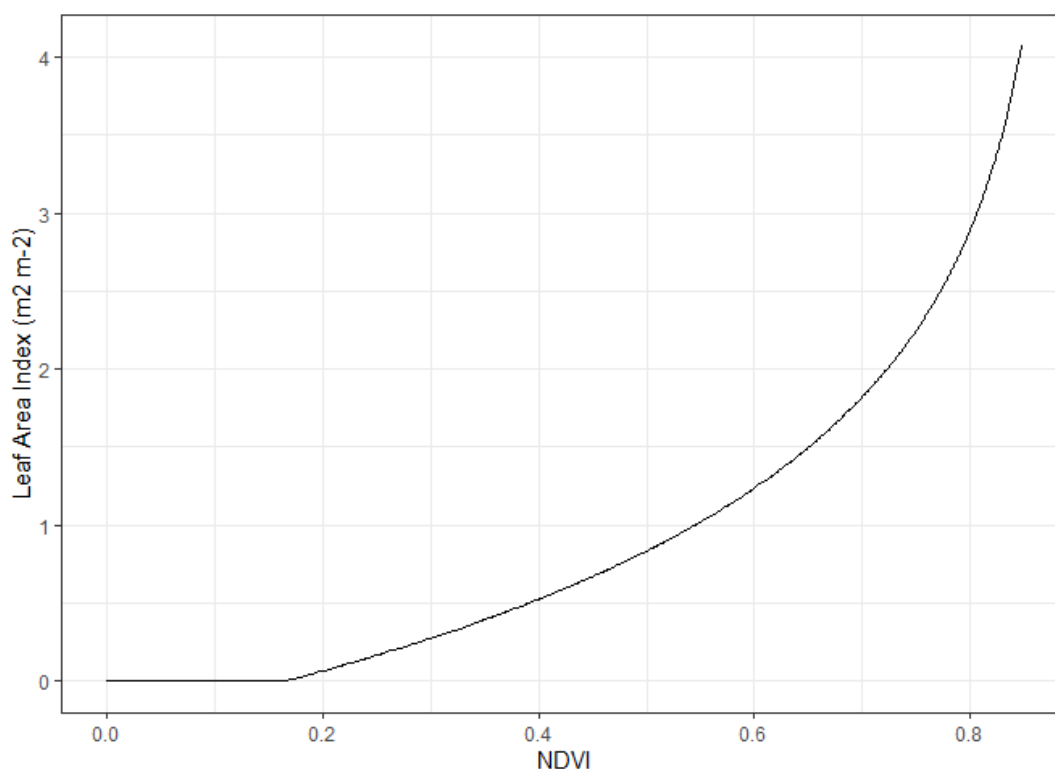


Fig. D.4. Relation between NDVI and leaf area index (LAI).

Fig. D.4 shows a logarithmic relationship between NDVI and LAI. The continuity of the curve indicates that the two variables are fairly correlated.

Combination of the two relations

The following equation gives the relationship between AGB and NDVI:

$$AGB = -74.432 * \max\left(0; \log\left(\frac{0.88 - NDVI}{0.714}\right)\right) + 15.25$$

The latter converts NDVI values into aboveground biomass (AGB) as illustrated in Fig. D5, which represents a logarithmic curve starting from 0 and increasing as NDVI increases. Observed negative NDVI values were not represented.

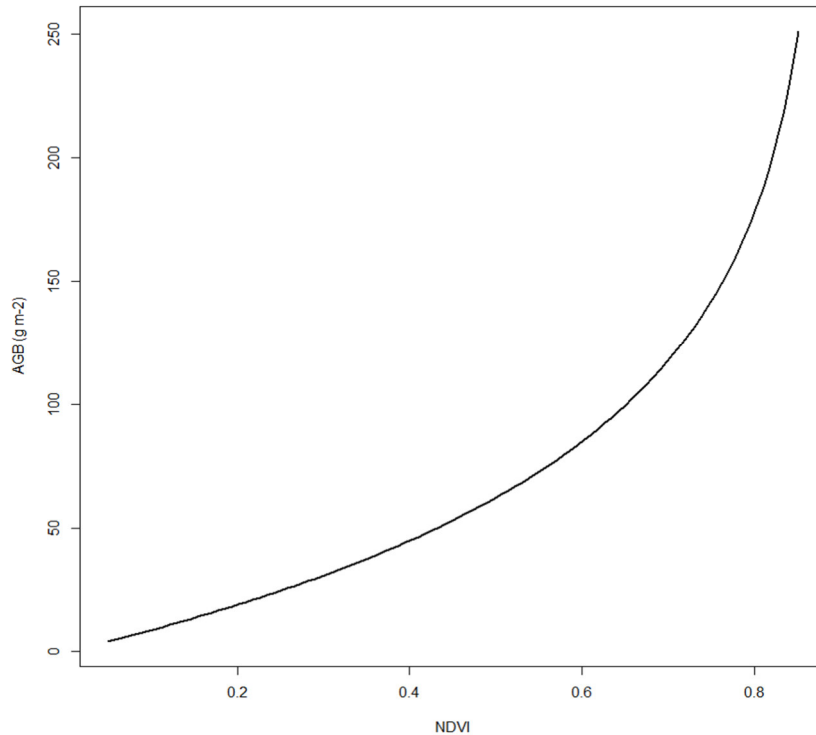


Fig. D.5. Relation between NDVI and AGB (g m⁻²).

NDVI data processing

We created a function within the Rstudio development environment to calculate AGB with the conversion equation mentioned above:

$$AGB = -74.432 * \max\left(0; \log\left(\frac{0.88 - NDVI}{0.714}\right)\right) + 15.25$$

As we had negative NDVI values during winter, e.g. due to the presence of snow or water, some calculated AGB values were also negative. Thus, the values of NDVI<0 cannot be exploited because snow cover hides vegetation, making impossible establishing a correlation with AGB. Only positive values corresponding to plant cover were kept for further analysis. By excluding negative NDVI values, the calculated data gave the dynamics of plant cover, as shown in Fig. D6.

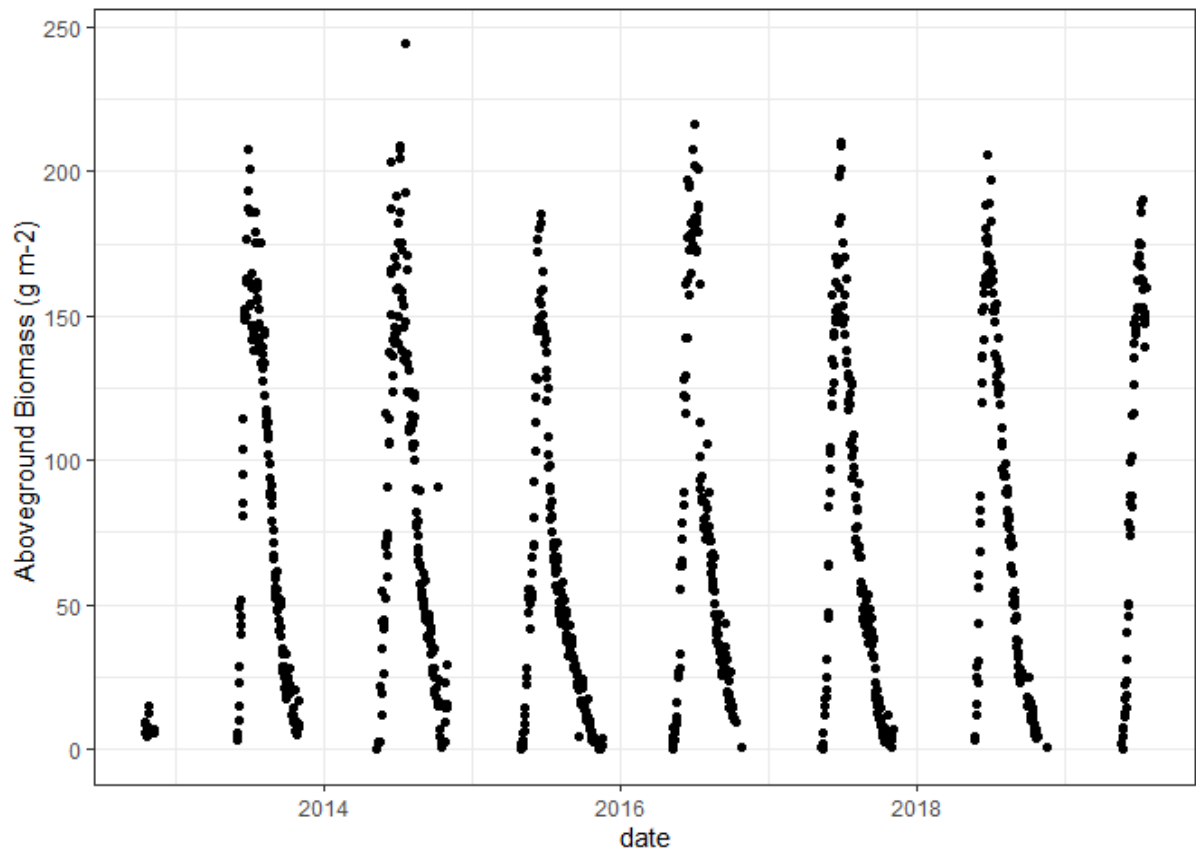


Fig. D6. Interannual dynamics of AGB ($g\ m^{-2}$).

This work allowed us to verify the data as well as the method used. Overall, the approach proved effective because the converted data are a coherent representation of measurements. This supports using this conversion method in the PASTORALP modelling framework for the purpose of model calibration.